Natural radioactivity in soils of Ijero, Nigeria: measurements and risk assessment

by

Tarryn Bailey

Thesis presented in partial fulfillment of the requirements for the degree of Master of Science in the Faculty of Natural Science at Stellenbosch University

Supervisor: Prof. R.T. Newman
Co-supervisor: Dr. P.P. Maleka

December 2019

Declaration

By submitting this thesis electronically, I declare that the entirety of the work contained therein is my own, original work, that I am the sole author thereof (save to the extent explicitly otherwise stated), that reproduction and publication thereof by Stellenbosch University will not infringe any third party rights and that I have not previously in its entirety or in part submitted it for obtaining any qualification.

Date: December 2019

Abstract

Natural radioactivity in soils of Ijero, Nigeria: measurements and risk assessment

T. Bailey

Department of Physics,

University of Stellenbosch,

Private Bag X1, Matieland 7602, South Africa.

Thesis: MSc (Physics)

December 2019

Several soil samples were obtained from Ijero, Nigeria, where the chemical and radio-toxicity of soil is under question due to ongoing and unregulated mining activities. The soil samples were crushed, sieved, dried and sealed in identical cylindrical containers. The activity concentrations of primordial radionuclides in the ^{238}U series, ^{232}Th series and ^{40}K were measured using a High-Purity Germanium (HPGe) detector. Subsequently, radiological risk factors were calculated to assess the average risk to an individual living in Ijero.

The measured activity concentrations for the ^{238}U series ranged from 10.1±1.4 to 83.9±2.1 Bq/kg with a mean value of 38.5 Bq/kg. For the ^{232}Th series, the activity concentrations ranged from 11.3±2.9 to 108.0±2.4 Bq/kg with a mean value of 37.1 Bq/kg. Finally, the ^{40}K activity concentration ranged from 67±26 to 1196±36 Bq/kg with a mean value of 461 Bq/kg. The mean values for the activity concentrations of the ^{238}U series, ^{232}Th series and ^{40}K were comparable to the global population-weighted average for concentration in soils, given by UNSCEAR 2000, of 33 Bq/kg, 45 Bq/kg and 420 Bq/kg respectively.

In total, thirty soil samples from Nigeria were measured. Of these samples, thirteen had ^{238}U series concentrations above 33 Bq/kg, three of those samples had

activity concentrations for the ^{238}U series above 70 Bq/kg. For the ^{232}Th series, thirteen samples had activity concentrations above 45 Bq/kg with two samples above 90 Bq/kg. Finally, seventeen samples had ^{40}K activity concentrations above 420 Bq/kg with eleven of those above 800 Bq/kg.

Five soil samples had hazard indices that summed to more than the permissible limit of 1 mSv/yr. Eight samples were above the permissible limit for the Annual Effective Dose rate, where indoor and outdoor dose rates must sum to 1 mSv/yr. The Annual Gonadal Equivalent Dose limit of 300 μSv/yr was surpassed by twenty-five samples.

For the Excess Lifetime Cancer Risk (ELCR) and excess percentage risk, which estimates the probability that an individual could develop cancer in their lifetime, seven samples exceeded the maximum ELCR of 0.29×10^{-3}. The ELCR results ranged from 0.102×10^{-3} to 0.483×10^{-3}. The highest ELCR result is 1.67 times greater than the upper recommended value of 0.29×10^{-3}. A value of 1.67 for the ratio of the calculated ELCR to the maximum permissible ELCR corresponds to an excess percentage risk of 67%. The mean ELCR is 0.239×10^{-3} which is below the maximum recommended value.

There are certain locations where the activity concentration of primordial radionuclides is high, far surpassing the world average. However, most of the soil samples measured did not exceed the recommended maxima for activity concentrations and radiological risk factors.

Uittreksel

Natuurlike radioaktiwiteit in grondsoorte van Ijero, Nigerië: metings en risikobepaling

("Natural radioactivity in soils of Ijero, Nigeria: measurements and risk assessment")

T. Bailey

Departement Fisika,

Universiteit van Stellenbosch,

Privaatsak X1, Matieland 7602, Suid Afrika.

Tesis: MSc (Fisika)

Desember 2019

Verskeie grondmonsters is verkry uit Ijero, Nigerië, waar die chemiese en radiotoksisiteit van grond bevraagteken word weens voortgesette en ongereguleerde mynaktiwiteite. Die grondmonsters is fyngedruk, gesif, gedroog en in identiese silindriese houers verseël. Die aktiwiteitskonsentrasies van oer-radionukliede in die ^{238}U-reeks, ^{232}Th-reeks en ^{40}K is gemeet met behulp van 'n Hoë Suiwerheid Germanium (HPGe) detektor gekoppel aan 'n Palmtop multikanaal-ontleder (MCA). Daarna is radiologiese risikofaktore bereken om die risiko gemiddelde vir 'n individu wat in Ijero woon te bepaal.

Die gemete aktiwiteitskonsentrasies vir die ^{238}U-reeks het gewissel van 10.1±1.4 tot 83.9±2.1 Bq/kg met 'n gemiddelde waarde van 38.5 Bq/kg. Vir die ^{232}Th-reeks het die aktiwiteitskonsentrasies gewissel van 11.3±2.9 tot 108.0±2.4 Bq/kg met 'n gemiddelde waarde van 37.1 Bq/kg. Laastens het die ^{40}K aktiwiteitskonsentrasie gewissel van 67±26 tot 1196±36 Bq/kg met 'n gemiddelde waarde van 461 Bq/kg. Die gemiddelde waardes vir die aktiwiteitskonsentrasies van die ^{238}U-reeks, ^{232}Th-reeks en ^{40}K was vergelykbaar met die wêreldwye bevolkingsgeweegde gemiddelde vir konsentrasie in grondsoorte, gegee deur UNSCEAR 2000, van onderskeidelik 33 Bq/kg, 45 Bq/kg en 420 Bq/kg.

'n Totaal van dertig grondmonsters uit Nigerië is gemeet. Hieruit was die ^{238}U-reeks konsentrasies van dertien monsters bo 33 Bq/kg. Drie van die monsters het aktiwiteitskonsentrasies vir die ^{238}U-reeks bo 70 Bq/kg gehad. Vir die ^{232}Th-reeks het dertien monsters aktiwiteitskonsentrasies bo 45 Bq/kg gehad met twee monsters bo 90 Bq/kg. Die ^{40}K aktiwiteitskonsentrasies van sewentien monsters was bo 420 Bq/kg, met elf hiervan meer as 800 Bq/kg.

Vyf grondmonsters het gevaarindekse gehad wat tot meer as die toelaatbare limiet van 1 mSv/jr saamgestel het. Agt monsters was bo die toelaatbare limiet vir die jaarlikse effektiewe dosis tempo, waar binne en buite dosis tempo's tot 1 mSv/jr moet saamtel. Die jaarlikse gonadale ekwivalente dosisgrens van 300 μSv/jr is oorskry deur vyf en twintig monsters.

Vir die oormaat leeftyd kankerrisiko (ELCR) en die oormaat persentasierisiko, wat die waarskynlikheid dat 'n individu kanker kan ontwikkel in hul leeftyd beraam, het sewe monsters die maksimum ELCR van 0.29×10^{-3} oorskry. Die ELCR resultate het gewissel van 0.102×10^{-3} tot 0.483×10^{-3}. Die hoogste ELCR resultaat is 1.67 keer groter as die boonste aanbevole waarde van 0.29×10^{-3}.'n Waarde van 1.67 vir die verhouding van die berekende ELCR tot die maksimum toelaatbare ELCR stem ooreen met 'n oortollige persentasie risiko van 67%. Die gemiddelde ELCR is 0.239×10^{-3}, wat onder die maksimum aanbevole waarde is.

Daar is sekere plekke waar die aktiwiteitskonsentrasie van oer-radionukliede hoog is, wat die wêreldgemiddelde ver oortref. Die meeste grondmonsters wat gemeet is het egter nie die aanbevole maksimum vir aktiwiteitskonsentrasies en radiologiese risikofaktore oorskry nie.

Acknowledgements

I would like to express my sincere gratitude to the following people and organisations...

The financial assistance of iThemba LABS (National Research Foundation) towards this research is hereby acknowledged. Opinions expressed and conclusions arrived at, are those of the author and are not necessarily to be attributed to the NRF.

iThemba LABS and Dr P.P. Maleka for the assistance, laboratory equipment and laboratory space (the Environmental Radiation Laboratory) provided during this study.

My supervisor, Prof. R.T. Newman, and my co-supervisor, Dr. P.P. Maleka, for their mentorship, guidance and the wealth of knowledge that was shared with me.

My collaborators, Dr. Adewale Adesiyan, Prof. Leslie Petrik and Mr. Ryno Botha for the collection of samples, their research, communication, collaboration and their significant contribution to this study.

Stellenbosch University for the financial assistance, the use of their equipment and office space.

Dedications

This thesis is dedicated to...

Prof Newman, for his continuous involvement and encouragement. He consistently offered excellent advice and opportunities.

Mom and dad for their unconditional love and support, both psychologically and financially.

Tawfeeq Titus for consistently motivating me to set higher goals and take every opportunity to grow academically.

Contents

List of Figures

List of Tables

Chapter 1

Ijero, Nigeria

Ijero Ekiti is a town in Ekiti state in south-western Nigeria. It lies at 7.8120° latitude and 5.0677° longitude. For this study, soil samples were taken between 7°47' and 7°52' north of the Equator and 5°01' and 5°07' east of the Greenwich meridian. The altitude in Ijero varies between 390 and 586 metres. Ijero experiences a tropical climate. There are two distinct seasons, a rainy one, with south-westward monsoon winds from April to October, followed by a dry season with fog and north-eastward winds from November to March. Temperatures in Ijero fluctuate between 21 and 34°C [AIK18]. Figures 1.1a to 1.2b show the location of Ijero.

Approximately 80% of the land on which Ijero is built has an abundance of mineral resources. The small town boasts minerals such as columbite, quartz and feldspar among other rare earth metals and gems [Usi+19]. The town does not have many local businesses and its people live in poverty.

1.1 Geology

The geology of the study area is relevant when considering the degree to which mining and the use of fertilizers could enhance the natural background radiation.

The study area in Ijero, Nigeria is underlain by various types of rock as shown in Figure 1.3. Namely, biotite gneiss (green), biotite schist (light blue), amphibolite schist (dark blue), quatzite (yellow), epidiorite (grey) and migmatite gneiss (beige) [OA10].

Schists are medium grade metamorphic rocks. They have experienced moderate heat, pressure and chemical change that resulted in a foliated structure made up of small plate-like mineral grains. If they are exposed to increasingly harsh conditions, they metamorphose further to become gneiss. The parent rock need not consist of any particular minerals to be named a schist, it must only exhibit the foliated appearance as a result of the plate-like minerals. Schists are named according to the minerals that are visible to the naked eye, when inspected. They are also the host rocks for gemstones such as ruby, which Ijero is known for. Epidiorite is a form of schistose metamorphic rock [Kin05c]. In the Svecofennian schist belt in southern Finland, there are occurrences of uranium and thorium deposits, usually associated with the granitic and pegmatitic deposits in the migmatite [Dża+18]. As can be seen in Figure 1.3 this sample area also contains granites and pegmatites within the biotite schist as well as the migmatite gneiss.

Gneiss is a high grade metamorphic rock. It has experienced more intense heat, pressure and chemical change than schists. Its foliation is also more distinct than the foliation seen in schists. The more distinct foliation is what characterizes it as a gneiss. It is named according to the dominant mineral in the metamorphic environment [Kin05a]. In the eastern part of the USA, gneisses are often enriched with uranium [WHO09]. In Poland, a study conducted in the Opava mountains found that migmatite gneiss and granite contained the highest and second highest concentrations of ^{238}U and ^{232}Th in the region [Dża+18]. The granite had a ^{40}K activity concentration of 942 Bq/kg. An increased activity concentration of 1560 Bq/kg was measured in weathered granite, possibly due to the presence of potassium feldspar. Gneiss and migmatite gneiss had ^{40}K activity concentrations of 645 and 778 Bq/kg respectively. Migmatite gneiss presented the highest activity of ^{232}Th of 71 Bq/kg [Dża+18]. In Brazil, migmatite gneiss activity concentrations ranged from 78 to 81 Bq/kg [Anj+11]. The activity concentration of the ^{238}U series was estimated by Dzaluk et al. by assuming radioactive equilibrium in the ^{238}U series for ^{226}Ra, ^{222}Rn, ^{214}Pb and ^{214}Bi [Dża+18] (refer to Appendix A). For ^{238}U in particular, the activity concentrations ranged from 6 Bq/kg, for weathered gneiss, to 52 Bq/kg for migmatite gneiss. Granite had an activity

concentration of ^{238}U of 44 Bq/kg [Dża+18].

Granitic types of igneous rock are generally associated with higher concentrations of ^{238}U and ^{232}Th than sedimentary rock [UNS00].

Since there are granite and pegmatite deposits in the migmatite gneiss, it is expected that the ^{238}U series and ^{232}Th series activity concentration will be enhanced. Samples that lie atop the migmatite gneiss and near granite and pegmatite deposits are expected to have higher ^{238}U series and ^{232}Th series activity concentrations.

Finally, quartzite is a metamorphic rock that is approximately 90% quartz, interlocked in a crystalline structure. When sandstone is subject to intense heat, pressure and chemical changes, the sand and silica within is recrystallized, forming an extremely strong quartzite rock. Quartzite can exist in a variety of colours depending on impurities present during metamorphosis. Pure quartzite is white or gray in colour and is not foliated [Kin05b].

Each of these rock types is formed at converging plate boundaries which is enough to cause medium grade metamorphosis. Gneiss and quartzite will most likely form during the formation of mountains at plate boundaries. The intense pressure when being submerged under great depths, near igneous intrusions and between converging plates is enough to induce high grade metamorphosis.

1.2 Environmental Contamination

In Nigeria, 95% of mining activities are unregulated and often performed in areas where radiological risks and geological surveys have not yet been performed [Nig19]. Ijero has been a mining community since the 1930s. Mining alone comes with its own set of radiological hazards. Most of the naturally occurring radioactive material (NORM) around mines contain ^{238}U and ^{232}Th [Usi+19]. NORM is undisturbed material that naturally contains primordial radionuclides and their radioactive decay products. Mining and processing of these materials can generate waste that contains these radionuclides in higher concentrations

and disturbs them in a way that makes them more likely to contribute to human and environmental exposure. When this happens, these radioactive materials are known as technologically enhanced naturally occurring radioactive materials (TENORM) [OAO16].

Ijero forms part of the Ijero Local Government Area which had a population of 93 286 in 1991. The unregulated mining was seen as a source of economic opportunity by surrounding communities [Bab+13] and by 2006, the population grew to 221 405 [AO17]. In the 2019 census [Rev], its population was reported as 167 632. It remains one of the largest towns in Ekiti state. Recently, the abundant mineral resources, such as cassiterite, quartz, mica, marble, tin ore and columbite [Law02] have drawn the attention of foreigners from the West-African sub-region. The traditional leader, the Ajero of Ijero, stated that both local and foreign miners occupy the mines. However the number of foreign miners is much greater [Ade18a].

Whether local or foreign, the miners in Ijero are all unregulated and therefore should be classified as illegal miners. Due to the unregulated nature of their mining, these illegal miners are not properly protected from radioactive dust particles and ^{222}Rn gas inside the mines and trenches as shown in Figure 1.4. The abandoned mines once hosted large scale mining operations and contain significant amounts of naturally occurring radionuclides [OAO16]. Most of the local miners are under-aged, mining for precious stones. Not only do they expose themselves, but they transport their takings past farm land and water sources, contaminating the environment. Once they arrive home, they expose their families to the same potentially radioactive material [OAO16]. In addition, the heaps of displaced sand and rocks that are left behind are piled metres high and could be transported by wind or rain to contaminate the environment [Usi+19][OAO16].

The contamination of the environment is particularly concerning as Ijero is a farming community where locals grow and sell their produce to make a living. The crops grown include cocoa, coffee, bananas, cashews and tomatoes. The water sources are easily contaminated since the community chiefly relies on borehole

water and wells [Hom].

Contamination of the food and water sources could lead to an increased radiation dose due to inhalation and ingestion of radioactive particles [Ran+15]. If the parent rock has a high concentration of ^{238}U then the surrounding geological material could have a high concentration of its decay product, ^{226}Ra and consequently, ^{222}Rn. As a result, water sourced from boreholes and wells could already have a higher concentration of ^{222}Rn gas than water from reservoirs and dams built above ground [Ism16].

Additionally, many dwellings in Ijero are predominantly built from clay and mud bricks. For an impoverished town, it can be assumed that the clay and mud is sourced locally and therefore has a similar geological composition. In fact, the locals consider the mine tailings a cheaper alternative to other commonly used building materials [Usi+19]. The clay waste around the mines is used by the locals for pottery [OAO16]. This could result in an increased indoor radiation dose rate to the average individual.

The analysis of soil is therefore necessary to assess the activity concentration of primordial radionuclides in the environment of Ijero [UNS00].

1.3 Previous Studies in Ijero

A study, by Babatunde et al., performed in Ijero surveyed 118 miners in south west Nigeria. The survey revealed that 39 of the respondents suffered chronic cough, 47 experienced chest pain, 21 coughed mucoid or bloody sputum and 27 felt progressive breathlessness. Skin rashes experienced by 19.5% of respondents could be linked to chemical toxicity in the mines [Bab+13].

A study by, Ajiboye et al., on ^{222}Rn in groundwater and soil gas, performed in South-west Nigeria, concluded that Ijero presented a mean total annual effective dose due to inhalation and ingestion of 256.2 μSv which is significantly higher than the World Health Organisation's recommended limit of 100μSv. In Ijero, the maximum radon concentration was reported as 165.0$\pm$12.0 Bq/L, in

the groundwater, and 80.4±2.1 Bq/L in the soil gas. The study deduced that the groundwater posed a considerable radiological hazard to the population. The study highlighted the increase in lung cancer cases in Nigeria for non-smokers and stated that it could be attributed to inhalation and ingestion of radionuclides [AIK18].

A study, by Olise et al., published on Ijero in 2016, stated that the activity concentrations of the ^{238}U series, ^{232}Th series and ^{40}K ranged from 12.90±0.02 to 250±0.02 Bq/kg, 1.00±0.05 to 115.37±0.02 Bq/kg and 45.56±0.01 to 2610.27±0.01 Bq/kg respectively. The mean activity concentrations of the ^{238}U series, ^{232}Th series and ^{40}K were 70.57±0.08 Bq/kg, 19.56±0.03 Bq/kg and 659.15±0.01 Bq/kg respectively. These results can be compared to the global population-weighted average for concentration in soils, given by UNSCEAR 2000, of 33 Bq/kg, 45 Bq/kg and 420 Bq/kg respectively. The same study reported a mean outdoor dose, due to the ^{238}U series, ^{232}Th series and ^{40}K in the soil, of 0.26 mSv which is much higher than the worldwide average of 0.06 mSv for outdoor exposures [UNS00]. If the soil is used in the building materials, then the study reported an indoor dose of 0.18 mSv, which is lower than the worldwide average of 0.41 mSv for indoor exposures [UNS00]. Finally, the total annual effective dose ranged from 0.03 to 0.82 mSv with a mean of 0.44 mSv which is lower than the global mean of 0.48 mSv. The study concluded that proper monitoring and control of construction materials is required to protect miners and the public [OAO16].

In a study, by Akinnagbe et al., the ground water in Ijero was deemed relatively safe as the effective dose due to ^{222}Rn seemed low. The results ranged from 0.168 to 78.509 Bq/L from stream and borehole samples. None of the samples presented a concentration above the recommended limit of 100 Bq/L. None of the samples surpassed the annual effective dose limit of 0.2 mSv/yr, for children, or 0.1 mSv/yr for adults [Aki+18].

A study, by Isinkaye, on the radiological hazards due to mine tailings and sediment presented soil activity concentrations for the ^{226}Ra series,^{232}Th series and ^{40}K ranging from 7.62 to 50.31 Bq/kg, 12.68 to 234.18 Bq/kg and 249.66 to

1459.25 Bq/kg respectively. The study concluded that while the hazard indices are higher than global averages, they are acceptable [Isi14].

A paper published in 2018, in Ijero, by Usikalu et al. once again highlighted the risks. Comparing the soil in mining areas to those in living areas, the results showed a mean absorbed dose rate of 89.70 nGy/hr and 72.2 nGy/hr for mining and living areas respectively. The mean activity concentration of ^{238}U series,^{232}Th series and ^{40}K was 128.05 Bq/kg, 24.8 Bq/kg and 455.05 Bq/kg for mining areas and 42.02 Bq/kg, 43.27 Bq/kg and 635.41 Bq/kg for living areas. The mining areas therefore presented much higher activity concentrations for the ^{238}U series. This was thought to be due to the mineral contents at the mine or the processes performed for extraction of minerals. It was speculated that the high concentrations of potassium may be due to the use of inorganic fertilisers in the living areas [Usi+19].

In the present study, the soil was sampled in thirty locations around Ijero. The primordial radionuclides investigated were ^{238}U , ^{232}Th and ^{40}K. The measurement of each soil sample was performed at iThemba LABS, in the Environmental Radiation Laboratory (ERL), using a High-Purity Germanium (HPGe) detector.

The activity concentration for each soil sample was then analysed to quantify the radiological risk factors such as the dose to the average individual and the likelihood that said individual could develop cancer in their lifetime due to this exposure. This study aims to relate the activity concentration in the soil to the geology of the study area. The results will primarily quantify the natural background radiation present, giving some perspective on the degree to which additional human activity, such as mining and the use of fertilizers, could enhance the background radiation.

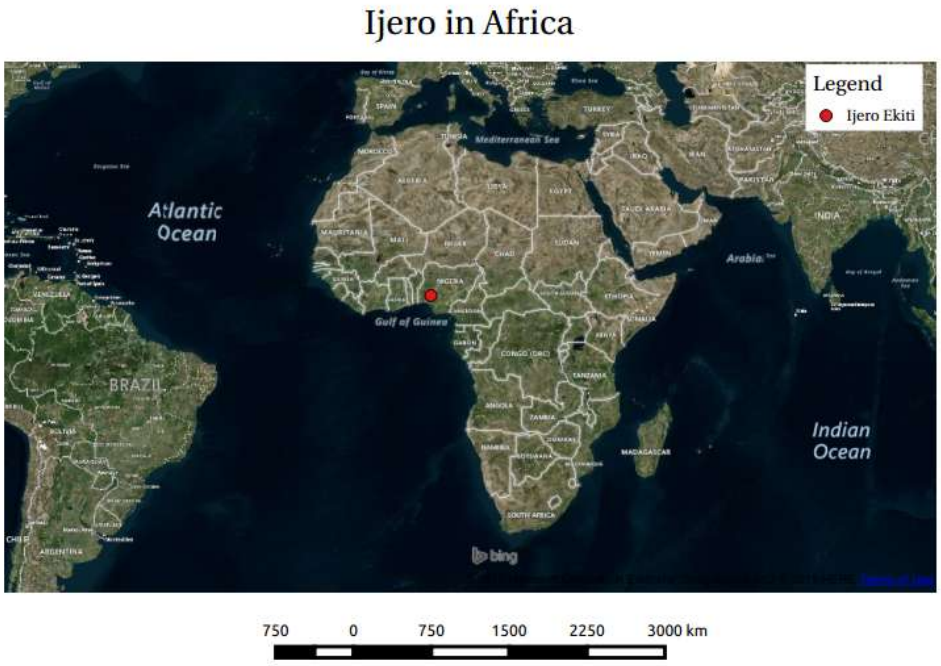

(a) Ijero in Africa

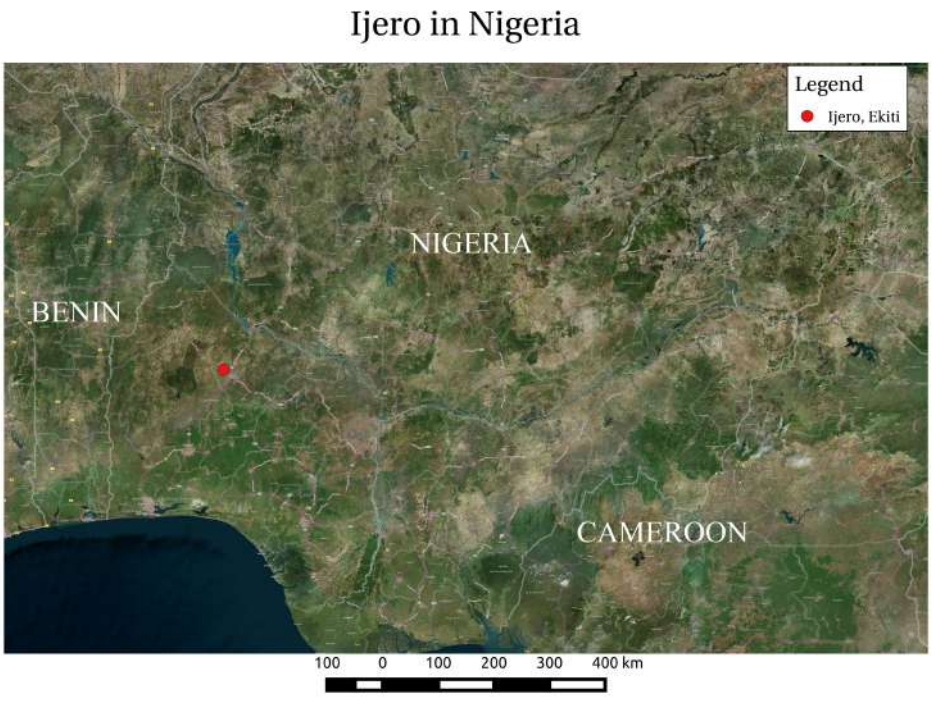

(b) Ijero in Nigeria

Figure 1.1: Ijero in Africa and Nigeria

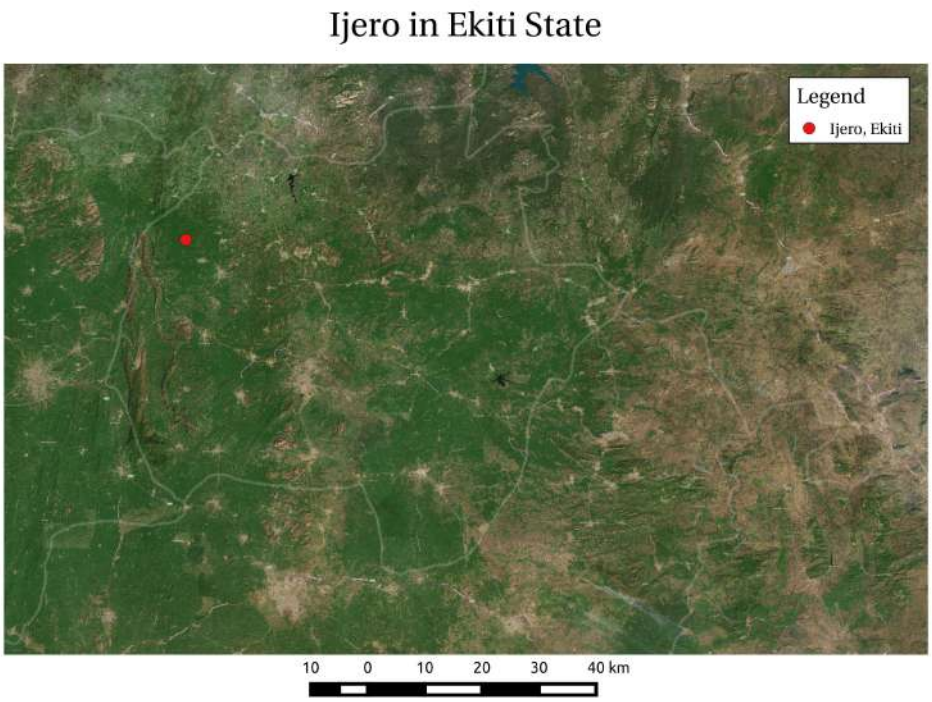

(a) Ijero in Ekiti State

(b) Ijero

Figure 1.2: Ijero in Ekiti State

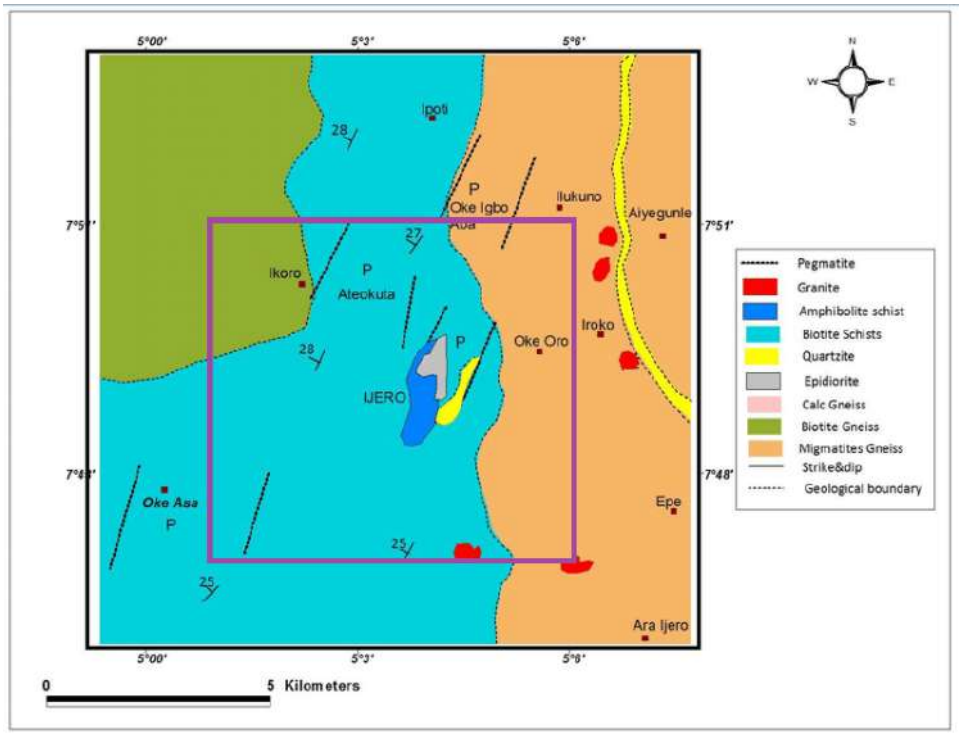

Figure 1.3: A colour coded image of Ijero, indicating the square area in which the samples were obtained as well as the locations of the various parent rock types [OA10]

Figure 1.4: Illegal miners in Ijero, Nigeria [Ade18a]

Chapter 2

Radiation

2.1 Radioactivity and Half-life

Atoms are known to be composed of smaller subatomic particles, namely neutrons, protons and electrons. The neutrons and protons occupy the nucleus and the electrons form an electron cloud around the nucleus. Protons are positively charged, electrons are negatively charged and neutrons have a net zero charge [NRF17a].

The protons exist in close proximity to one another inside the nucleus. Each proton experiences repulsive Coulomb forces due to the presence of nearby protons. The nucleus is held together by the nuclear force that attracts the protons and neutrons to each other. Over short distances, this nuclear force is strong enough to overcome the repulsive Coulomb force. This is a delicate balance and only certain combinations of protons and neutrons produce stable atoms. If the ratio of protons to neutrons results in an unstable nucleus, the nucleus will attempt to gain stability via radioactive decay [Wyn17].

During β^+ decay, when a proton is converted to a neutron, a positron and a neutrino, the atomic number changes, that is, the identity of the element changes. Similarly, during β^- decay, when a neutron is converted to a proton, an electron and an anti-neutrino, the element will change. If the number of protons remains constant, while the number of neutrons changes, an isotope of the original atom is formed. Atoms can have more than one isotope and each isotope could either

be stable or unstable. If an isotope is unstable and it disintegrates by radioactive decay, then it is called a radioisotope or a radionuclide. Isotopes, their decay products and the decay products of their decay products can form a decay chain. These decay chains continue until a stable isotope is reached [CSP12].

The half-life of a particular radionuclide is a characteristic constant that varies from a few microseconds to billions of years. The half-life is defined as the time it takes for one half of the atomic nuclei of a radioactive substance to decay [CSP12].

2.2 Alpha, Beta and Gamma Radiation

Three common types of ionizing radiation related to radioactive decay include alpha particles, beta particles and gamma radiation.

Alpha particles consist of two protons and two neutrons. They are essentially helium nuclei. Alpha particles can be considered the heaviest form of naturally occurring ionizing radiation. While they are approximately four times heavier than protons and neutrons, they are approximately eight thousand times heavier than beta particles, which are electrons or positrons. The alpha particle carries a charge of +2. This increases its mean energy loss per unit distance due to ionization and excitation of atoms in the medium.

Alpha particles are positively charged and relatively massive so they readily interact with nearby atoms. During these interactions, they lose most of their energy in a relatively short, confined and straight path. This type of radiation is therefore commonly referred to as being high linear energy transfer (high LET) radiation when interacting with human tissue [NRF17a].

Since alpha particles lose their energy so quickly, they are especially easy to shield. They are unable to penetrate the outer layers of human skin. However, this form of radiation can still prove its potency when inhaled or ingested. During inhalation and ingestion, alpha particles can directly impart their energy into sensitive tissues. Radon, an alpha particle emitter, is considered to be one of the leading causes of lung cancer in areas with greater natural background radiation [UNS00].

Beta particles have a charge of -1 or +1 and are essentially electrons or positrons. They have a lower ionizing ability and a larger penetrating ability than alpha particles due to their lower charge [CSP12]. It is relatively easy to shield them using aluminium foil. While beta particles can present a small external risk, they are capable of serious cell damage when ingested or inhaled.

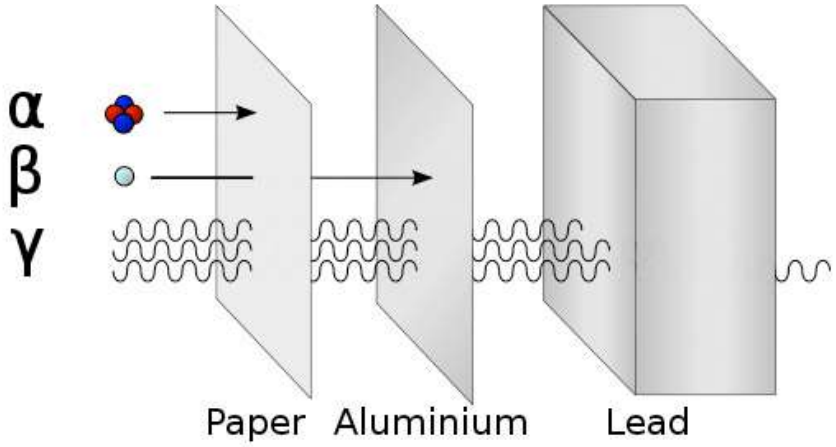

Figure 2.1: The penetrability of alpha, beta and gamma radiation [ICR]

Gamma radiation is a high energy electromagnetic wave that consists of photons. Gamma radiation can interact with atoms, ionize them and cause them to release directly ionizing radiation, such as electrons [BB11]. The wavelength of gamma rays is particularly short, only a few picometres. Photons are chargeless and massless, meaning that gamma radiation has immense penetrating ability. Consequently, a thick, dense material with high atomic number is required to attenuate gamma rays. Lead and depleted uranium are commonly used [NRF17a].

2.3 Radiation and the human body

Ionizing radiation affects human cells on an atomic level. It is possible that ionizing radiation could pass through a cell and cause no damage at all. Nevertheless, ionizing radiation is capable of damaging and killing cells. In the worst case, it can damage the chromosomes within the nucleus of the cell. This can alter the reproductive process of the cell, resulting in abnormal cell multiplication and impaired function.

It is generally more likely for high LET, heavy, charged particles, like alpha particles, to cause direct chromosomal damage than for gamma radiation, which is essentially massless and chargeless [NRF17a].

It is possible for ionizing radiation to create free radicals by interacting with water within cells. Free radicals like OH^- and H^+ are exceptionally reactive owing to the presence of an unpaired electron in the molecule. These free radicals could bond with H_2O to form destructive chemicals like hydrogen peroxide (H_2O_2) within the cell. As a result, the cell could experience severe damage to critical structures, resulting in cell death or mutation.

Chromosomes are most sensitive to radiation and chemical damage during cell division. Therefore children and foetuses are particularly susceptible to chromosomal damage due to the high rate of cell division throughout their bodies [Hun12].

Exposure to low levels of natural background radiation will generally not result in any acute radiation sickness symptoms. However, it can result in or contribute to an increased probability of long term effects.

2.4 Dose Measurements

It is essential to quantify the potential risks due to exposure to radiation.

Ionizing radiation carries energy which is measured in electron-volts (eV). One eV is defined as the amount of energy gained by an electron when it is accelerated through a potential difference of 1 V. It is a very small unit of energy, equal to 1.6×10^{-19} joules. Therefore, the energy of radiation is normally given in kiloelectron-volts (keV) or megaelectron-volts (MeV) [NRF17b].

Originally, X-rays and gamma rays were quantified by the ionization they produced in air, known as their exposure. Exposure is the absolute value of the total charge of ions of one sign produced in air when all the electrons liberated per unit mass of air have been completely stopped in air. The unit of exposure is the

roentgen (R). The SI unit is the coulomb per kilogram (C kg^{-1}) [NRF17b].

Dose refers to the amount of energy deposited when radiation passes through a material. It can refer to absorbed dose, equivalent dose or effective dose.

Absorbed dose (D) is the energy absorbed per unit mass. It is a measure of the energy deposited in any medium by any type of radiation. The SI unit is joule per kilogram (J kg^{-1}) and is called gray (Gy) [NRF17b].

The equivalent dose (H) quantifies the effect of a given type of ionizing radiation on specific organs or tissues. It is calculated by multiplying the absorbed dose (D) by a radiation weighting factor, w_R. The equivalent dose for a tissue, T is shown in Equation 2.1 [NRF17b].

$$H_T = D_T \times w_R \tag{2.1}$$

The SI unit for equivalent dose is also J kg^{-1} but its name is the sievert (Sv) to distinguish it from absorbed dose [NRF17b].

The effective dose takes into account that certain organs are more sensitive to radiation than others. The ICRP assigns tissue weighting factors w_T to each organ that take the varying radiosensitivities into account.

The total effective dose for all exposed organs or tissues is the sum of the product of the tissue equivalent dose and the tissue weighting factor for a given organ over all organs. It is shown in Equation 2.2

$$E = \sum_T (H_T \times w_T) \tag{2.2}$$

In most cases the whole body is exposed to radiation. Assuming uniform irradiation, the total effective dose can be calculated by summing the doses to each organ or simply by taking a tissue weighting factor of 1 for the entire body [NRF17b].

2.5 Sources of Radiation

There are two primary groups of sources of radiation, naturally occurring radiation and anthropogenic "man-made" radiation. Naturally occurring radiation exists as primordial radionuclides which are present in soils, food, water our surroundings and cosmogenic radionuclides which are produced by the interaction of cosmic rays and atmospheric molecules. Anthropogenic radioactive sources exist as a result of atmospheric testing of weapons, electricity generation (reactors and power plants), medical procedures and industrial activities.

2.5.1 Naturally Occurring Radiation

This category can be divided into extra-terrestrial and terrestrial radiation [UNS00]. Extra-terrestrial radiation is cosmic rays. Terrestrial sources of radiation include radionuclides in the decay series of primordial radionuclides ^{238}U, ^{232}Th and the non-series ^{40}K [OAO16].

Cosmic radiation consists of highly penetrating, high energy particles from outer space [UNS00]. These particles are protons, alpha particles and electrons originating from within Earth's galaxy, produced by celestial objects and events. When cosmic rays interact with the Earth's atmosphere, cosmogenic radionuclides are produced. The exposure due to extra-terrestrial radiation varies from person to person based on location and individual activities [UNS00].

Primordial radionuclides are terrestrial sources that are believed to have existed since the formation of Earth. Radionuclides that have half-lives less than 10^8 years have already decayed to undetectable levels. Radionuclides with half-lives longer than 10^{11} years decay so slowly that they do not contribute to natural background radiation. The principal primordial radionuclides, in terms of dose, are ^{40}K, ^{232}Th and ^{238}U. The radionuclides in the decay series of ^{232}Th and ^{238}U are responsible for significant human exposures [UNS00].

Humans and other living organisms on Earth are exposed to radiation, as a result of primordial radionuclides, due to external exposure, inhalation and ingestion of particles containing these radionuclides and their decay products. All living

organisms are also sources of radiation. Humans, for example, are sources of radiation due to the ^{40}K, ^{14}C and ^{210}Pb radionuclides in our bodies which have been present since birth [UNS00]. The exposure due to other living organisms is substantially lower than that experienced due to extra-terrestrial, terrestrial and anthropogenic sources.

In this assessment, the primordial radionuclides considered are the ^{238}U series, ^{232}Th series and ^{40}K. Their half-lives are 4.468×10^9 years for ^{238}U, 1.40×10^{10} years for ^{232}Th and 1.248×10^9 years for ^{40}K [IAE].

These radionuclides can be found naturally in soil and rock. Trace amounts of dissolved uranium and thorium can be present in water. A decay product in the ^{238}U decay chain, ^{222}Rn, exists in air. Exposure to an individual varies depending on the local distribution of primordial radionuclides.

2.5.2 Anthropogenic Radioactive Sources

Atmospheric testing of weapons was conducted from the end of World War II, that is, since the 1950s up to the 1980s. The Union of Soviet Socialist Republics (USSR) as well as the United States of America tested thermonuclear weapons in the atmosphere, resulting in radioactive fallout that was globally distributed. Fallout is also a product of nuclear accidents like Chernobyl and atomic bombs such as Hiroshima and Nagasaki. Nuclear fallout contaminates food and water sources, increasing the rate of ingestion of radionuclides. Each year, these radionuclides decay, slightly decreasing the contribution due to atmospheric testing [UNS00].

Medical procedures such as diagnostic X-ray imaging contribute to the annual radiation exposure of the average individual. Radiotherapy techniques employed during cancer treatment have a much larger dose contribution to the individual. Additionally, certain diagnostic nuclear medicine procedures involve the injection of radiopharmaceuticals. These generally have short half-lives and decay inside the patient before being excreted [UNS00]. The International Commission on Radiation Units and Measurements (ICRU) develops and promulgates interna-

tional recommendations on radiation related quantities. All medical procedures are regulated by the ICRU to ensure that the radiation dose is kept as low as is reasonable for a particular procedure [ICR].

Certain industrial activities increase the amount of environmental radiation and individual exposure. For example, the manufacture of large scale consumer products such as combustible fuels produce TENORM as waste. The geological environment that forms oil deposits also contains NORM. The extraction process concentrates the NORM and brings it to the surface where it comes into contact with humans and contaminates the environment [EPA]. Activities that change the composition of the natural environment, such as mining or the use of fertilizers can increase the natural background radiation [Bax93].

During the mining process, rock deep within the Earth's crust is brought to the surface. This transports concentrated minerals and ores containing primordial radionuclides from underground to easily contaminate surface soil, water and food sources.

Fertilizers used in many agricultural communities are composed of heavy metals and large quantities of naturally occurring radionuclides. Phosphoric fertilizers are one of the largest contributors of anthropogenic uranium in the environment [Ran+15]. Both mining and fertilizers contribute to an increased level of exposure due to inhalation and ingestion of radionuclides.

2.6 ^{238}U, ^{232}Th and ^{40}K

The primordial radionuclides under investigation in this study, are ^{238}U, ^{232}Th and ^{40}K. The total contribution from terrestrial natural sources makes up 9% of the natural background, approximately 0.28 mSv per year [NRF17b]. This is the largest contributor to the external terrestrial average equivalent dose rate. Whether the dose rate is above or below average for an individual is still dependent on the local concentration of radionuclides.

^{40}K has the rare ability to undergo both beta plus and beta minus decay. It

can decay to ^{40}Ca by beta-minus decay, which it does 89.28% of the time. Alternatively, it can decay to ^{40}Ar by electron capture with the emission of a neutrino, beta-plus decay, which it does 10.72% of the time. The latter decay mode is followed by gamma-ray emission with an energy of 1.461 MeV [IAE]. The decay scheme for ^{40}K is shown in Figure 2.4

^{238}U and ^{232}Th have long decay chains consisting of multiple decay modes and daughter nuclides with varying half-lives as illustrated in Figures 2.2 and 2.3.

^{238}U decays by emitting an alpha particle to become ^{234}Th. ^{234}Th emits a beta particle to become ^{234}Pa. The decay process continues with alpha and/or beta as well as gamma-ray emitting radionuclides as indicated in Figure 2.2. Finally, a stable isotope of lead, ^{206}Pb, is reached and the decay series ends.

Similarly, ^{232}Th decays, emitting an alpha particle to become ^{228}Ra. ^{228}Ra emits a beta particle to become ^{228}Ac. ^{228}Ac emits beta and gamma radiation. The emission of the beta particle leads to the creation of ^{228}Th. The gamma rays with energy 338 keV and 911 keV are used in the ^{232}Th activity concentration calculation for this study. The decay process continues with alpha and/or beta, as well as gamma-ray emitting radionuclides, as indicated in Figure 2.3. Finally, a stable isotope of lead, ^{208}Pb, is reached and the decay series ends.

^{222}Rn is one of the radioactive daughters in the ^{238}U series. It emits an alpha particle during its decay. Since it is a noble gas, it emanates from the material in which it is confined. It is non-reactive, odourless and tasteless. Consequently, humans routinely inhale ^{222}Rn and its short-lived decay products. Its decay products are radioisotopes of heavy metals that can be deposited in human tissue during inhalation. Once inhaled, ^{222}Rn and its daughters undergo radioactive decay. The alpha particles emitted during the decay of ^{222}Rn and its daughters are able to directly interact with sensitive internal tissues. A radon isotope that is also highly radioactive and present in our surroundings is ^{220}Rn, commonly known as thoron. It is produced in the decay chain of ^{232}Th. Thoron is an alpha emitter with a half-life of 55,6 seconds. It is therefore able to decay during inhalation.

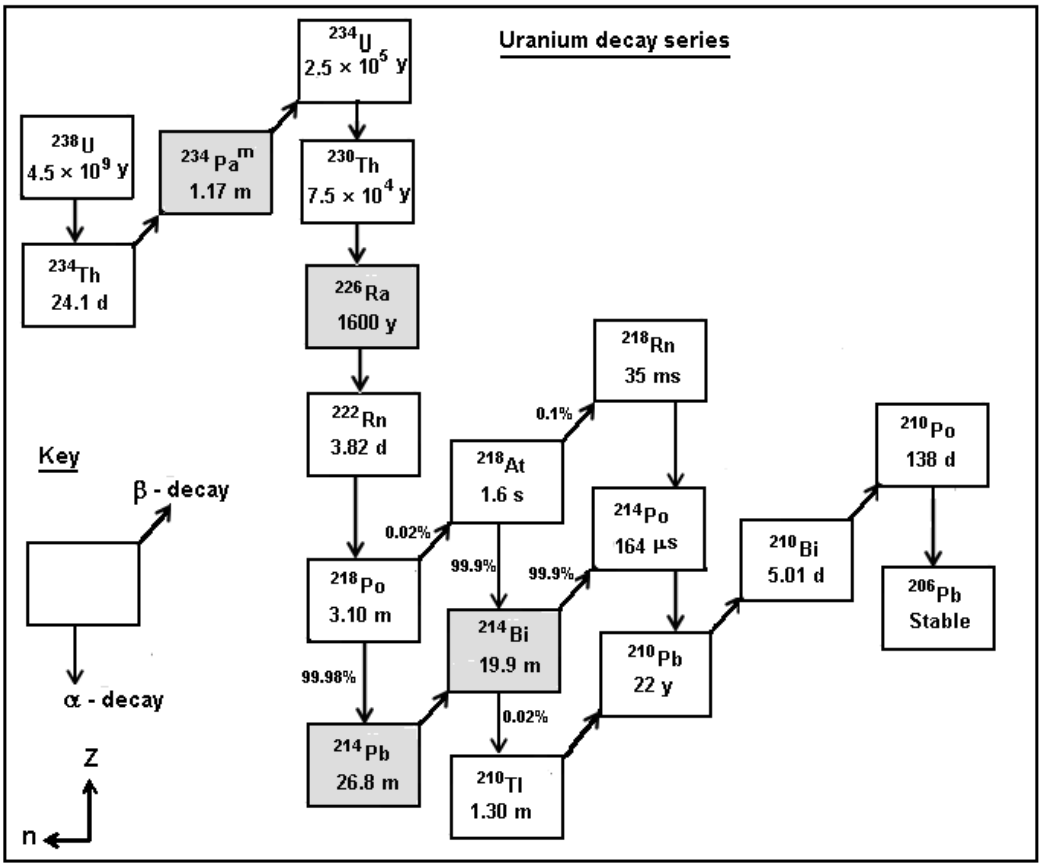

Figure 2.2: The ^{238}U decay series [K+87]

The most commonly affected tissues are those in the tracheobronchial region of the lung [IAR88].

2.7 Gamma-ray Interactions

Gamma rays are emitted during the radioactive decay of a nucleus. Understanding gamma-ray interactions is important when considering gamma detection and attenuation. In order to determine the presence of gamma radiation, it must be detected. For this study, a High Purity Germanium (HPGe) detector was used. For the gamma rays to be detected, they must interact with the detector material. The gamma-ray intensity is always measured to be less outside of the sample than it truly is inside, due to attenuation within the sample. Attenuation is defined as the measure of the reduction of gamma-ray intensity at a particular energy caused by an absorber material.

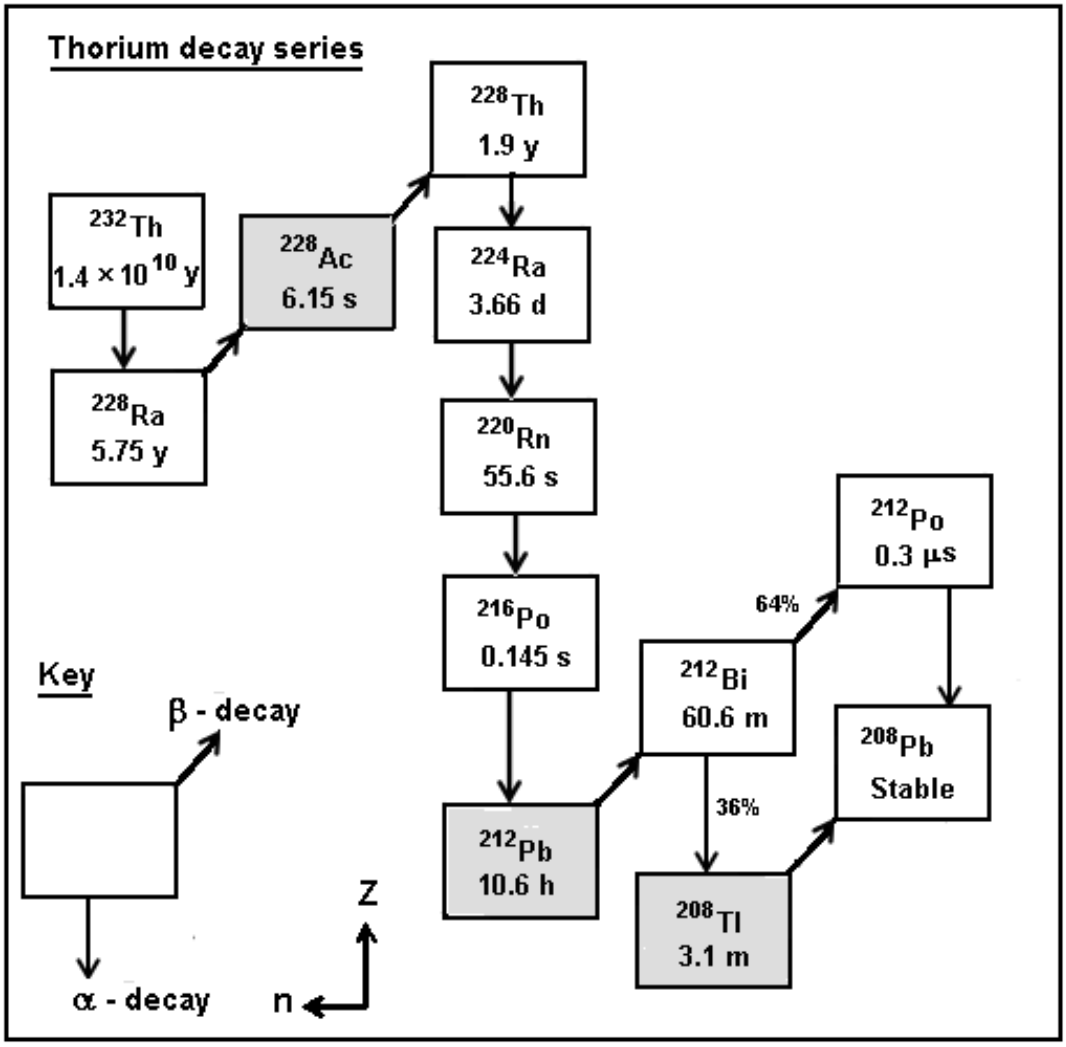

Figure 2.3: The ^{232}Th decay series [K+87]

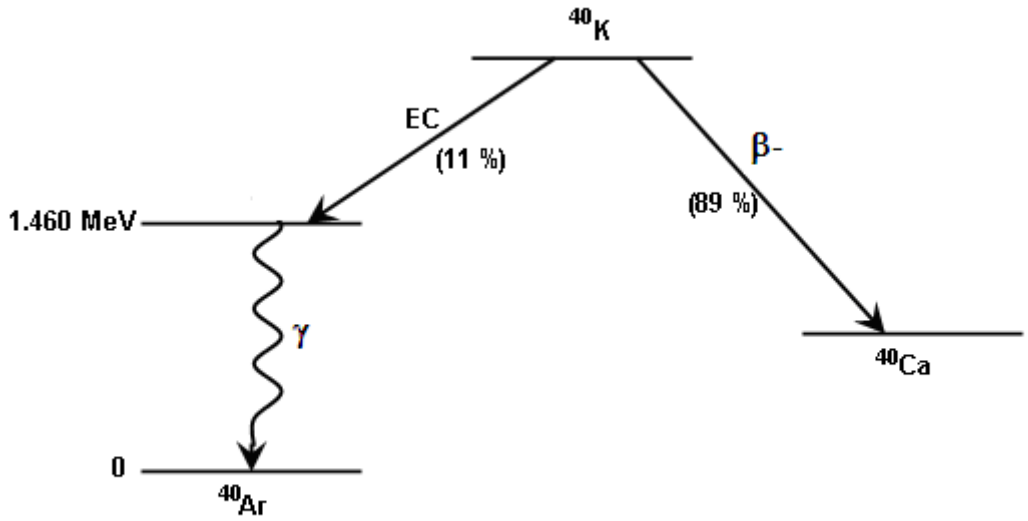

Figure 2.4: The decay scheme for ^{40}K [Ong13]

Gamma radiation is highly penetrating, far more so than alpha and beta particles [CSP12]. Gamma radiation, incident perpendicular to a rectangular slab of material, is attenuated exponentially. The number of gamma rays that pass through a slab decreases exponentially with thickness. Lambert's Law, used for linear attenuation is shown in Equation 2.3.

The attenuation coefficient depends on the electron density of the absorber material [Kno00], since gamma rays normally interact with atomic electrons. The attenuation within a sample depends on the gamma energy as well as the atomic number and density of the material. Therefore, it is convenient to use a mass attenuation coefficient, defined as the linear attenuation coefficient divided by the density of the material as shown in Equation 2.4.

$$I = I_0 e^{-\alpha x} \tag{2.3}$$

$$I = I_0 e^{-\frac{\alpha}{\rho}\rho x} = I_0 e^{-\mu z} \tag{2.4}$$

where

I is the radiation intensity after attenuation;

I_0 is the radiation intensity before attenuation;

α is the linear attenuation coefficient;
ρ is the density of the material;
x is the thickness of the material;
μ is the mass attenuation coefficient and
z is the density thickness of the material

The cross section for photoelectric absorption depends on the atomic number of the absorber material, as shown in Equation 2.5. This explains why lead is often used as a shielding material. Lead has a high atomic number and a high density, therefore it is able to attenuate gamma rays enough to prevent unsafe radiation doses to humans.

$$\sigma \propto \frac{Z^x}{E_\gamma^y} \tag{2.5}$$

where

σ is the cross section for photoelectric absorption;
Z is the atomic number of the absorber material;
x,y is approximately 4 and
E_γ is the energy of the photon

The major gamma-ray interactions include photoelectric absorption, pair production and Compton scattering. There are minor interactions, such as Rayleigh scattering and Thomson scattering, which scatter the gamma radiation without significantly affecting its energy [Kno00].

For the major interactions, photoelectric absorption occurs most frequently for low and ultra-low gamma energies, less than 0.5 MeV. Photoelectric absorption can only occur when the photon energy is greater than the binding energy of the atomic electron. Compton scattering dominates for mid-range energies, between 0.5 and 5 MeV, but can occur for photon energies in the range of 100 keV to 10 MeV. Pair production dominates for high energy photons, greater than 5 MeV, but can occur for photon energies as low as 1.022 MeV. The relationship between photon energy and atomic number of the absorber is illustrated in figure 2.5, displaying the areas in which each mode of interaction is dominant.

During photoelectric absorption, a gamma ray (a photon) interacts with an

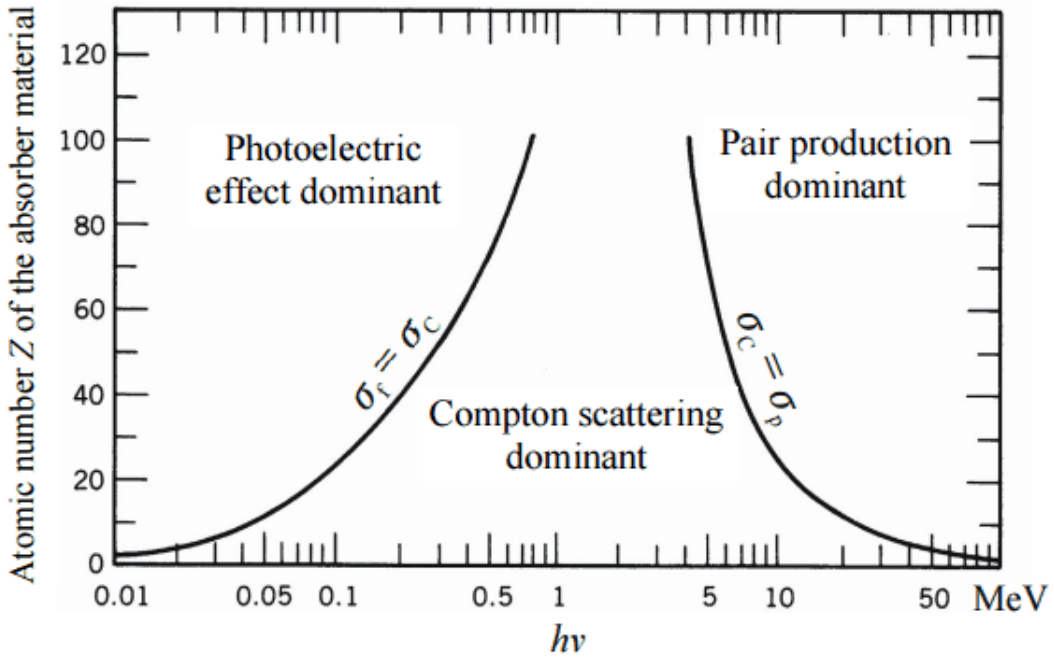

Figure 2.5: Interaction mechanisms for gamma radiation and the energies at which each mechanism dominates [Pow]

atomic electron as shown in Figure 2.6. During this interaction, the photon imparts all of its energy to the orbital electron. As a result, the orbital electron is ejected as a photoelectron with kinetic energy approximately equal to the difference between the photon energy and the electron's binding energy [BB11]. A small portion of the photon energy goes to the recoil of the atom to conserve momentum, as shown in Equation 2.6.

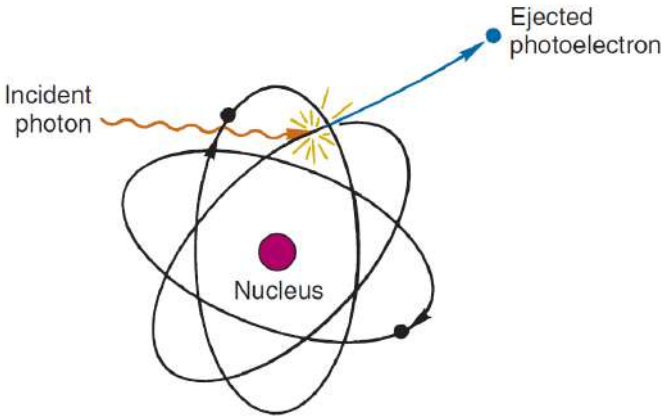

Figure 2.6: A schematic representation of photoelectric absorption [CSP12]

Using the conservation of energy:

$$E_\gamma = E_e + E_a + E_b \tag{2.6}$$

where

E_γ is the energy of the photon;
E_e is the energy of the photoelectron;
E_a is the recoil energy of the atom and
E_b is the binding energy required to eject the orbital electron.

For gamma energies above 0.5 MeV, it is most common for the K-shell electrons to be ejected during photoelectric absorption. Once the electron has left the atom as a photoelectron, the electrons in higher shells could rearrange to fill the vacancy. When an electron moves from a higher energy orbital to fill the vacancy in the K-shell, it will emit an X-ray with an energy that is characteristic to that atom. The characteristic X-ray could continue to interact with other orbital electrons and continue the cycle until the original photon energy has been dissipated or until an X-ray escapes the detector material [BB11]. These X-rays are emitted and recorded in coincidence with the photoelectron's energy.

Alternative to the filling of the K-shell vacancy, the excited atom could de-excite by releasing a cascade of electrons, called Auger electrons. This allows for a redistribution of energy and the transfer of the remainder of the photon energy to the detector material.

This is the most important mode of interaction for gamma-ray detection. When a photon deposits all its energy into the detector material, the pulse, which depends on the photon energy deposited, is recorded in the full-energy peak [Kno00]. The photoelectric absorption cross section depends on the atomic number of the detector material and the gamma-ray energy as shown in Equation 2.5. Low energy photons can only eject electrons that are weakly bound. Germanium is used in gamma radiation detectors as it is a semi-conductor with a relatively large atomic number of 32. Since the atomic number is high, the outer shell electrons are shielded from the nucleus and have a low binding energy. This allows low

energy gammas to interact by photoelectric absorption.

Compton scattering takes place when an incident gamma ray interacts with a free electron or an electron that is weakly bound, such that the binding energy is much less than the gamma-ray energy [Pod+05]. These weakly bound electrons are normally found in the outer shells [BB11]. The gamma ray is scattered and imparts only a portion of its energy to the Compton electron, as shown in Figure 2.7. The energy imparted will determine the directions in which the electron and the gamma ray travel after the interaction [Kno00]. Compton scattering normally continues until the gamma ray has sufficiently low energy and undergoes photoelectric absorption.

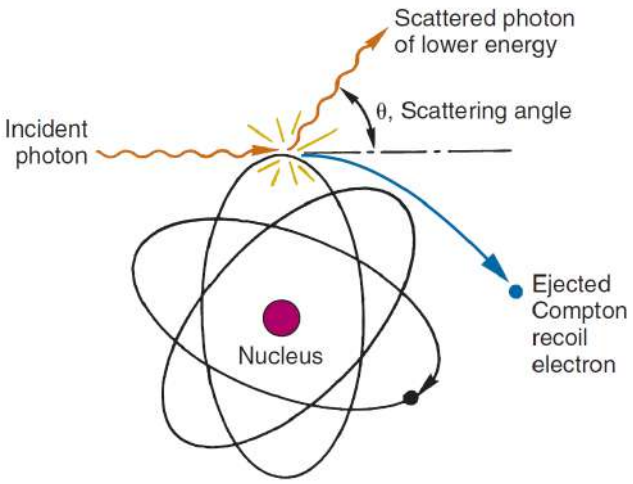

Figure 2.7: A schematic representation of Compton scattering [CSP12]

If a photon of energy greater than 1.022 MeV or an energy equal to two rest masses of an electron ($2m_0c^2$) passes near a nucleus, it will interact with the electric field surrounding the nucleus. The interaction is normally between the photon and an atomic nucleus, however it can occasionally be between the photon and an atomic electron [CSP12]. The photon will be transformed into an electron-positron pair, by a process called pair production [Kno00]. During pair production, the photon undergoes an energy-mass conversion to produce one electron and one positron, as shown in Figure 2.8. The newly produced electron and positron will travel in opposite directions. The positron will most likely interact with a different electron and the two will annihilate, releasing two photons, each with energy 511

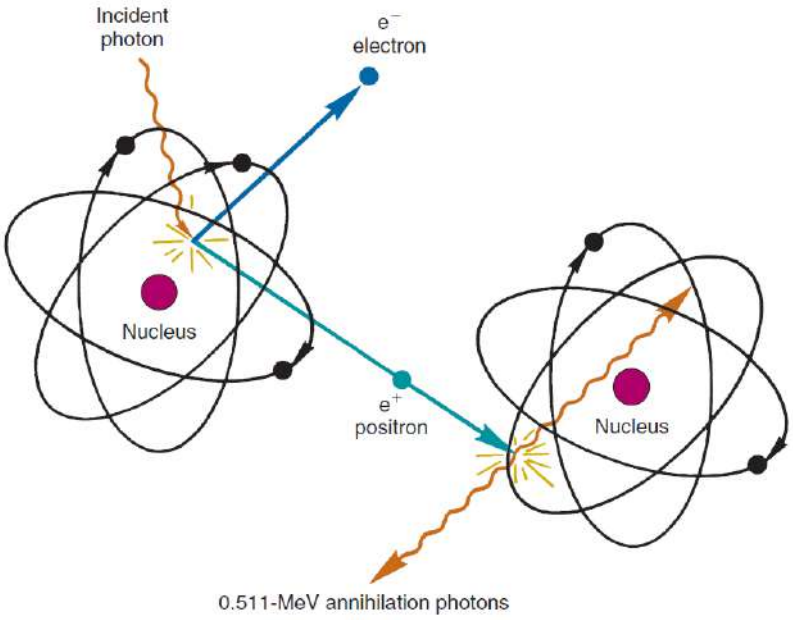

Figure 2.8: A schematic representation of pair production [CSP12]

keV [BB11]. If the gamma ray initially had an energy greater than 1.022 MeV, the electron-positron pair will use the excess energy as kinetic energy. Ultimately, the incident photon disappears and, aside from a bit of recoil, the nucleus will remain unchanged.

2.8 Detectors

2.8.1 Band Theory

Considering the atomic model in which electrons orbit the nucleus in discrete shells, where each shell is associated with a particular energy level, the outermost shell is known as the valence shell or valence band. In the valence band, electrons are bound to the atom and they are unable to move freely. If an electron in the valence band is given enough energy, it can enter the conduction band, where it is no longer bound to the atom and is able to move freely. The band gap is the amount of energy that is required for an electron in a particular atom to leave the valence band and enter the conduction band. When an electron leaves the valence band to enter the conduction band, it leaves behind a “hole” in the valence band that acts as a positive charge carrier.

All atoms can be classified as either conductors, insulators or semiconductors. For conductors, the band gap is very small to non-existent. The valence band and the conduction band overlap and the electrons require little to no energy to enter the conduction band and conduct electricity. The band gap is too large in insulators for electrons to leave the valence band and enter the conduction band. Insulators cannot conduct electricity. Semiconductors have a small band gap. Thermal energies are normally sufficient to excite the electrons from the valence band to the conduction band for semiconductors.

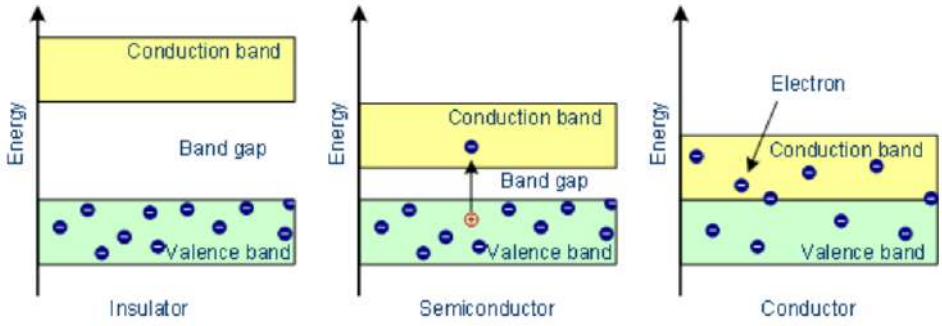

Figure 2.9: The band gap for semiconductors compared to conductors and insulators [Sta]

2.8.2 Semiconductor Detectors

Semiconductor detectors consist of a p-n junction diode where there is an n-type semiconductor joined to a p-type semiconductor. Both types are made from the same semiconductor material. Due to doping, the majority charge carriers in the two types differ. The terms p-type and n-type, when used with semiconductors, simply refer to the manner in which the semiconductor is doped. Germanium has four valence electrons which it uses to form four covalent bonds. For p-type, the semiconductor is doped with atoms of fewer valence electrons, for example boron or lithium. Thus, a hole is created. Electricity is primarily conducted, in a p-type semiconductor, by the movement of these holes. For n-type, the semiconductor is doped with atoms with one more valence electron such as phosphorous. The movement of the additional valence electrons is used for the conduction of electricity in n-type semiconductors. Both types of semiconductors are electrically neutral. In the n-type semiconductor the majority charge carriers are electrons.

In the p-type semiconductor the majority charge carriers are holes. An electron in the conduction band is a negative charge carrier. A hole in the valence band is a positive charge carrier.

In a p-n junction diode, a "depletion" region exists along the junction between the n-type and p-type semiconductors as shown in Figure 2.10. Along the junction, the holes from the p-type semiconductor can recombine with the electrons from the n-type semiconductor, creating the depletion region. In the depletion region there are no holes and no electrons that can move freely. There are no free charge carriers in the depletion region. The depletion region acts as the detector.

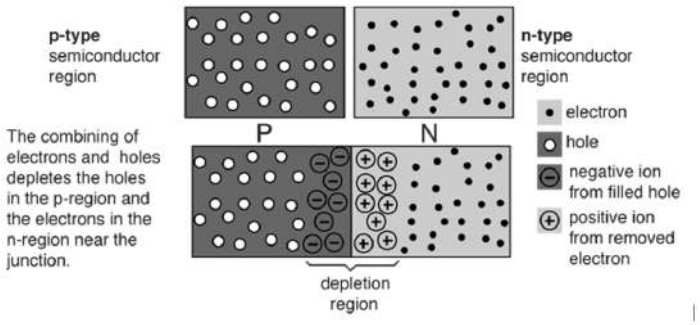

Figure 2.10: The depletion region created in a p-n junction diode [Lau]

A reverse bias is applied to enlarge the depletion region. A reverse bias is created by connecting the p-n junction diode to an external circuit that consists of a high voltage power supply and a resistor. Specifically, the p-type semiconductor will be connected to the negative terminal of the power supply and the n-type semiconductor will be connected to the positive terminal of the power supply. This way the current in the circuit is minimal. Due to the opposite polarities, the charge carriers are attracted in opposite directions resulting in a larger depletion region [Mir].

The reverse bias is therefore necessary for two important reasons. Firstly, it minimises the current in the circuit. This way the main current that is detected will be due to the gamma radiation interacting with the detector material. Secondly, the reverse bias enlarges the depletion region, which acts as the detector. The potential drop across the resistor and the current associated with the resistor

is monitored.

When a gamma ray enters the depletion region, it interacts with the electrons, transferring large amounts of energy, greater than 100 keV. The electrons in germanium only require a few electron-volts to enter the conduction band, so many electrons will be ionized by a single gamma ray. When gamma rays ionize the electrons in the depletion region, the electrons enter the conduction band, leaving holes in the depletion region.

The electrons, from the depletion region, that have entered the conduction band are then free to enter the circuit, connected to the p-n junction diode. This movement of charge, or flow of current, creates a potential drop across the resistor which can be measured. A current pulse, proportional to the energy transferred between the gamma ray and the electrons, can be detected. Semiconductor detectors are highly efficient at resolving peaks for radiation events. These detectors can therefore be used for energy-selective radiation counting. Semiconductor detectors such as the HPGe detector have much better energy resolution compared to scintillation detectors like NaI detectors.

Chapter 3

Experimental Methods

3.1 Sample Location and Collection

Thirty-eight soil samples were obtained in Ijero between January and March in 2015. The sample locations were chosen randomly every 500 to 1000 metres. Rivers, refuse dumps, rocky areas and settlements were avoided during sample selection. Sample locations were identified using a global positioning system (GPS) and recorded. The sample locations are presented in Appendix D in Table D.1 [AP].

The top soil was removed. Thereafter, the soil was sampled 10 cm underground using a 1 metre auger. The soil was carefully removed from the auger and immediately placed into clean, labelled, baft material sample bags. The soil samples were then air-dried while still in the baft material sample bags for 30 to 40 days [AP]. The sample collection was performed by Dr Adewale Adesiyan and supplied through a collaboration with Prof Leslie Petrik, Mr Ryno Botha and the University of the Western Cape.

Of the soil samples obtained from Ijero, Nigeria, only 30 samples were stored at iThemba LABS. They were previously measured for gamma radiation at iThemba LABS.

For comparison, soil was also sampled from a garden in the Kraaifontein suburb of Cape Town as shown in Figure 3.1. The top 10 cm layer of soil was

displaced and soil below was scooped using a plastic 2 litre container, so that metal or foreign particles from a used shovel would not contaminate the soil. The soil was then poured through a sieve to remove fine pebbles and organic matter. Approximately 1 kg of soil was sampled from the garden.

(a) Scooping the soil (b) Sieving the soil

Figure 3.1: Garden sample

3.2 Sample Preparation

It is important to consider the sample geometry and detector placement during these measurements. The detector efficiency largely relies on a constant sample geometry and a constant detector-sample geometry. Varying these geometries would lead to inconsistencies when considering the number of events detected compared to the number of gamma ray photons emitted by the sample. The geometries and sample volumes must be maintained so that the solid angle between the detector and the sample remains constant.

The detector efficiency also depends on the energy of the incident gamma rays. Altering the sample geometry would affect the attenuation of gamma rays escaping the sample. Attenuation is largely due to the absorption and scattering of gamma rays within the sample. Gamma rays are attenuated due to their interactions within the sample by photoelectric absorption, Compton scattering and pair production. When this happens, the intensity of the gamma rays is decreased

before reaching the detector.

Therefore, it was necessary to maintain sample geometry, sample volume and detector-sample geometry for each sample. This was done using 24 cm^3 cylindrical pillbox containers. A circle was drawn on a sheet of plastic, that was secured to the detector, to ensure that the samples were continuously placed in the same position, thus maintaining the detector-sample geometry.

It is necessary to operate in a sterile laboratory environment when working with radioactive samples and sensitive measurements. For this reason, before the laboratory and apparatus were used, they were thoroughly cleaned using Contrad® concentrate and Sunlight® liquid.

After each sample went through its necessary preparation, the apparatus and the laboratory were cleaned once again to prevent cross contamination of the samples.

To decrease the cleaning and to limit exposure, the sample along with the mortar and pestle was taken outside for the crushing and sieving process as shown in Figure 3.2.

Initially, the samples were stored in sealed, plastic Ziploc® bags. They were poured from the Ziploc® bag, onto the sieve. Organic plant matter was removed from each sample at this stage. An unused, folded paper plate was used to line the inside of the mortar to prevent cross contamination of the samples. Any rocks or pebbles remaining on the sieve were poured into the paper plate lined mortar to be crushed and re-sieved as shown in Figure 3.3. This process was repeated three times.

During this process, it was only necessary to wear protective goggles, a lab coat and a surgical mask to prevent inhalation of and exposure to any radionuclides that could be present in the samples.

Once the soil and crushed rocks had been sieved multiple times, they were care-

fully dished into a single cupcake mould in a metal cupcake tray as shown in Figure 3.4. A cupcake tray was used as it was necessary to keep the samples separate and to oven dry each sample to remove any moisture. The moisture must be removed to prevent inconsistencies due to the additional mass of water and to keep the attenuation of gamma rays as constant as possible.

Each cupcake mould was numbered and the name of each soil sample was recorded, along with the number of the cupcake mould that it was placed in. After three days of crushing and sieving soil samples, all thirty Nigerian samples, and one garden sample, had been crushed and dished into cupcake moulds. At the end of each day, the cupcake tray, with as many samples as had been completed on that day was placed inside an oven and heated at 105°C for twenty hours.

After twenty hours had elapsed, the samples were removed and given time to cool. During this time, each pill container was labelled and weighed three times and each mass was recorded. Each soil sample was scooped into its 24 cm^3 pill container. The pill container was filled as full as possible for each sample to ensure consistent sample volume as shown in Figure 3.5. The pill container was then weighed three times and the mass was recorded each time. The scale used was a Sartorius® BP2100S laboratory scale. This was necessary to properly measure the mass of the soil sample. The standard deviation of the mean for all measurements was considered the "error" in the mass.

The pill containers were stored in the lab for only 21 days and sealed using tape. This was done to prevent the escape of ^{222}Rn and to allow the ^{226}Ra, ^{222}Rn and short-lived daughters of ^{222}Rn present in the sample to reach secular equilibrium. After 21 days, or approximately 7 half-lives of ^{222}Rn, it is expected that the activity of the daughters will have increased to equal the activity of the parent radionuclides. Thereafter, their activity will decrease at the same rate. It is at this point that the radionuclides have reached and subsequently exist in secular equilibrium [BB11].

In the meantime, the background measurements could be completed. The background was measured by closing the lead castle without a sample inside. This

measurement was conducted for approximately 66 hours. The second background measurement was modified by the addition of an empty pillbox, placed on the detector. The final modification of the background measurement was the use of a pillbox filled with still mineral water.

To measure the detector efficiency, reference samples of uranium-ore, thorium-ore and potassium chloride (U-ore, Th-ore and KCl) were used. The certificate information for each reference sample is given in Table 3.1. They were carefully dished into pill containers, labelled, sealed and weighed according to the same procedure followed for the soil samples, as shown in Figure 3.6.

Table 3.1: Certificate information for the Reference samples. The "Mass" column refers to the mass of the reference sample once it had been spooned into the pillbox.

Reference Sample	Activity Concentration (Bq/kg)	Mass (kg)	Code
U-ore	4940(30)	0.02163(1)	IAEA-RGU-1
Th-ore	3250(70)	0.02076(1)	IAEA-RGTh-1
KCl	16260(100)	0.02071(0)	5042020EM

A thin sheet of plastic with a circle drawn in its center was secured onto the detector to guarantee a constant detector-sample geometry. The reference samples were carefully placed on the detector, ensuring that the sample was perfectly centered on the circle, as shown in Figure 3.7. The lead castle was closed and the reference samples were measured for 24 hours each.

Once 21 days had elapsed, the soil samples were placed on the detector using the same method as for the reference samples. Each sample was measured for 24 hours.

3.3 The HPGe detector at iThemba LABS

Germanium has a relatively large atomic number of 32. Therefore, it will have a large linear attenuation coefficient, which corresponds to a short mean free path

and improved detection efficiency [Mas]. However, impurities in relatively "pure" crystals interfere with the positioning of germanium atoms. This interference leads to the creation of electron traps that catch electrons, decreasing the electrical signal available for detection. For this reason, detector thickness is practically limited to 1 cm, which restricts the detection efficiency [CSP12].

To combat the impurity problem, high-purity germanium crystals are specifically produced for use in detectors. These crystals are then refined by a process called the zone refining technique. During this process, radio frequency heating coils are used to heat and melt the germanium. All impurities will be removed as they remain in the molten zone, while the purified germanium solidifies [Mas].

Another solution to the impurity problem is the deliberate doping of detector crystals. Lithium ions are used for doping germanium crystals. Unfortunately, Lithium condenses at room temperature, ruining the germanium crystal. Therefore, the HPGe detector is constantly cooled, using liquid nitrogen. The cooling also decreases the thermal noise produced by the germanium detector.

The doping of the semiconductor results in an excess of holes, which, owing to the electric field, created by the reverse bias, will travel to the n electrode as the electrons move towards the p electrode. The movement of charge across the detector is related to the energy imparted to the detector material by the photons. An integral charge sensitive preamplifier performs the translation from charge to energy imparted during the event.

The HPGe detector used in this study is a Canberra p-type GC4520 detector, based at iThemba LABS, in the Environmental Radiation Laboratory (ERL). The detector primarily consists of a cylinder of germanium with an n-type contact on the outer surface and a p-type contact on the inner, cylindrical surface as illustrated in Figure 3.8. A more detailed diagram of the HPGe detector used in this study is shown in Figure 3.9. It has been customised to measure samples of low activity [NRF][New+08].

HPGe detectors have an n-type outer layer. When a reverse bias is applied across

the detector, a depletion region is formed across the intrinsic region. For accurate measurements using an HPGe detector, the detector crystal must be free of impurities and the crystalline structure should be perfectly undisturbed.

The detector crystal is enveloped in a cup, usually aluminium. Inside the cup, the detector crystal is seated in a vacuum. The cup protects the crystal but is thin enough to allow for the penetration of gamma rays. Additionally, the crystal is connected to a coldfinger which is submerged in liquid nitrogen inside the dewar, as shown in Figure 3.9. This keeps the detector at a constant temperature of approximately 77 K. Together, the cup and the coldfinger is called the cryostat. The cryostat ensures reproducibility of results by preventing contamination and thermal noise. This maintains the high energy resolution of the HPGe detector.

The housing of the germanium crystal has electrical feedthroughs so that the high voltage supply can be connected directly to the detector crystal. The high voltage supply must be gradually increased, at around 100 V/s, so as not to damage the crystal.

The detector was shielded by a lead castle that was approximately 10 cm thick as shown in Figure 3.7. Lead has a high atomic number and for that reason it is useful for the attenuation of gamma rays. The shielding protects the detector from any background radiation that could influence the spectra. This background radiation comes from extra-terrestrial, terrestrial and anthropogenic sources.

The sample was placed directly on top of and in the centre of the HPGe detector as shown in Figure 3.7. It can be assumed that the radioactive sample emits gamma rays isotropically. Therefore the gamma rays may undergo photoelectric interactions with the detector as well as the shielding. The gamma ray could excite the lead atoms in the shielding. When they de-excite, they will emit a characteristic X-ray. The X-ray could escape the lead and be detected by the detector in the 75 to 80 keV region. On the inside, the shielding is lined with copper to attenuate these X-rays. It could also attenuate the gamma rays that have back-scattered from the shielding into the detector.

3.4 Electronic Setup

The high voltage power supply used was the SILENA MOD. 7716. The voltage applied was 3.50 kV. Since the detector has an internal preamplifier, only an external amplifier was necessary. The external amplifier used was the ORTEC 572, as shown in Figure 3.10. The make, model and settings for each electronic device is shown in Table 3.2.

The high voltage power supply, SILENA model 7716 is a NIM module and is designed specifically for high energy resolution semiconductor detectors. It can supply up to ±6 kV of bias voltage. The high voltage supply is stable with low frequency noise, under 5 mV [SIL].

The internal preamplifier was the CANBERRA Model 2002 Ge detector preamplifier. It is designed for high energy resolution gamma spectroscopy. It is a low noise, high speed preamplifier. When a nuclear event occurs within the detector material, the preamplifier converts the total charge accumulated during that event into a step-function output pulse. The amplitude of the pulse is proportional to the charge accumulated in the event. The input circuits are cooled by the cryostat to decrease noise. This creates an integral detector/preamplifier assembly. It can also be coupled directly to the detector [Can04].

The ORTEC 572 is a NIM module and a general purpose amplifier for energy spectroscopy. It can be used with any type of detector, but it is well suited to germanium detectors [Per04]. Amplifiers amplify and shape the signals, from the preamplifier and detector setup, by increasing the pulse amplitudes and eliminating noise from the pulse. Gain is the ratio of the output pulse to the input pulse amplitude. The fine gain was set to 1.2, the coarse gain was set to 20 and the shaping time was set to 6 μs.

The multi-channel analyser used to collect and generate spectra in this study was the Palmtop MCA 8k-01, shown in Figure 3.11. It is specially designed for nuclear radiation detectors. Its features include dead-time and pile-up loss correction which ensures precise measurements of gamma ray intensity. The device is easily

portable as it has small dimensions and only requires a USB port for power [Ato]. The software for the Palmtop MCA can be installed on a desktop or laptop with a Windows operating system.

Table 3.2: Settings for the HPGe electronics.
*Detection system consists of the HPGe detector, the nitrogen dewar and the internal preamplifier

Item	Module no.	Make	Settings
HV-supply	MOD 7716	SILENA	3.50 kV
Detection system*	P-type GC4520	CANBERRA	
Preamplifier	2002 CSL	CANBERRA	
Amplifier	572	ORTEC	Gain: 1,2; coarse gain: 20; shaping time: 6 μs
Pamltop MCA	serial: 0202	Atomki	

The Palmtop MCA software allows the user to set regions of interest (ROIs) across peaks in the spectrum. It highlights and saves ROIs for use in subsequent spectra. Additionally, it requires the user to perform an energy calibration using peaks in the spectrum.

The software instantly calculates the gross counts as well as the net counts in the peak which it displays as "Integral" and "Net Area". For the removal of the Compton continuum, caused by Compton scattering during measurement, it assumes a linear background using the counts at the start and end of the ROI. It calculates the net area using the counts in the ROI after subtracting the linear background [Ato].

Subsequently, it calculates the uncertainty in its calculation for both the gross and net counts. The uncertainty for the net area is calculated automatically according to equation 3.1 [Ato].

$$E_N = \frac{100 \times \sqrt{(A - S - E) + (\frac{K-2}{2})^2 \times (S + E)}}{A - \frac{K}{2} \times (S + E)} \tag{3.1}$$

where

E_N is the uncertainty in the net area;

A is the gross area of the ROI;

S is the contents of the first ROI channel;

E is the contents of the last ROI channel and

K is the number of channels of the ROI.

(a) The transfer of soil from the Ziploc® bag

(b) Grind soil using mortar and pestle

(c) Sieving

Figure 3.2: The crushing and sieving process

(a) Sieving Apparatus used

(b) Paper plate inside the mortar

(c) The soil on the sieve

Figure 3.3: The crushing and sieving apparatus

(a) The soil poured to be re-sieved

(b) The sieve after only fine pieces of rock remain

(c) The soils in the cupcake tray

Figure 3.4: The transfer of ground soil into the cupcake tray

(a) Apparatus used to transfer soil to pill containers

(b) Mass measurement

(c) Sealed sample

Figure 3.5: The transfer of the soil into the pill container

(a) KCl reference material

(b) uranium-ore reference material

(c) thorium reference material

(d) sealed reference samples

Figure 3.6: Reference materials

(a) Soil sample placed on the HPGe detector

(b) Plastic for detector

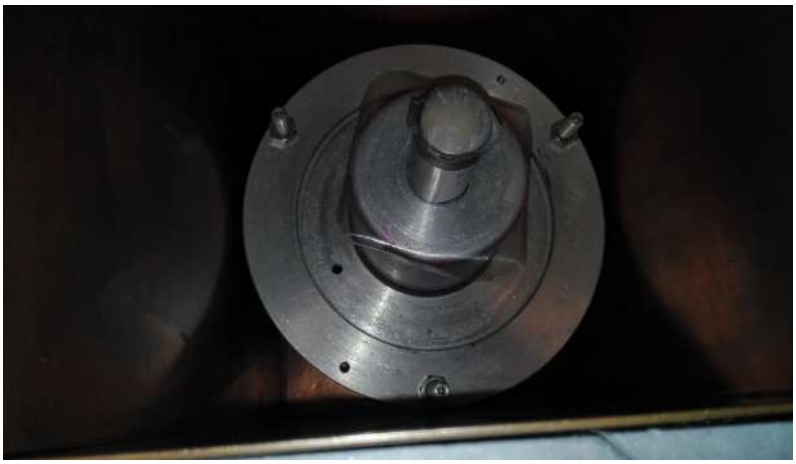

(c) Plastic secured to detector

Figure 3.7: The method used to ensure consistent sample geometry

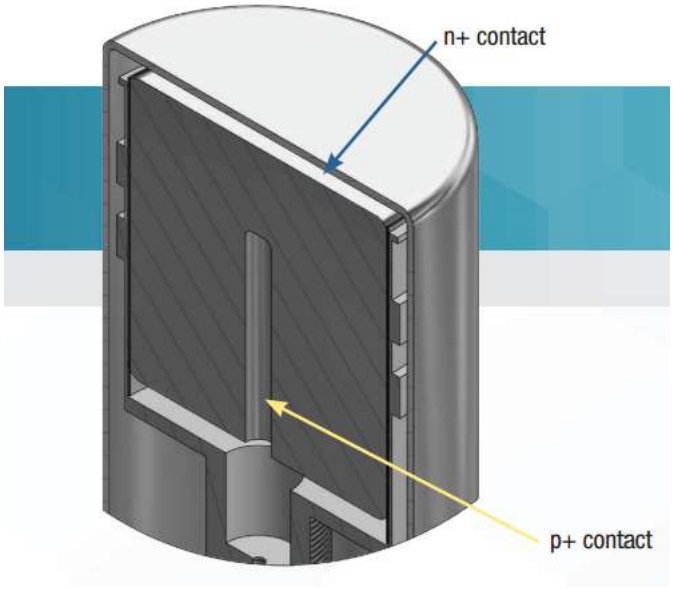

Figure 3.8: Simplified diagram showing the structure of an HPGe detector [Mir]

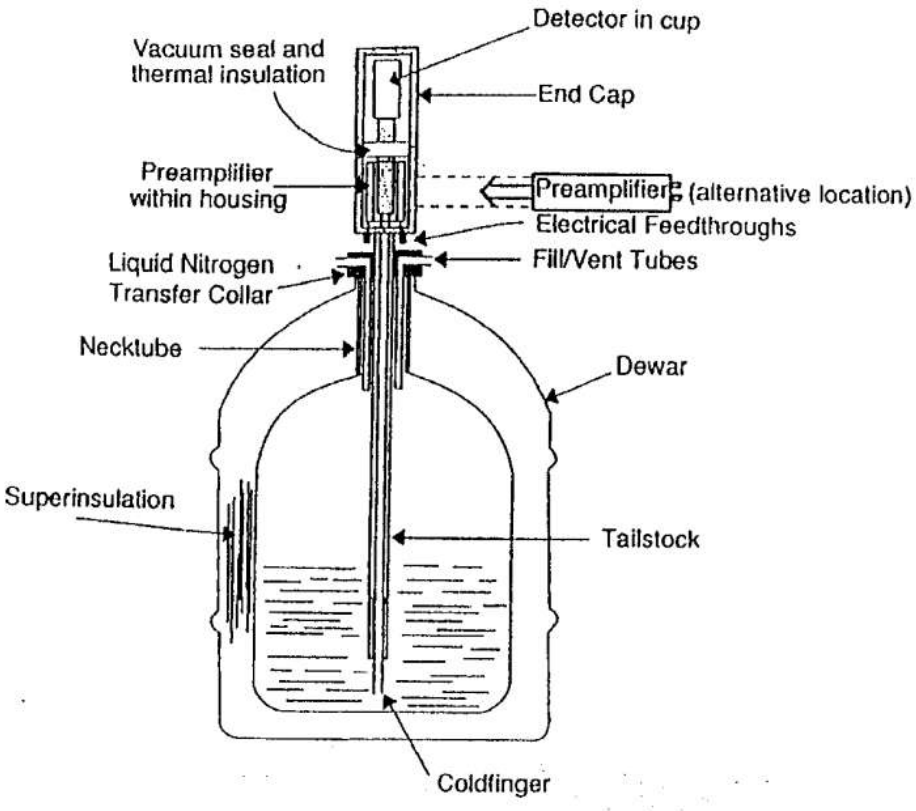

Figure 3.9: Basic diagram of an HPGe detector [Mas]

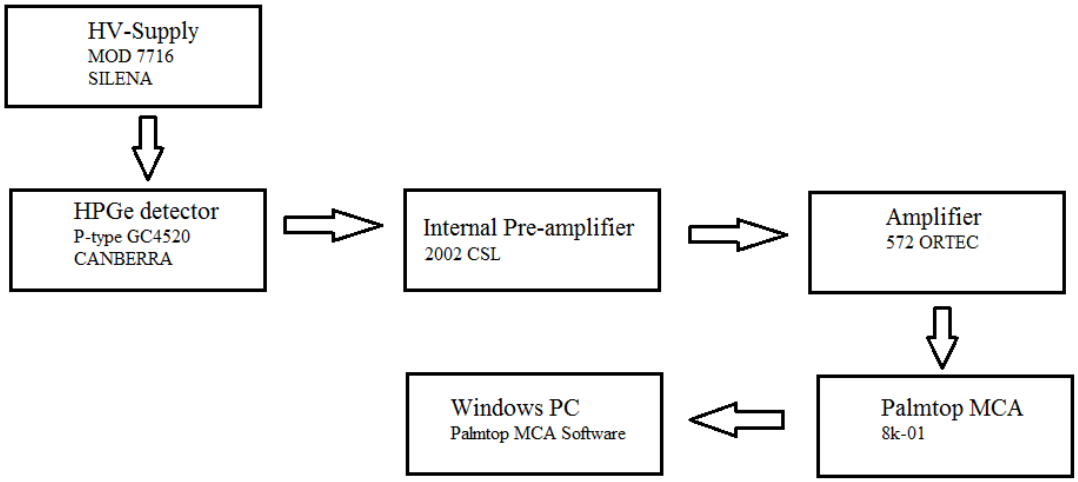

Figure 3.10: The setup for the detection system

Figure 3.11: The Palmtop MCA [Ato]

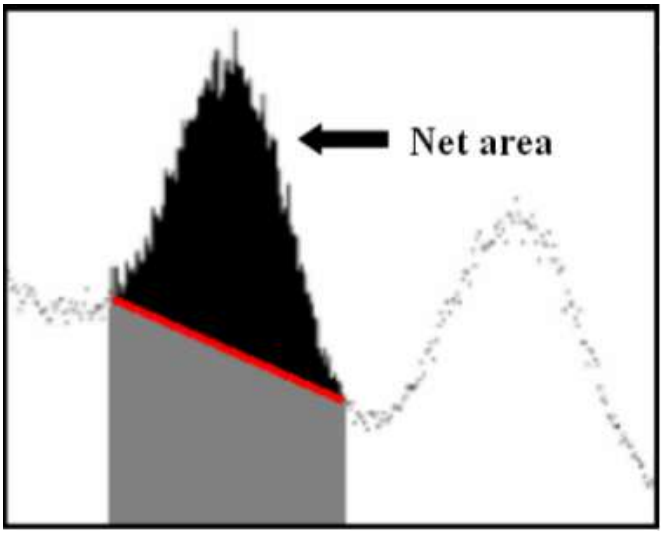

Figure 3.12: The net area [Ato]

(a) Detector system and external electronic modules

(b) Palmtop MCA

(c) computer and monitor for spectra

Figure 3.13: The detector and spectra acquisition system

Chapter 4

Data Analysis

4.1 Gamma Emission Probability

As previously illustrated, some radionuclides have long decay chains with multiple emissions and emission probabilities. For the relevant decay chains, it was shown that certain radionuclides were only gamma emitters while others were alpha, beta and gamma emitters. Gamma rays are emitted with a characteristic energy and an associated gamma emission probability.For the calculation of activity concentration of a given radionuclide, using gamma spectrometry, the gamma emission probability is required.

The full-energy peak at 1001 keV, associated with the ^{234}Pa decay was analysed, but unfortunately found to be below detectable limits after background subtraction. The next gamma-ray emitting radionuclide in the ^{238}U series is ^{226}Ra. The 186 keV gamma-ray associated with the decay of ^{226}Ra could be measured above background. This gamma ray and gamma rays associated with daughter radionuclides of ^{226}Ra were used to determine an average activity concentration for the ^{238}U series radionuclides. For this work, it was assumed that there is secular equilibrium in the ^{238}U decay series.

The full-energy peaks used for the calculation of activity concentration for the ^{238}U series were those at 186 keV, associated with the decay of ^{226}Ra, and at 295 and 351 keV, associated with the decay of ^{214}Pb. For the activity concentration of the ^{232}Th series, the full-energy peaks used were those at 238 keV, associated

with the decay of ^{212}Pb, and 338 and 911 keV associated with the decay of ^{228}Ac. Full-energy peaks that the detector could resolve and did not overlap were selected.

For this study, the emission probabilities in literature were compared. The emission probabilities from literature are shown in table 4.1.

Table 4.1: The gamma emission probabilities for the full-energy peaks used in the activity concentration calculation from several reliable sources.

Series	Radionuclide	Energy (keV)	IAEA [IAE]	Firestone [FEC99]
^{238}U	^{226}Ra	186	0.0364±0.0004	0.0359±0.0006
	^{214}Pb	295	0.1842±0.0004	0.193±0.002
	^{214}Pb	351	0.356±0.0007	0.376±0.004
^{232}Th	^{212}Pb	238	0.436±0.005	0.433±0.004
	^{228}Ac	338	0.113±0.002	0.113±0.002
	^{228}Ac	911	0.258±0.004	0.258±0.004
^{40}K	^{40}K	1461	0.107±0.001	0.11

Series	Radionuclide	Energy (keV)	Gilmore [Gil08]	Newman [New+08]
^{238}U	^{226}Ra	186	0.0356	0.0617
	^{214}Pb	295	0.185	0.185
	^{214}Pb	351	0.356	0.358
^{232}Th	^{212}Pb	238	0.436	0.433
	^{228}Ac	338	0.113	0.113
	^{228}Ac	911	0.258	0.266
^{40}K	^{40}K	1461	0.107	0.107

Notice the variation in the gamma emission probability for the 186 keV full-energy peak in Table 4.1. The IAEA [IAE], Firestone [FEC99] and Gilmore [Gil08] all report it as approximately 0.036. Newman et al. [New+08] states that the activity concentration calculation for ^{238}U yields more accurate results when 0.0617 is used as the effective branching ratio. This effective branching ratio accounts for the ^{235}U contribution to the ^{226}Ra full-energy peak at 186 keV.

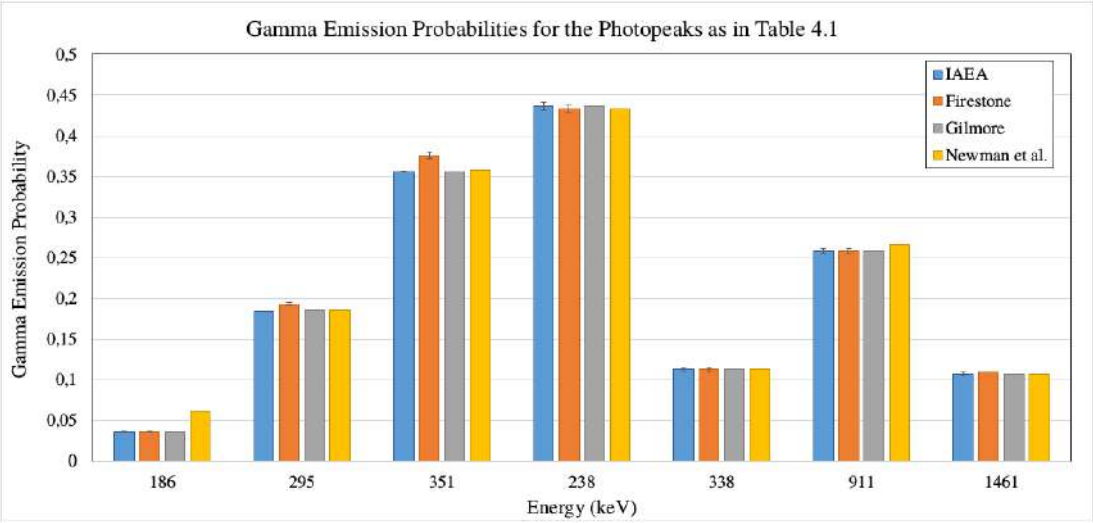

Figure 4.1: The gamma emission probabilities as in Table 4.1.

^{235}U and ^{226}Ra are both present in natural samples. The principal isotopes of uranium present in the Earth's crust are ^{235}U with natural abundance of 0.72% and ^{238}U with natural abundance of 99.27%. ^{226}Ra, the daughter radionuclide of ^{238}U, emits a photon with energy 186.2 keV. Additionally, ^{235}U emits a photon with energy 185.7 keV [Eba10]. The energy resolution of the HPGe detector is not good enough to resolve these two peaks.

Once the count rate, the specific activity and the natural abundance of the radionuclides involved was considered, the calculation of the effective branching ratio was performed accordingly. The calculation can be seen in Appendix B. The result for the effective branching ratio of ^{226}Ra was 0.0637, which is comparable to the value obtained by Newman et al. Thus, 0.0637 is the value that is used as the effective gamma emission probability for the 186 keV full-energy peak in this study.

4.2 Background

For the evaluation of health risks due to ^{238}U, ^{232}Th and ^{40}K, it is necessary to calculate the activity concentration of each radionuclide in the soil sample. This calculation requires a precursory background radiation subtraction and detector efficiency calculation.

Twenty-one soil samples were analysed in 2017 and the remaining eight samples, including a control sample, were analysed in 2018. In 2019, samples from 2017 were measured a second time to test the reproducibility of the results. The results of the re-measurement can be seen in Appendix D in Table D.2 and Figures D.1 to D.3. A background measurement was performed each year.

In 2017, the background was measured with an empty, closed lead castle.

In 2018, a few background measurements were performed to determine the optimal background measurement technique. Each background measurement took place over a weekend at iThemba LABS. The first background measurement was performed with an empty, closed lead castle. For the second background measurement, an empty pillbox was placed on the detector. The final background measurement involved a pillbox filled with still mineral water. Each pillbox was identical to the ones used for the soil samples. The pillboxes were placed in the same position as the soil samples.

In comparison, the background measured with the empty closed lead castle was slightly lower than the background measured with the empty pillbox. This could be due to photon scattering. It could happen that gamma rays that would have normally missed the detector, instead scattered off of the pillbox into the detector. Additionally, gamma rays that may have escaped the detector material without the pillbox, could be scattered off of the pillbox back into the detector material. The background measurement that involved the pillbox filled with mineral water resulted in the highest background measurement. The reason for this is very similar to the empty pillbox, that is, the photons could be scattering into the detector. Another aspect to be considered is that the water that was used was not pure water. It was bottled mineral water from a natural spring that had been filtered and UV treated. Since it was from a natural spring, it consisted of various minerals, such as calcium, magnesium and potassium. Plots showing the comparison of background measurements can be seen in Appendix C.

Ultimately, the empty closed lead castle setup was used for the precursory back-

ground subtraction required for the activity concentration calculation in 2018. This choice was made so that the background setup in 2018 was as similar as possible to the background setup in 2017.

In 2019, 3 samples from the first 21 samples, that is, the original, 2017 soil samples, were remeasured to test the reproducibility of the results obtained originally. For this measurement, the background was measured with an empty closed lead castle as well as with an empty pillbox to demonstrate how the 2017 samples' activity concentration would be altered with an improved setup for the background measurement.

When analysing the soil samples, the background measured in 2017 with an empty closed lead castle was used for the activity concentration calculation of the first 21 samples, measured in 2017. The background measured in 2018 was used for the activity concentration calculation performed for the samples that were measured in 2018. The same can be said about the background measured in 2019 for the activity concentration calculation of the 2019 samples, that were simply re-measurements of 2017 samples.

Since the background was always measured over the weekend, the counts were scaled according to the measurement time for each soil sample. The background measurements were about 60-80 hours long, whereas the soil measurements were 24 hours or 86400 seconds long. When performing the background subtraction on the counts, the counts in the background spectrum were multiplied by 86400 and divided by the length of time for the background measurement. For example, in 2019 the background measurement lasted 230528 seconds.

$$N_i = N_{spec} - N_{bg}\left(\frac{86400}{230528}\right) \tag{4.1}$$

where

N_i is the counts after background subtraction (net counts);

N_{spec} is the counts in the full-energy peak in the soil gamma spectrum (gross counts) and

N_{bg} is the counts in the full-energy peak in the background gamma spectrum.

4.3 Detection Efficiency

Before we can begin to analyse the gamma spectra for the activity concentration calculation, there is one last important measurement that must be conducted. This is the determination of the absolute full-energy peak efficiency at different gamma energies for this detector.

This measurement is performed using reference samples of known radionuclide composition and activity concentration. The spectrum was obtained for each reference material. Conveniently, the reference samples have clear, well-defined full-energy peaks which are also used in the energy calibration of the spectra.

Since the activity of the reference samples is given by the reference material certificates, the detector efficiency at a given energy can be calculated using the activity concentration formula as follows

$$A = \frac{N_i}{L_T \times B_r \times \epsilon \times m} \tag{4.2}$$

$$\epsilon = \frac{N_i}{L_T \times B_r \times A \times m} \tag{4.3}$$

where

ϵ is the absolute full-energy peak efficiency;

N_i is the net counts in the full-energy peak after background subtraction;

L_T is the live time of the detector system in seconds;

B_r is the gamma-ray emission probability;

A is the activity concentration in Bq/kg and

m is the mass of the sample in kg.

The reference samples were measured in 2017, 2018 and 2019 and the detector efficiency was calculated each year. The results are shown in Table 4.2. The detector efficiency is a function of energy. Therefore the results can be plotted, producing an efficiency curve as in Figure 4.2.

For each year, the activity concentration of ^{238}U, ^{232}Th and ^{40}K was calculated using the efficiency values obtained in that year.

Table 4.2: Detector efficiency results for 2017, 2018 and 2019

Series	Radionuclide	Energy (keV)	Efficiency 2017	Efficiency 2018	Efficiency 2019
^{238}U	^{226}Ra	186	0.0654±0.0007	0.0701±0.002	0.0707±0.002
	^{214}Pb	295	0.0447±0.0003	0.0492±0.0005	0.0502±0.0005
	^{214}Pb	351	0.0421±0.0003	0.0442±0.0003	0.0443±0.0004
^{232}Th	^{212}Pb	238	0.0526±0.001	0.0663±0.002	0.0659±0.002
	^{228}Ac	338	0.0405±0.0009	0.0421±0.001	0.0411±0.0009
	^{228}Ac	911	0.0187±0.0004	0.0190±0.0005	0.0186±0.0004
^{40}K	^{40}K	1461	0.0126±0.0001	0.0126±0.0001	0.0129±0.0001

The uncertainty in the activity concentration calculation was propagated through the uncertainties in the efficiency, the mass of the soil samples as well as the counts in the spectra. Equation 4.4 shows the formula used to calculate the uncertainty in the counts, after background subtraction. Equation 4.5 shows the formula used to calculate the uncertainty in the absolute detector efficiency. Finally, equation 4.6 is the formula used to calculate the uncertainty in the activity concentration [Kno00]. These formulae were used for every full-energy peak analyzed for every sample, including the reference samples.

$$\delta N_i = \sqrt{(\delta N_c)^2 + (\delta N_{bg})^2} \tag{4.4}$$

$$\delta\epsilon = \epsilon\sqrt{\left(\frac{\delta N_i}{N_i}\right)^2 + \left(\frac{\delta A}{A}\right)^2 + \left(\frac{\delta m}{m}\right)^2} \tag{4.5}$$

$$\delta A = A\sqrt{\left(\frac{\delta N_i}{N_i}\right)^2 + \left(\frac{\delta\epsilon}{\epsilon}\right)^2 + \left(\frac{\delta m}{m}\right)^2} \tag{4.6}$$

where

δN_i is the uncertainty in the net counts;

δN_c is the uncertainty in the counts in the spectrum;

δN_{bg} is the uncertainty in the counts in the background spectrum;

$\delta\epsilon$ is the uncertainty in the absolute detector efficiency;

ϵ is the absolute detector efficiency;

N_i is the net counts;

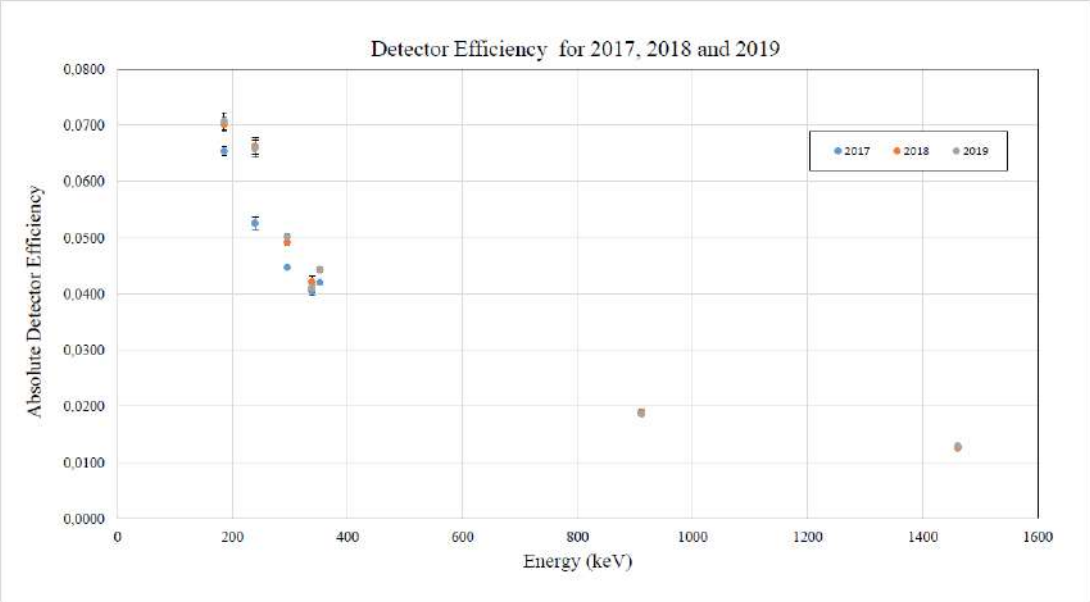

Figure 4.2: The absolute detector efficiency values for 2017, 2018 and 2019

δA is the uncertainty in the activity concentration;

A is the activity concentration;

δm is the uncertainty in the mass and

m is the mass.

4.4 Radiological Risk Formalism

Once the soil samples have been measured, using the HPGe detector and Palmtop MCA, the spectra are analysed and the activity concentrations of the primordial radionuclides ^{238}U, ^{232}Th and ^{40}K are calculated using the window analysis method [New+08].

The activity concentrations are subsequently used to calculate radiological hazards using pre-defined radioactivity formulae. These radiological hazards specify the permissible limits and the dangers present when these limits are exceeded.

4.4.1 Radium Equivalent Activity (Ra_{eq})

The primordial radionuclides are, generally, not uniformly distributed throughout the soil. To take this into account, the radium equivalent activity, Ra_{eq} is calculated. It is essentially a weighted sum of activity concentrations [Pen+18],

whereby it is assumed that 370 Bq/kg of ^{226}Ra, 259 Bq/kg of ^{232}Th and 4810 Bq/kg of ^{40}K produce the same gamma dose rate.

The radium equivalent activity considers both the external gamma dose and the internal alpha dose from radon and its daughters [DAE15]. Although secular equilibrium has been reached in the ^{238}U series, there may be disequilibrium between ^{238}U and ^{226}Ra. However, it is accepted, for this study, to replace ^{226}Ra with ^{238}U for A_U in Equation 4.7. Then the assumption is that 370 Bq/kg of ^{238}U, 259 Bq/kg of ^{232}Th and 4810 Bq/kg of ^{40}K produce the same gamma dose rate [Ama+17].

$$Ra_{eq}(Bq/kg) = A_U + 1.43A_{Th} + 0.077A_K \tag{4.7}$$

where A_U, A_{Th} and A_K are the activity concentrations (in Bq/kg) of ^{238}U, ^{232}Th and ^{40}K respectively [NRF17b].

The maximum acceptable limit for radium equivalent activity is 370 Bq/kg. This value corresponds to the maximum permissible limit for a member of the public, 1 mSv/yr [UNS00].

4.4.2 Hazard Indices

The soil and mine tailings in Ijero are frequently used in building materials [Usi+19]. It can be assumed that these bricks are made with soil from the same region as the soil samples collected in this study [Usi+19]. Residents of Ijero are exposed to radiation in their homes due to the presence of primordial radionuclides in the building materials.

The hazard indices quantify the radiation dose to an individual in these circumstances.

The external hazard index considers the external dose due to gamma radiation from building materials.

Multiple authors use the model of a room in a house with infinitely thick walls and

no windows or doors [Pen+18][DAE15][Ama+17]. For this model, the external hazard index can be calculated according to the following formula [UNS00]:

$$H_{ex} = \frac{A_U}{370} + \frac{A_{Th}}{259} + \frac{A_K}{4810} \tag{4.8}$$

A modified version of this model is one in which the walls are of finite thickness and windows and doors are present, resulting in enhanced ventilation. This decreases the activities to half of their original value. Using this model, the external hazard index is calculated according to the following formula [DAE15]:

$$H_{ex\prime} = \frac{A_U}{740} + \frac{A_{Th}}{518} + \frac{A_K}{9620} \tag{4.9}$$

The internal hazard index considers the internal dose due to inhalation or ingestion of alpha particles from the decay of ^{222}Rn, ^{220}Rn and their daughters in the construction materials.

The internal hazard index can be calculated according to the following formula:

$$H_{in} = \frac{A_U}{185} + \frac{A_{Th}}{259} + \frac{A_K}{4810} \tag{4.10}$$

For the hazard indices to be considered insignificant, they must be less than one. This limits the dose due to gamma and alpha particles to a permissible limit of 1 mSv/yr.

4.4.3 Absorbed Dose rate in air (D)

According to UNSCEAR 2000, the absorbed dose rate in air, due to gamma radiation is estimated at a height of 1 m above the ground's surface, assuming a uniform distribution of primordial radionuclides [Ama+17].

Conversion factors are used to convert the units of activity concentration (Bq/kg) to the units of outdoor absorbed dose rate (nGy/hr). These conversion factors are 0.462, 0.604 and 0.0417 (nGy/hr per Bq/kg) for the activity concentration of the ^{238}U series, ^{232}Th series and ^{40}K respectively citemasok. It is assumed that the contribution from other external radiation is insignificant.

$$D_{out}(\text{nGy/hr}) = 0.462A_U + 0.604A_{Th} + 0.0417A_K \tag{4.11}$$

Considering again that the construction materials are locally sourced and primarily made from soil, rocks, sediment and clay [Jib+16], the absorbed dose rate indoors must be analysed.

The model used to calculate indoor absorbed dose rates is intended for a room with dimensions $4 \times 5 \times 2.8$ m^3 and walls approximately 20 cm thick [Jib+16]. Since the absorbed dose rate is calculated for a confined space and is primarily due to the construction materials, new conversion factors are used.

The conversion factors for activity concentration to indoor absorbed dose rate in air are 1.21, 1.29 and 0.1 (nGy/hr per Bq/kg) for ^{238}U, ^{232}Th and ^{40}K respectively.

$$D_{in}(nGy/hr) = 1.21A_U + 1.29A_{Th} + 0.1A_K \tag{4.12}$$

4.4.4 Annual Effective Dose rate (AED)

Still, the dose absorbed in air is not a direct indication of the dose absorbed by an individual. UNSCEAR 2000 calculates the annual effective dose using the absorbed dose rate in air and a number of additional constants. The first of the these is 0.7×10^{-6} Sv/Gy which is a conversion factor from absorbed dose in air to effective dose to an individual.

Additionally, it is necessary to consider the outdoor annual effective dose as well as the indoor annual effective dose. Therefore occupancy factors are required. It is assumed that the average individual spends 80% of their day indoors and 20% of it outdoors. The indoor and outdoor occupancy factors are therefore 0.8 and 0.2 respectively [Ama+17].

Finally the equation is multiplied by the number of hours in a year. This is calculated as $24(\text{hr/day}) \times 365.25(\text{day/yr}) = 8766(\text{hr/yr})$ [DAE15].

$$AED_{in}(mSv/yr) = D_{in}\ (nGy/hr) \times 8766(hr/yr) \times 0.8 \times 0.7 \times 10^{-6}(Sv/Gy) \tag{4.13}$$

$$AED_{out}(mSv/yr) = D_{out}\ (nGy/hr) \times 8766(hr/yr) \times 0.2 \times 0.7 \times 10^{-6}(Sv/Gy) \tag{4.14}$$

The maximum permissible value for annual effective dose rate is 1mSv/yr for a member of the public, that is $AED_{in} + AED_{out} < 1mSv/yr$ [Mas+18].

4.4.5 Annual Gonadal Equivalent Dose (A_G)

The cells of the gonads (reproductive organs), active bone marrow and bone surface are the most radio-sensitive cells in the human body. The annual gonadal equivalent dose primarily evaluates the dose to these cells over the course of a year.

The constants 3.09, 4.18 and 0.314 convert the activity concentrations of ^{238}U, ^{232}Th and ^{40}K to the total dose received by the gonads [Pen+18] as shown.

$$A_G(\mu Sv/yr) = 3.09A_U + 4.18A_{Th} + 0.314A_K \tag{4.15}$$

The world average Annual Gonadal Equivalent Dose as well as the acceptable limit according to UNSCEAR is 300 μSv/yr [IAE].

4.4.6 Excess Lifetime Cancer Risk (ELCR) and Excess Percentage Risk (% Risk)

The Excess Lifetime Cancer Risk (ELCR) estimates the probability that an individual could develop cancer in their lifetime due to exposure to ionising radiation [Pen+18].

The calculation involves the previously calculated Annual Effective Dose Rate along with two constants. The first constant is 56, the average life expectancy in Ijero [WHO19]. The second constant is a risk factor, given by ICRP 103, that assumes a linear response to radiation at low doses, for stochastic effects, and states that the fatal cancer risk, is approximately 5% per Sv [Pro07] or 0.05×10^{-3} per mSv, for any given population [Pen+18].

The maximum permissible value for ELCR is 0.29×10^{-3} [Pen+18]. The equation used to calculate the ELCR is shown in Equation 4.16.

$$ELCR = (AED_{in} + AED_{out})\,(mSv/yr) \times 56\,yr \times 0.05 \times 10^{-3}(mSv^{-1}) \tag{4.16}$$

The ratio of the calculated ELCR to the upper recommended value of the ELCR is assessed in this study, using Equation 4.17. An acceptable value for the ratio

would be less than or equal to 1, where the ELCR result is less than or equal to the upper recommended value of 0.29×10^{-3}.

$$\text{ELCR Ratio} = \frac{\text{Calculated ELCR}}{\text{Maximum ELCR}} \tag{4.17}$$

Finally, the percentage deviation of the calculated ELCR from the maximum limit of the ELCR of 0.29×10^{-3} is determined and referred to as the excess percentage risk. The excess percentage risk is calculated by Equation 4.18.

$$\text{Excess \% Risk} = \frac{\text{Calculated ELCR - Maximum ELCR}}{\text{Maximum ELCR}} \times 100 \tag{4.18}$$

4.5 Data Processing

The calculations for the activity concentration and radioactivity formulae were performed using Microsoft Excel. Separate sheets were created for the background, detector efficiency, activity concentration and hazard indices.

The calculation of activity concentration was done according to equation 4.2.

Table 4.3 illustrates the method used to calculate the activity concentration for a given sample.

The weighted mean was calculated and reported as the activity concentration for that series as shown in Equation 4.19.

$$\bar{x} = \frac{\sum_{i=1}^{N} \frac{x_i}{\sigma_i^2}}{\sum_{i=1}^{N} \frac{1}{\sigma_i^2}} \tag{4.19}$$

$$\sigma_{\bar{x}} = \frac{1}{\sqrt{\sum_{i=1}^{N} \frac{1}{\sigma_i^2}}} \tag{4.20}$$

where

$\bar{x}$ is the weighted mean;

x_i is the activity concentration of a daughter radionuclide;

$\sigma_{\bar{x}}$ is the uncertainty associated with the weighted mean and

σ_i is the uncertainty associated with the daughter radionuclide.

Table 4.3: Table showing the calculation of the activity concentration for ^{238}U, ^{232}Th and ^{40}K

	Radionuclide	A_U	A_{Th}	A_K	Uncertainty
SOS4T	^{226}Ra	28.7			10.7
	^{214}Pb	26.2			2.5
	^{214}Pb	21.9			2.6
	^{212}Pb		74.2		2.8
	^{228}Ac		79.7		6.3
	^{228}Ac		86.7		4.6
	^{40}K			249	15
	weighted mean	24.3	77.7	249	
	uncertainty	1.8	2.2	15	
	χ^2	0.63	0.61		

The uncertainty in the activity concentration for each series is calculated by taking the uncertainty in the weighted mean of the activity concentration for the three daughter radionuclides, as shown in Equation 4.20.

The full-energy peak counts and the uncertainties for those counts were automatically calculated by the Palmtop MCA software, using the information from the ROIs. These values were entered into the spreadsheet. The net counts was calculated by the subtraction of the counts in the background spectrum, for that particular year, from the spectrum counts. The uncertainty in the net counts was calculated by propagation of uncertainties, using the uncertainties in the spectrum counts and the background's counts. Finally, the activity concentration was calculated. The uncertainty in the activity concentration was calculated using the uncertainties in the mass, the net counts and the detector efficiency.

A selection of the calculations of activity concentration for high, intermediate and low activity samples are tabulated in Table 4.4.

The activity concentration for the ^{238}U and ^{232}Th series was taken as the weighted mean activity concentration for three of their daughter radionuclides using Equation 4.19. For the activity concentration of ^{40}K, since it has no daughter nuclides,

the value in the table was used.

The final table for a sample's activity concentration was linked to Table 4.4. Examples are given in Table 4.5. For ^{238}U and ^{232}Th, the uncertainty in the activity concentration was reported as the uncertainty in the weighted mean. For ^{40}K, its uncertainty was propagated through the uncertainties in the mass, the net counts and the detector efficiency.

Sample SOS6T had the highest activity concentration for the ^{238}U series. The spectrum produced for SOS6T by the Palmtop MCA is shown in Figure 4.3. The spectrum for sample SOS7T is shown in Figure 4.4. SOS7T was the sample that had the highest activity concentration for the ^{232}Th series. Sample SOS37T had the highest activity concentration for ^{40}K. The spectrum produced for SOS37T is shown in Figure 4.5. SOS21T had one of the lowest activity concentrations for ^{238}U and ^{232}Th. Its spectrum is shown in Figure 4.6. The spectrum for the garden sample, taken from Kraaifontein, had very low levels of gamma radiation. The spectrum is shown in Figure 4.7.

Table 4.4: Examples of the tables created in the Excel spreadsheet for samples with high, medium and low activities. The Ac column gives the activity concentration.

(a) SOS7T

Series	Nuclide	Energy (keV)	Counts	Net counts	A_c (Bq/kg)
^{238}U	^{226}Ra	186	2526	880±130	75.6±11
	^{214}Pb	295	2026	1824±77	78.9±3.4
	^{214}Pb	352	3310	2973±94	68.5±2.2
^{232}Th	^{212}Pb	239	7171	6641±130	104±3.0
	^{228}Ac	338	1621	1496±74	117±6.4
	^{228}Ac	911	1698	1553±56	112±4.8
^{40}K	^{40}K	1461	3821	3430±76	912±22

(b) SOS18T

Series	Nuclide	Energy (keV)	Counts	Net counts	A_c (Bq/kg)
^{238}U	^{226}Ra	186	2206	560±117	47.7±10
	^{214}Pb	295	1263	1061±82	45.5±3.5
	^{214}Pb	352	2201	1864±109	42.9±2.5
^{232}Th	^{212}Pb	239	6498	5968±116	93.0±2.7
	^{228}Ac	338	1319	1194±71	92.8±5.9
	^{228}Ac	911	1574	1429±55	102±4.5
^{40}K	^{40}K	1461	730	339±47	89.3±12

(c) SOS21T

Series	Nuclide	Energy (keV)	Counts	Net counts	A_c (Bq/kg)
^{238}U	^{226}Ra	186	1890	244±91	24.2±9.0
	^{214}Pb	295	615	413±86	20.6±4.3
	^{214}Pb	352	1277	940±71	21.7±1.6
^{232}Th	^{212}Pb	239	1194	664±75	12.1±1.4
	^{228}Ac	338	285	160±43	14.5±3.9
	^{228}Ac	911	289	144±39	12.0±3.2
^{40}K	^{40}K	1461	2225	1830±58	563±18

Table 4.5: The final activity concentration table

Sample	Series	Ac
SOS7T	^{238}U	71.7±1.8
	^{232}Th	108±2.4
	^{40}K	912±22
SOS18T	^{238}U	44.0±2.0
	^{232}Th	95.0±2.2
	^{40}K	89.3±12
SOS21T	^{238}U	21.6±1.5
	^{232}Th	12.3±1.2
	^{40}K	563±18

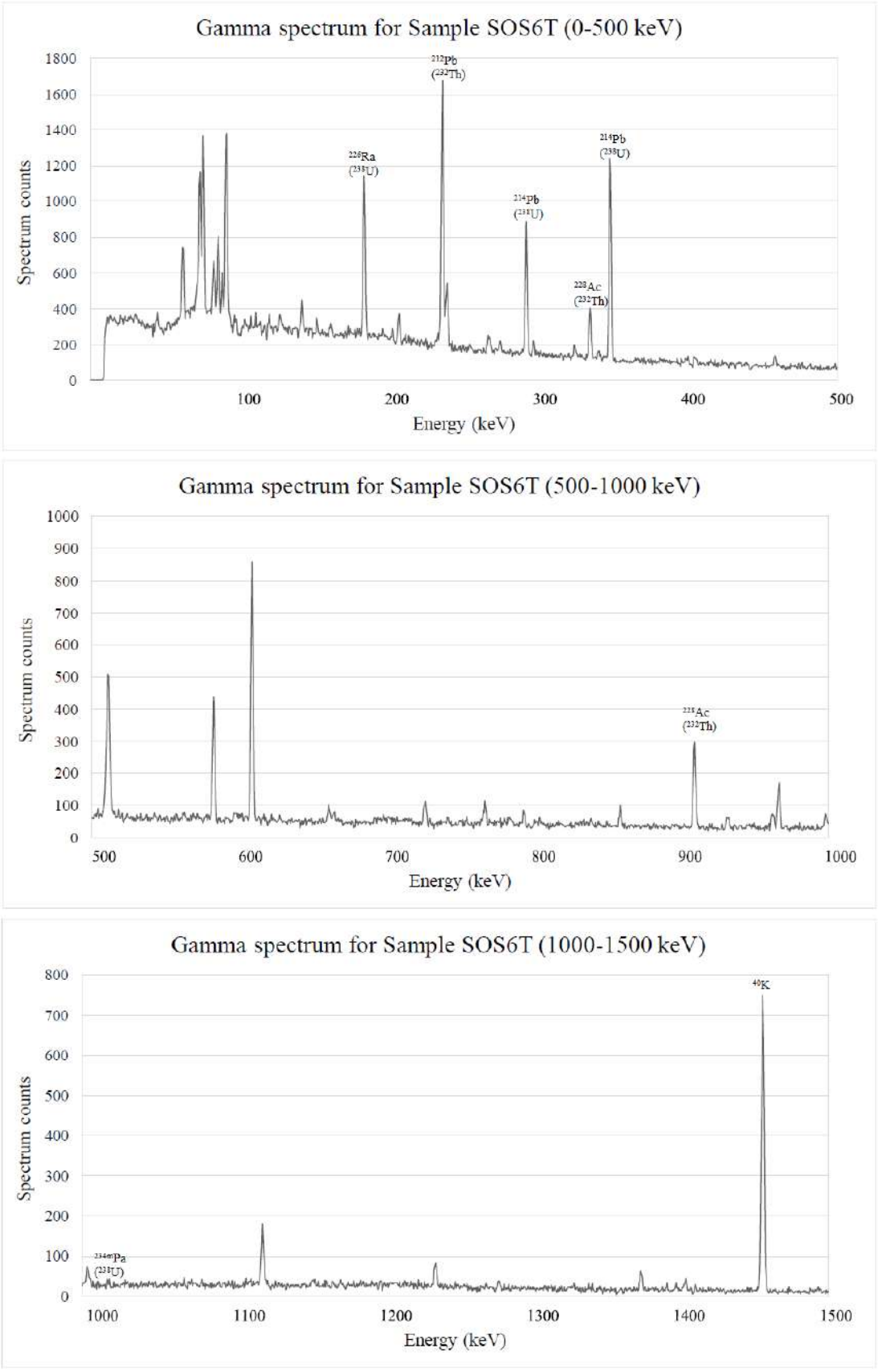

Figure 4.3: Palmtop MCA gamma spectrum for sample SOS6T

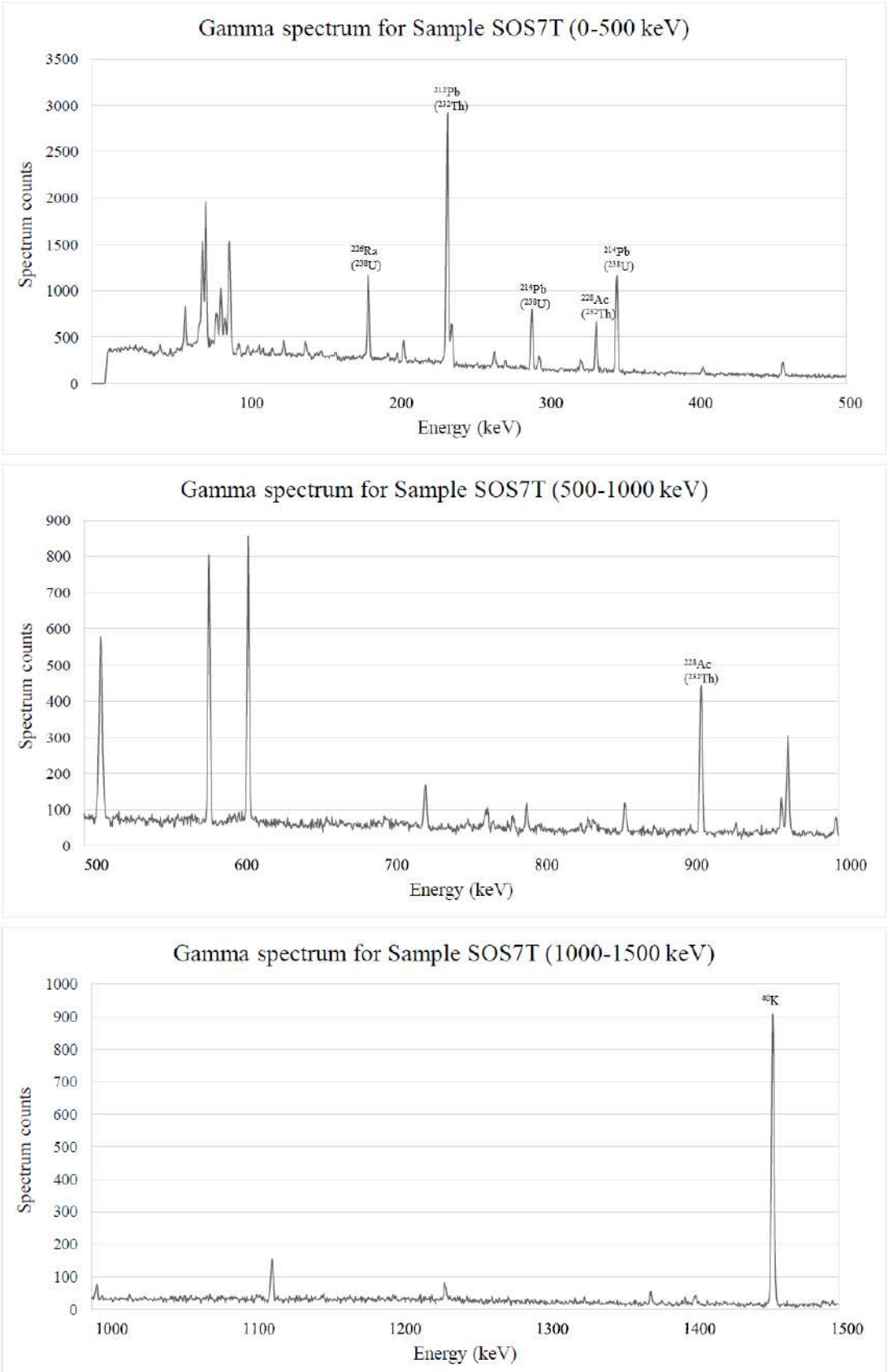

Figure 4.4: Palmtop MCA gamma spectrum for sample SOS7T

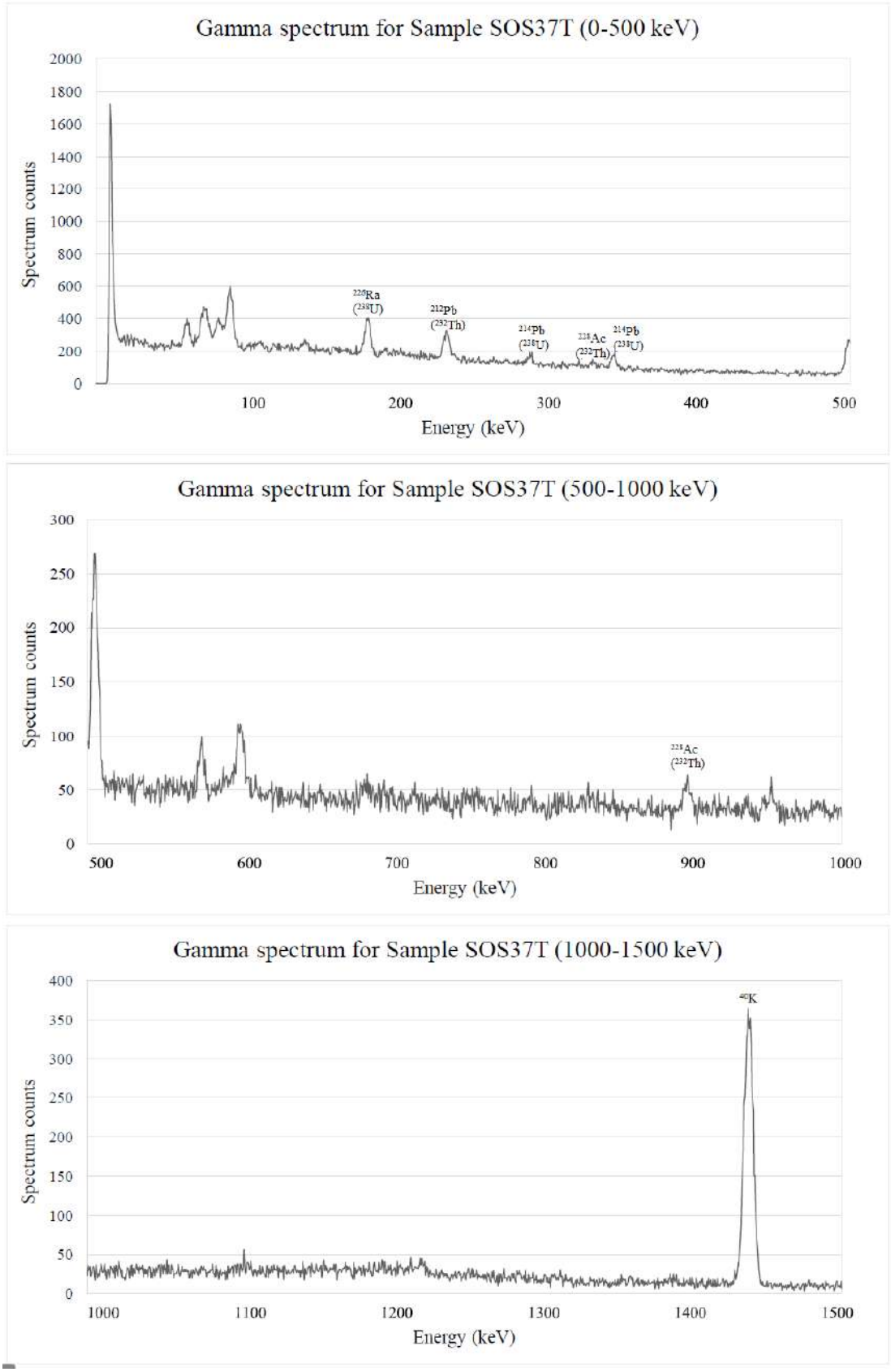

Figure 4.5: Palmtop MCA gamma spectrum for sample SOS37T

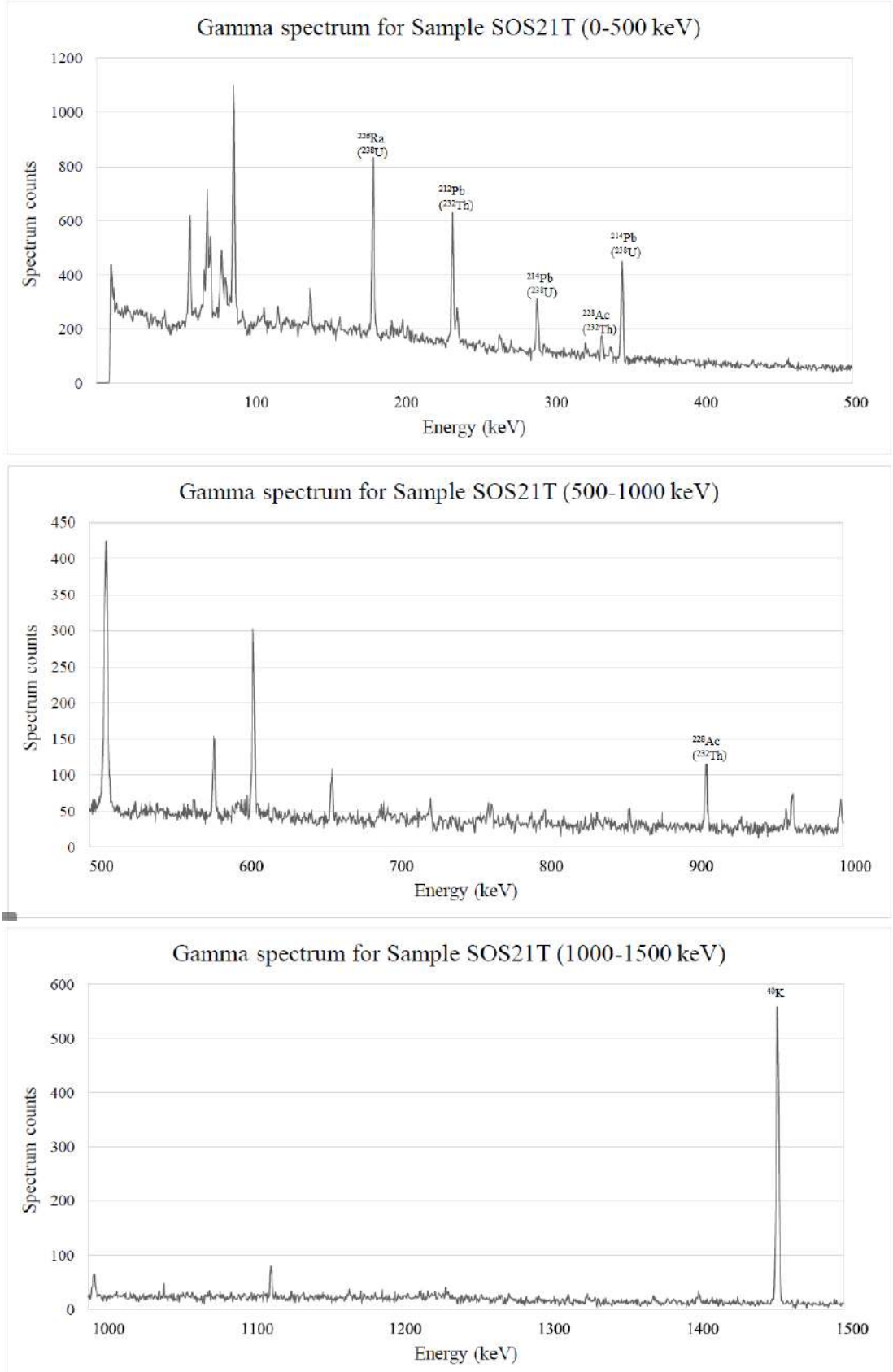

Figure 4.6: Palmtop MCA gamma spectrum for sample SOS21T

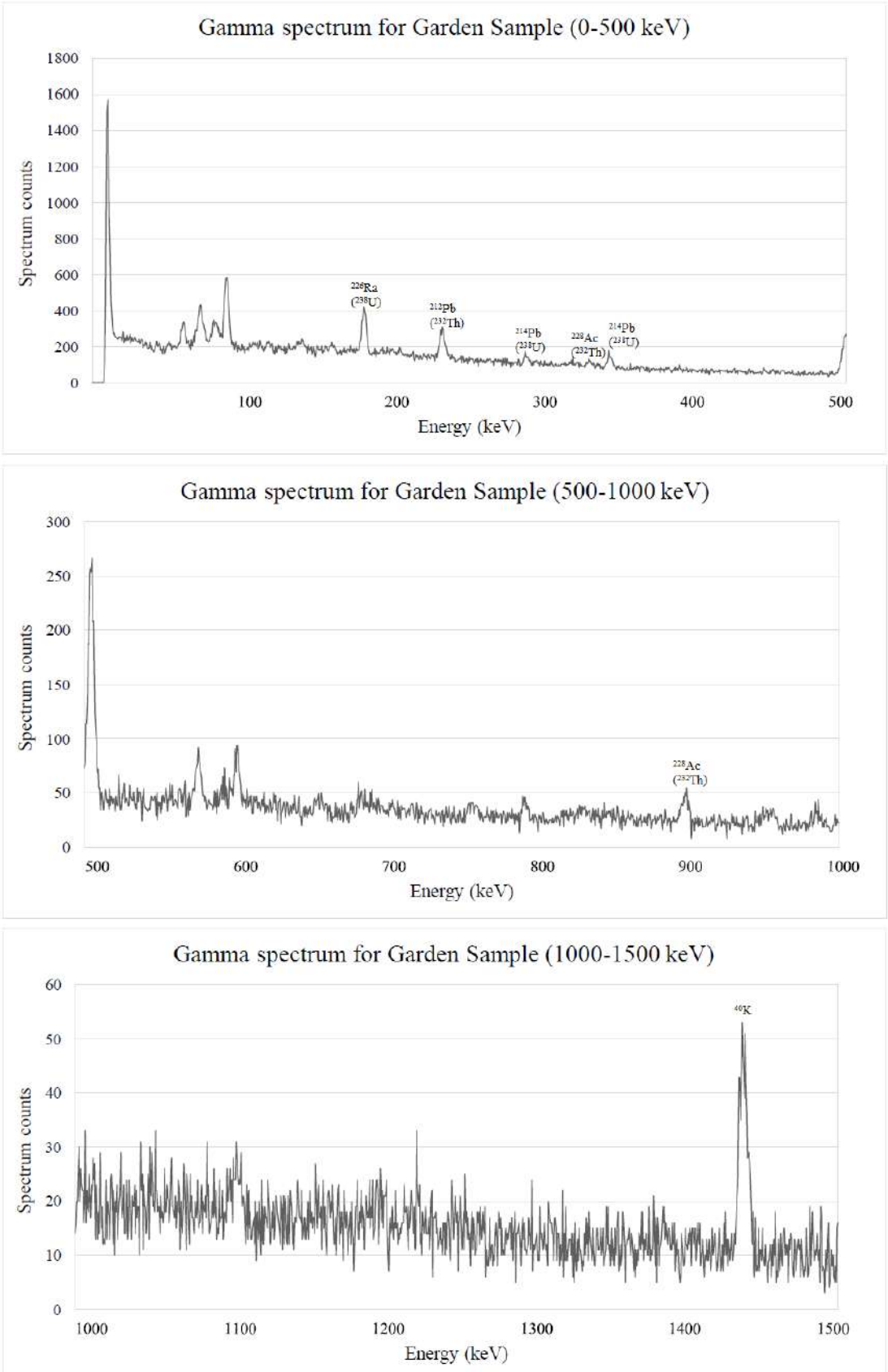

Figure 4.7: Palmtop MCA gamma spectrum for the garden sample

Chapter 5

Results

5.1 Activity Concentration

The results for the activity concentration are tabulated in Appendix D Table D.3.

The limit lines in Figure 5.4 and 5.5 indicate the global average activity concentration for each primordial radionuclide.

The low activity of the garden sample, in comparison to the activity concentrations of the soil samples from Ijero, emphasises the range of activities. There are a few low activity samples from Ijero that present activity concentrations of ^{238}U, ^{232}Th and ^{40}K that are comparable to those measured in the garden sample. There are also a few high activity samples that present activity concentrations nearly ten times greater than those measured in the garden sample.

Figures 5.6, 5.7 and 5.8 show the activity concentration heatmaps across the sample area for each primordial radionuclide. Each heatmap shows the sample location, colour coded according to the activity concentration of the soil obtained at that location. The maps were created using QGIS, a free GIS software, available for Windows and Ubuntu.

In total, 30 soil samples were measured. Of these samples, 13 had ^{238}U series concentrations above 33 Bq/kg, 3 of those samples had activity concentrations for the ^{238}U series above 70 Bq/kg. For the ^{232}Th series, 13 samples had activity

concentrations above 45 Bq/kg with 2 samples above 90 Bq/kg. Finally, 17 samples had ^{40}K activity concentrations above 420 Bq/kg with 11 of those above 800 Bq/kg.

The activity concentration of the ^{238}U series and ^{232}Th series is higher towards the east, where the geology largely consists of migmatite gneiss, granite and pegmatite. It can be deduced that the geology contributes substantially to the ^{238}U series and ^{232}Th series activity concentration in the soil.

The descriptive statistics are tabulated beneath each graph. The most significant of these statistics is the range of results, including the minima and maxima. The large spread of results is also seen in other studies, by Usikalu et al. and Olise et al., conducted in Ijero [Usi+19][OAO16]. A comparison of activity concentration results by Usikalu et al. and Olise et al. with those obtained in this study is shown in Appendix D, Table D.4. This data is illustrated in Figures 5.1 to 5.3.

The weighted mean is quoted to easily compare results with those obtained in other studies conducted in Nigeria. The weighted mean was calculated separately, according to Equation 4.19, and included in the descriptive statistics for the activity concentration.

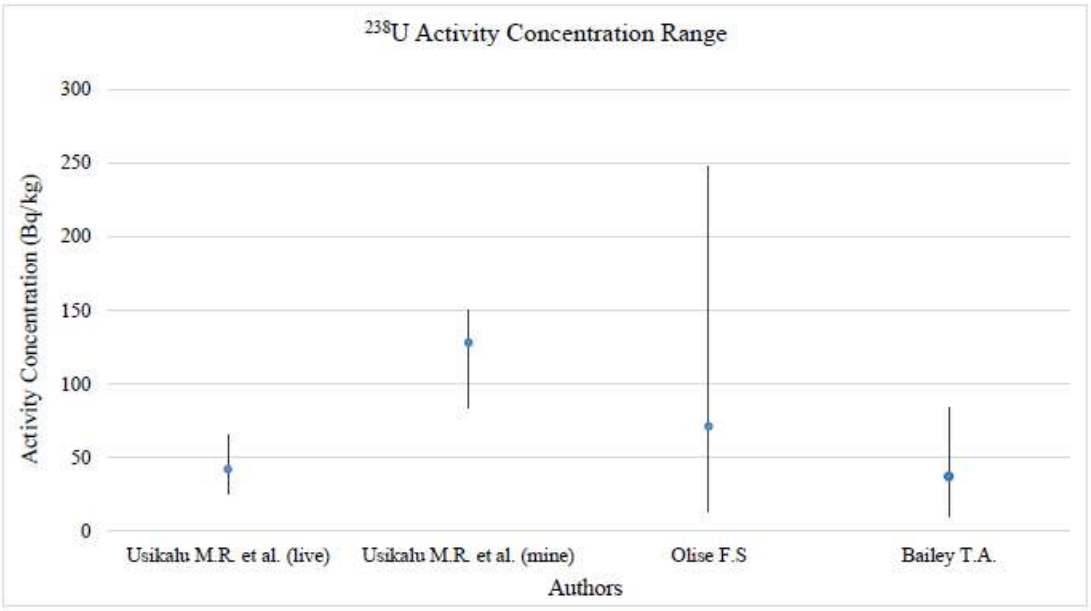

Figure 5.1: A comparison of the ranges of activity concentrations of ^{238}U previously found in Ijero by Usikalu et al. and Olise et al. with those found in the present study [Usi+19][OAO16]

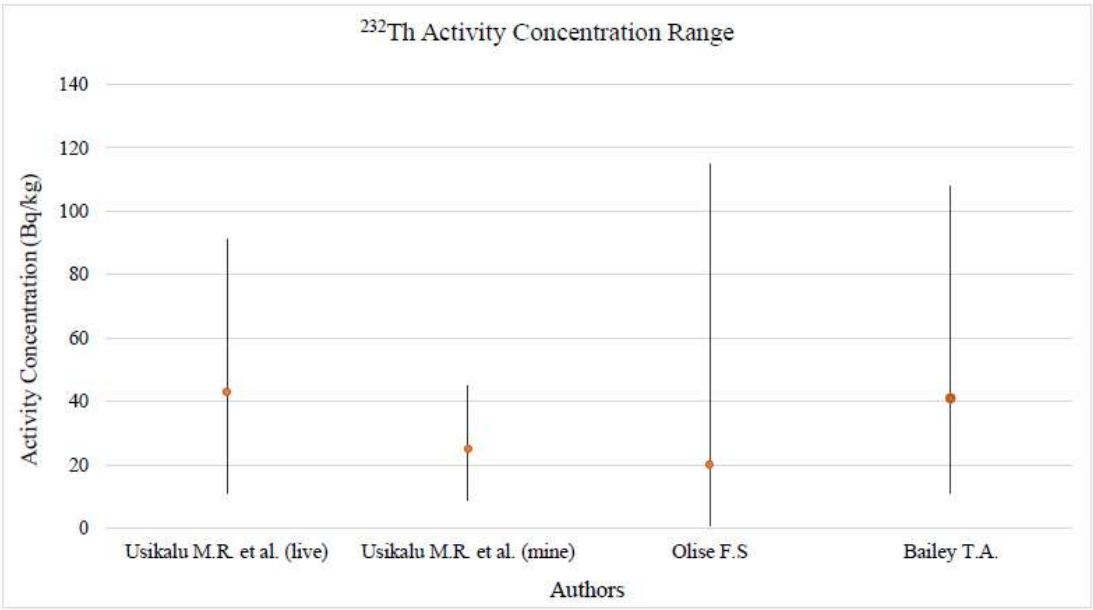

Figure 5.2: A comparison of the ranges of activity concentrations of ^{232}Th previously found in Ijero by Usikalu et al. and Olise et al. with those found in the present study [Usi+19][OAO16]

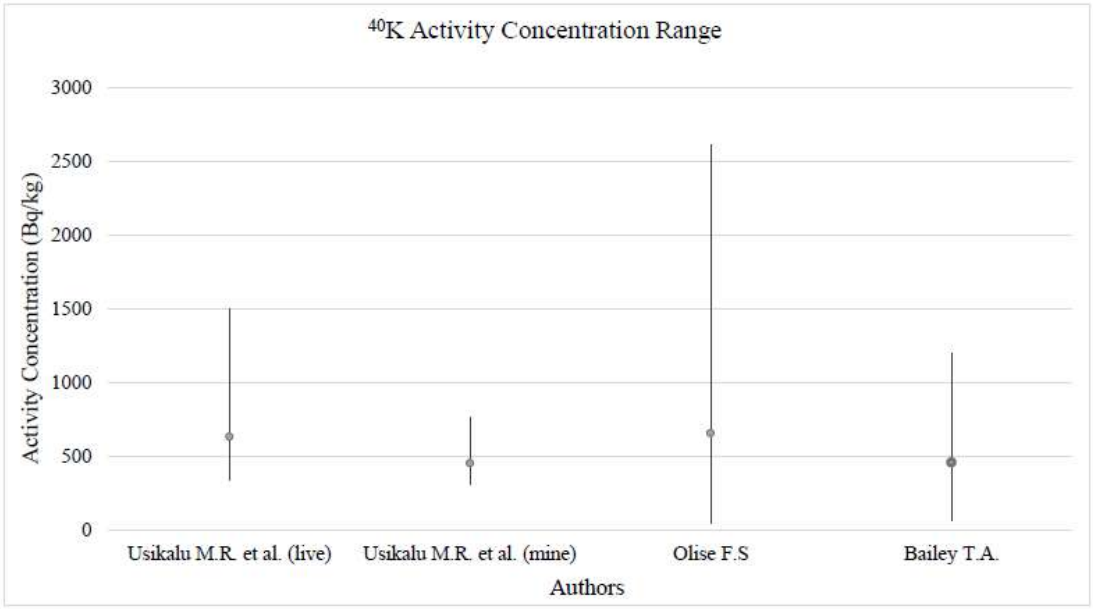

Figure 5.3: A comparison of the ranges of activity concentrations of ^{40}K previously found in Ijero by Usikalu et al. and Olise et al. with those found in the present study [Usi+19][OAO16]

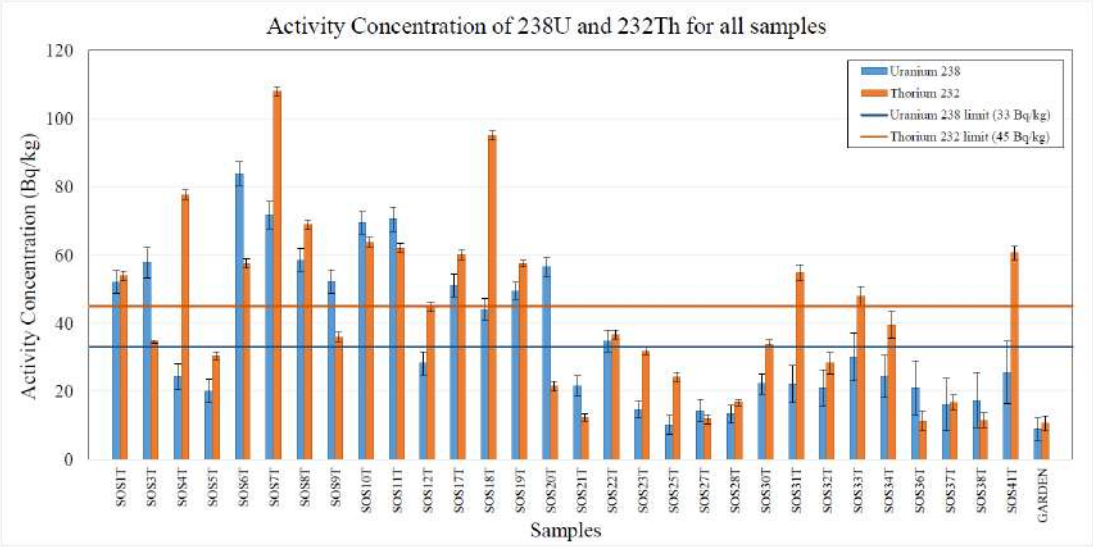

(a) **Descriptive statistics for the activity concentration of the ^{238}U series (Bq/kg)**

Weighted Mean	Median	Standard Deviation	Range	Minimum	Maximum
38.5	26.9	21.1	73.8	10.1	83.9

(b) **Descriptive statistics for the activity concentration of the ^{232}Th series (Bq/kg)**

Weighted Mean	Median	Standard Deviation	Range	Minimum	Maximum
37.1	38.1	24.7	96.7	11.3	108.0

Figure 5.4: The activity concentration of ^{238}U and ^{232}Th for all samples

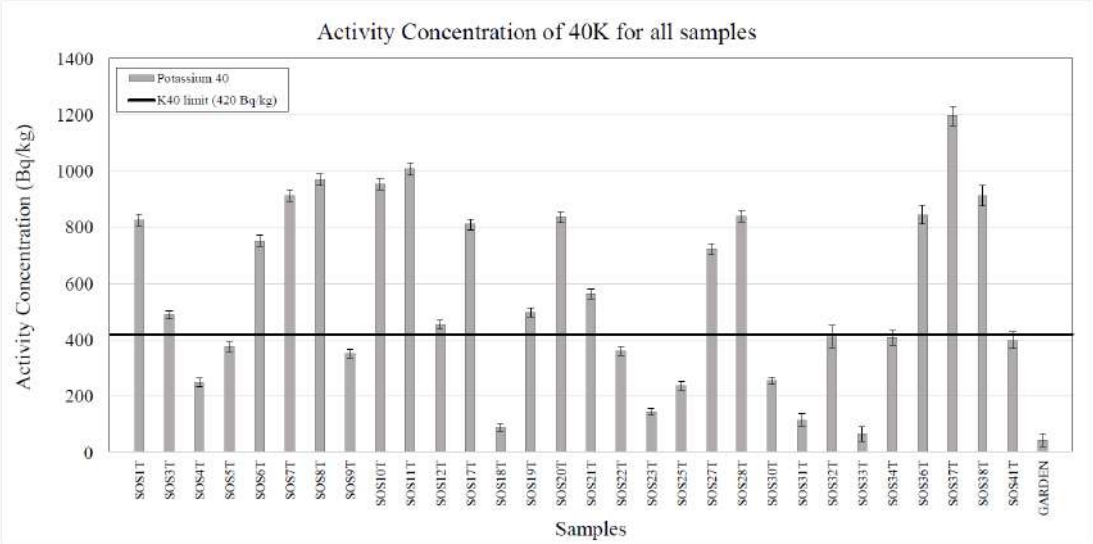

(a) **Descriptive statistics for the activity concentration of the ^{40}K series**

Weighted Mean	Median	Standard Deviation	Range	Minimum	Maximum
461	493	319	1129	67	1196

Figure 5.5: The activity concentration of ^{40}K for all samples

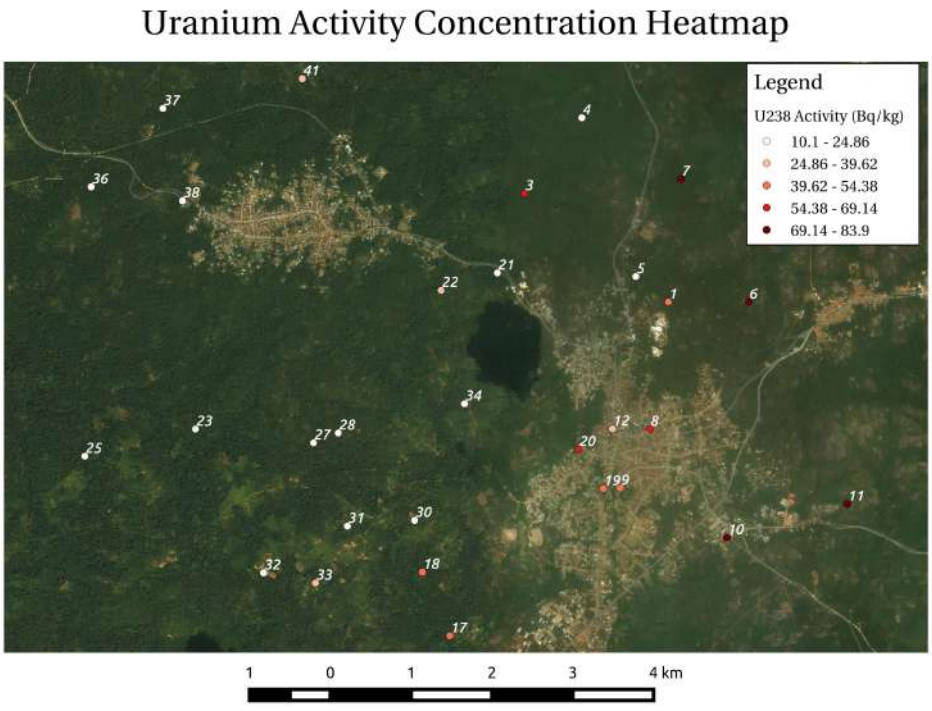

Figure 5.6: The activity concentration heatmap for ^{238}U for all samples

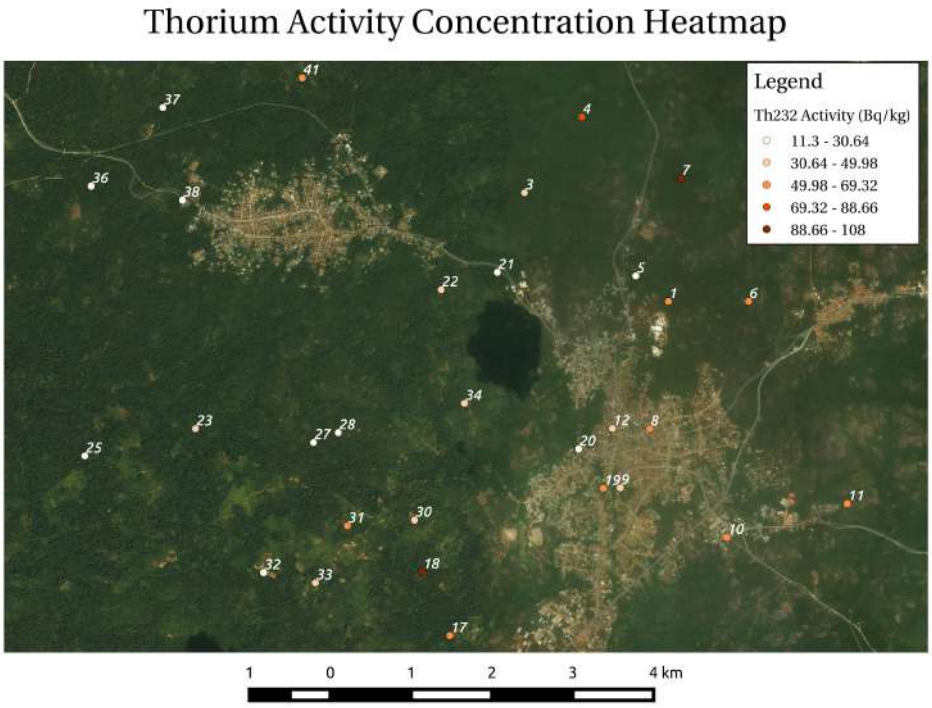

Figure 5.7: The activity concentration heatmap for ^{232}Th for all samples

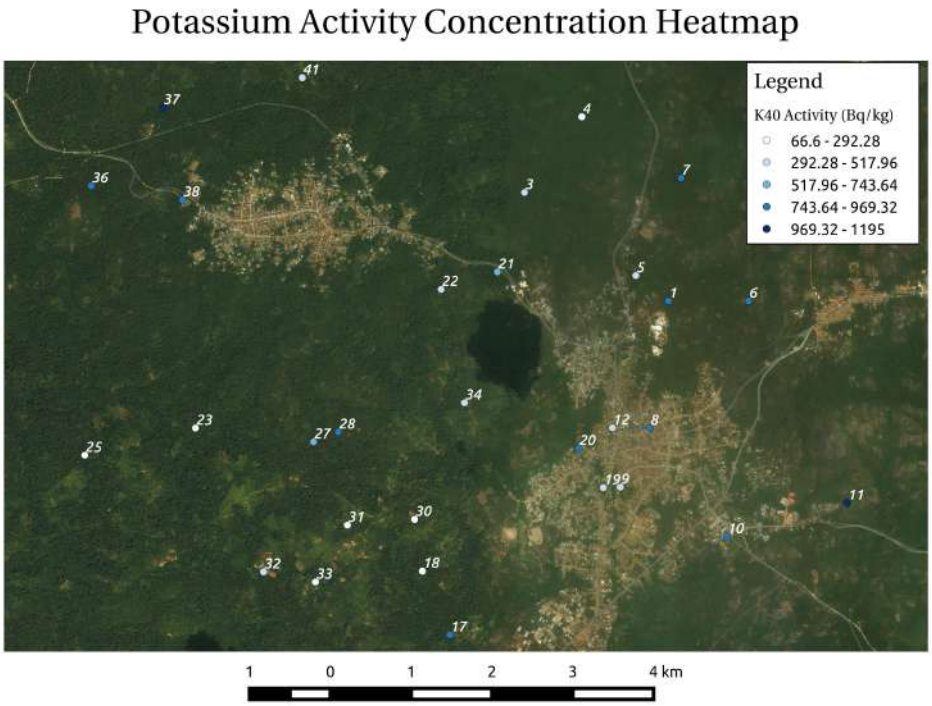

Figure 5.8: The activity concentration heatmap of ^{40}K for all samples

5.2 Radiological Risk Factors

The radiological risk factors could be more telling as to which sample locations are most concerning. The results for the radiological risk factors are tabulated in Appendix D, Tables D.3 to D.6. The results are plotted in Figures 5.9 to 5.15.

The limit lines in each plot correspond to those limits and standards outlined in Chapter 4.

Since the excess percentage risk for developing cancer depends on the excess lifetime cancer risk, it is possible to have a negative percentage risk result. The percentage risk depends on the estimated lifetime cancer risk, which depends on the annual effective dose rate, which finally depends on the absorbed dose rate in air. Since the percentage risk is in essence a propagation of all these radiological risk factors, Figure 5.16 shows the heatmap of the percentage risk across the sample area.

A map, showing the geology of the sample area obtained by Adesiyan, T.A. and subsequently edited for this study to include samples with elevated percentage risk, is shown in Figure 5.17. There seems to be a trend of high risk locations and migmatite gneiss geology. Migmatite gneiss and granite have been proven to have elevated concentrations of ^{238}U and ^{232}Th [Dża+18].

In total, thirty soil samples were evaluated. Of these samples, five had hazard indices outside of the permissible limit of 1 mSv/yr. Since the hazard indices are calculated using the activity concentration of ^{238}U, ^{232}Th and ^{40}K, there is also a large range of results for internal and external hazard indices. The internal hazard index, which quantifies the internal dose due to alpha particles, emitted during the decay of ^{222}Rn and ^{220}Rn, contributes the most to the total hazard index. The external hazard index, which quantifies the external dose due to gamma radiation from the building materials, is less than the internal hazard index as the formulae place more weight on the dose incurred due to inhalation and ingestion of alpha particles. Eight samples were above the permissible limit for the Annual Effective Dose rate, where indoor and outdoor dose rates must

sum to 1 mSv/yr. The Annual Gonadal Equivalent Dose limit of 300 μSv/yr was surpassed by twenty-five samples. For the Excess Lifetime Cancer Risk and percentage risk, seven samples were outside of the maximum permissible ELCR limit of 0.29×10^{-3}, with the highest excess percentage risk at 67%.

The calculated descriptive statistics are tabulated beneath each figure. The mean value in the radiological risk descriptive statistics tables does not reflect the weighted mean.

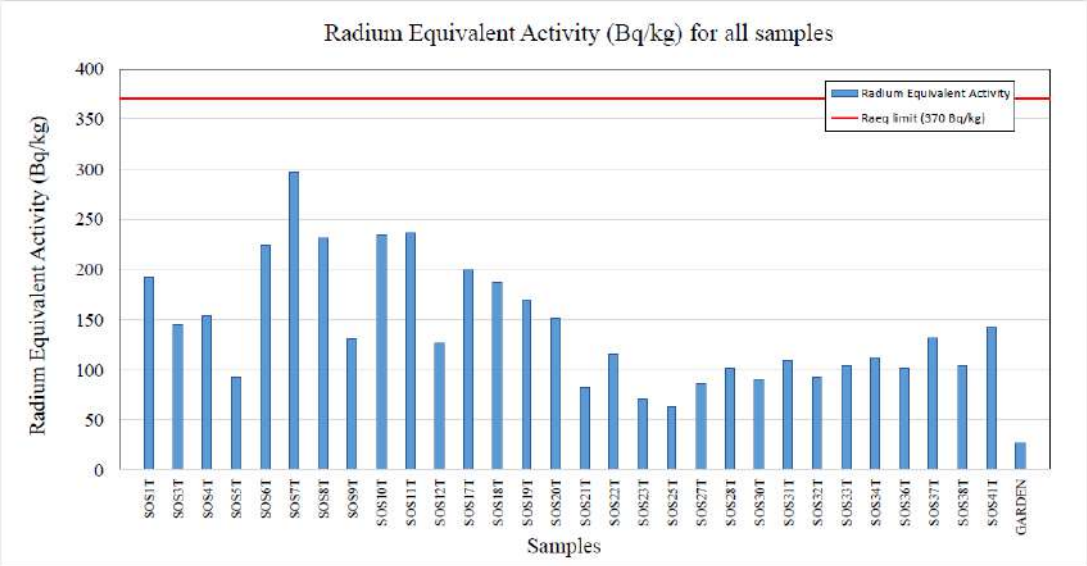

(a) **Descriptive statistics for the radium equivalent activity**

Mean	Median	Standard Deviation	Range	Minimum	Maximum
143	129	59	233	63	296

Figure 5.9: The radium equivalent activity for all samples

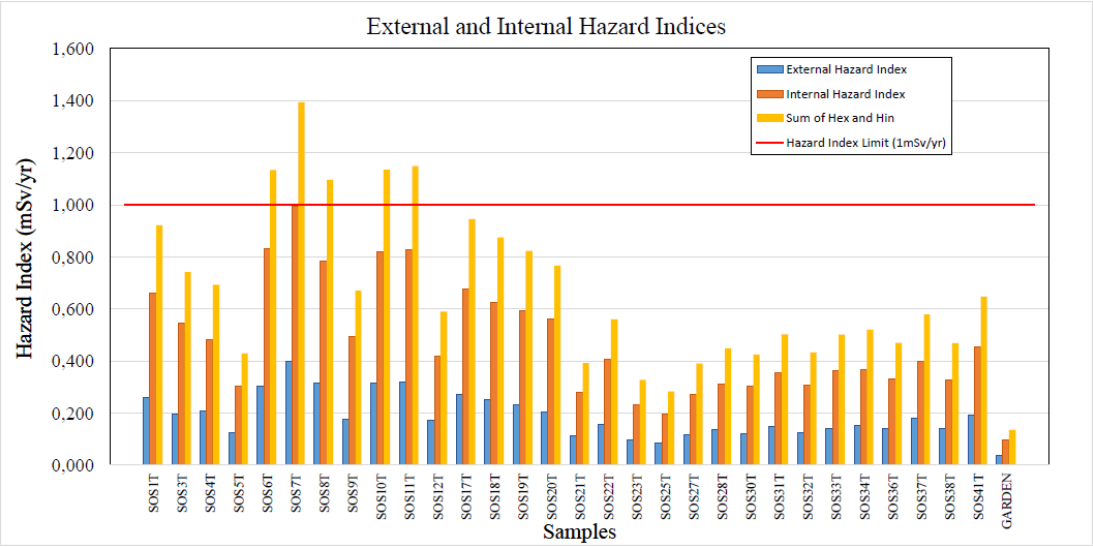

(a) **Descriptive statistics for the internal hazard index (mSv/yr)**

Mean	Median	Standard Deviation	Range	Minimum	Maximum
0.484	0.411	0.210	0.797	0.197	0.994

(b) **Descriptive statistics for the external hazard index (mSv/yr)**

Mean	Median	Standard Deviation	Range	Minimum	Maximum
0.193	0.174	0.079	0.315	0.085	0.400

Figure 5.10: The internal and external hazard indices for all samples

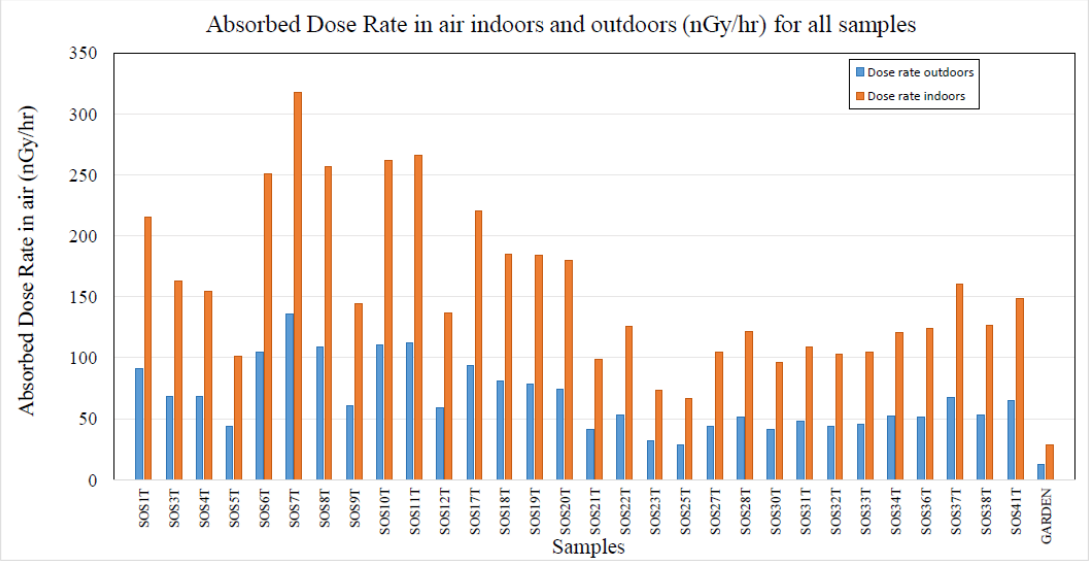

(a) **Descriptive statistics for the absorbed dose rate indoors (nGy/hr)**

Mean	Median	Standard Deviation	Range	Minimum	Maximum
157	141	64	250	67	317

(b) **Descriptive statistics for the absorbed dose rate outdoors (nGy/hr)**

Mean	Median	Standard Deviation	Range	Minimum	Maximum
67	60	27	107	29	136

Figure 5.11: Descriptive statistics for the absorbed dose rate indoors

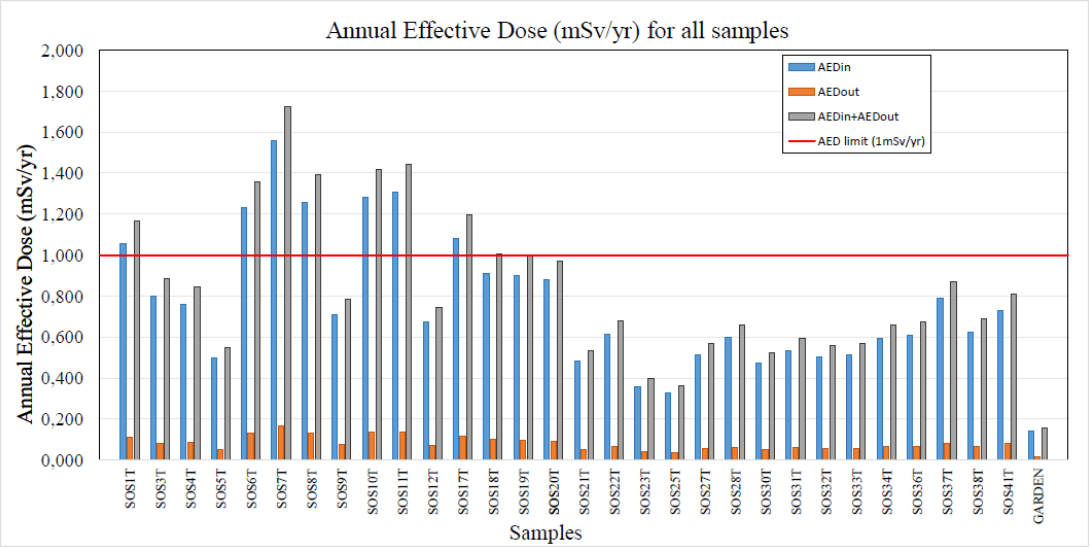

(a) **Descriptive statistics for the annual effective dose indoors (mSv/yr)**

Mean	Median	Standard Deviation	Range	Minimum	Maximum
0.772	0.691	0.314	1.230	0.328	1.558

(b) **Descriptive statistics for the annual effective dose outdoors (mSv/yr)**

Mean	Median	Standard Deviation	Range	Minimum	Maximum
0.082	0.073	0.033	0.131	0.036	0.167

Figure 5.12: The annual effective dose rate for all samples

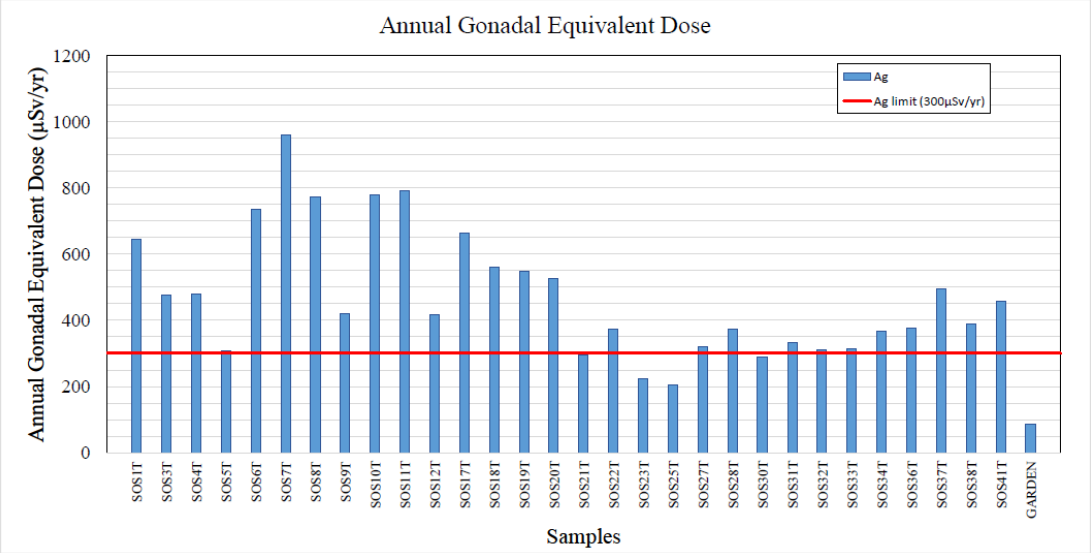

(a) **Descriptive statistics for the annual gonadal equivalent dose (μSv/yr)**

Mean	Median	Standard Deviation	Range	Minimum	Maximum
474	418	190	753	206	959

Figure 5.13: The annual gonadal equivalent dose for all samples

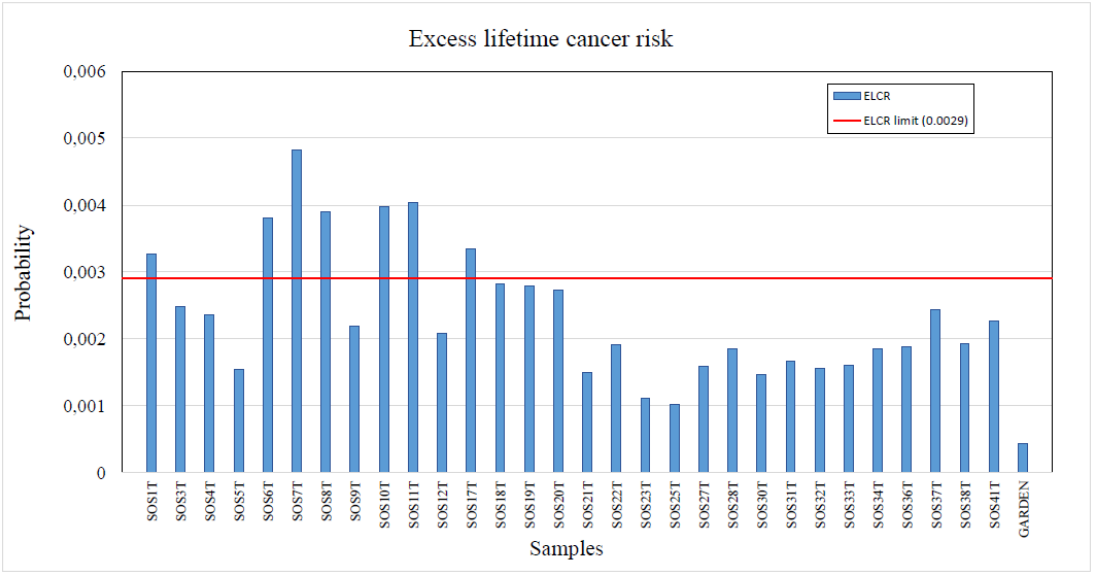

(a) **Descriptive statistics for the excess lifetime cancer risk**

Mean	Median	Standard Deviation	Range	Minimum	Maximum
0.0024	0.0021	0.0010	0.0038	0.0010	0.0048

Figure 5.14: The excess lifetime cancer risk for all samples

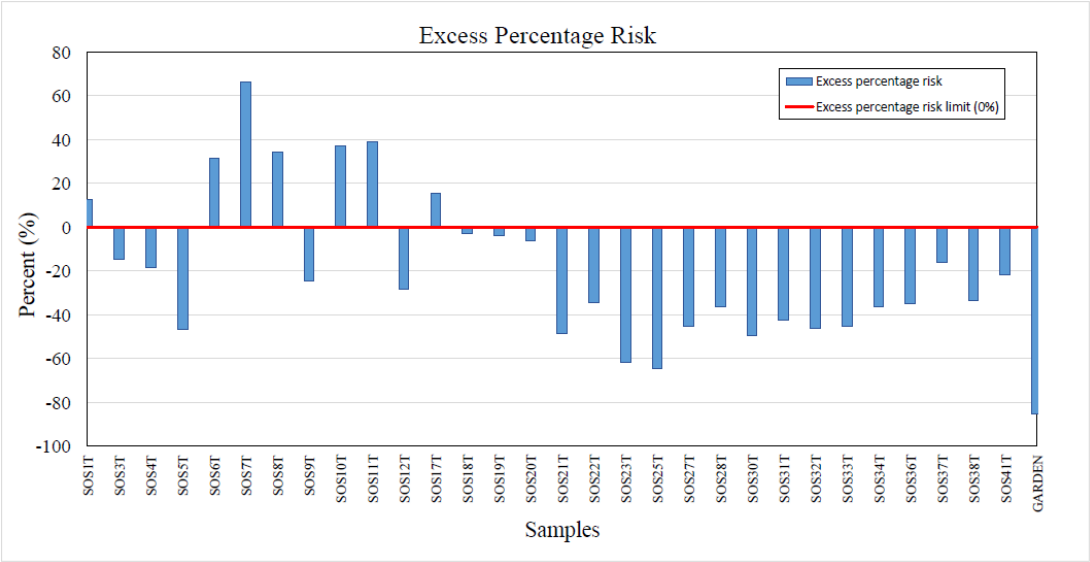

(a) **Descriptive statistics for the excess percentage risk for cancer induction**

Mean	Median	Standard Deviation	Range	Minimum	Maximum
-18	-26	34	131	-65	67

Figure 5.15: The excess percentage risk for cancer induction for all samples

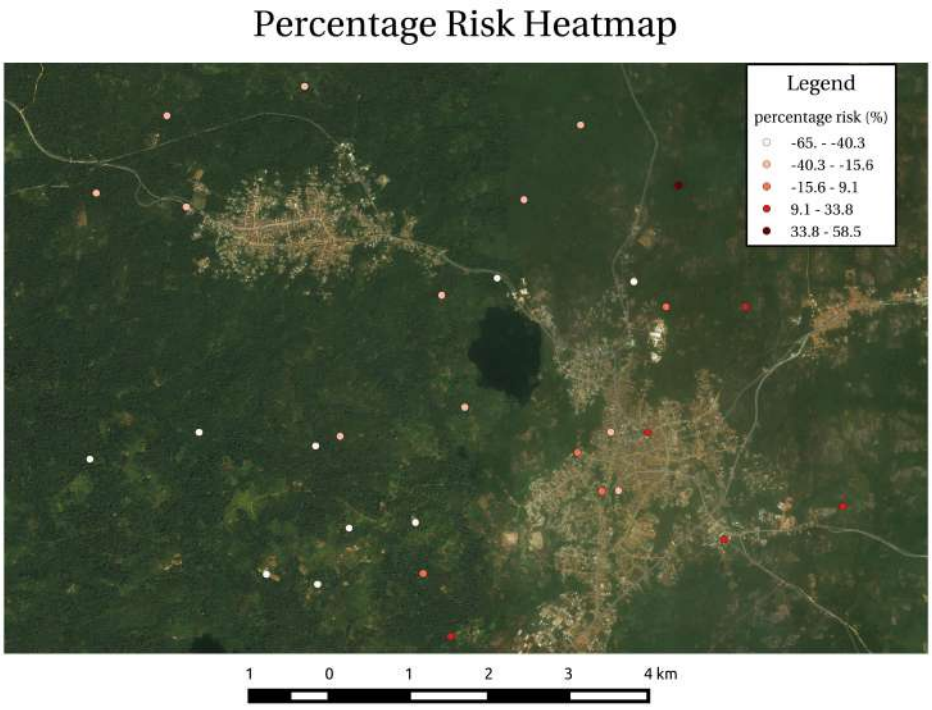

Figure 5.16: The excess percentage risk heatmap for the sample area

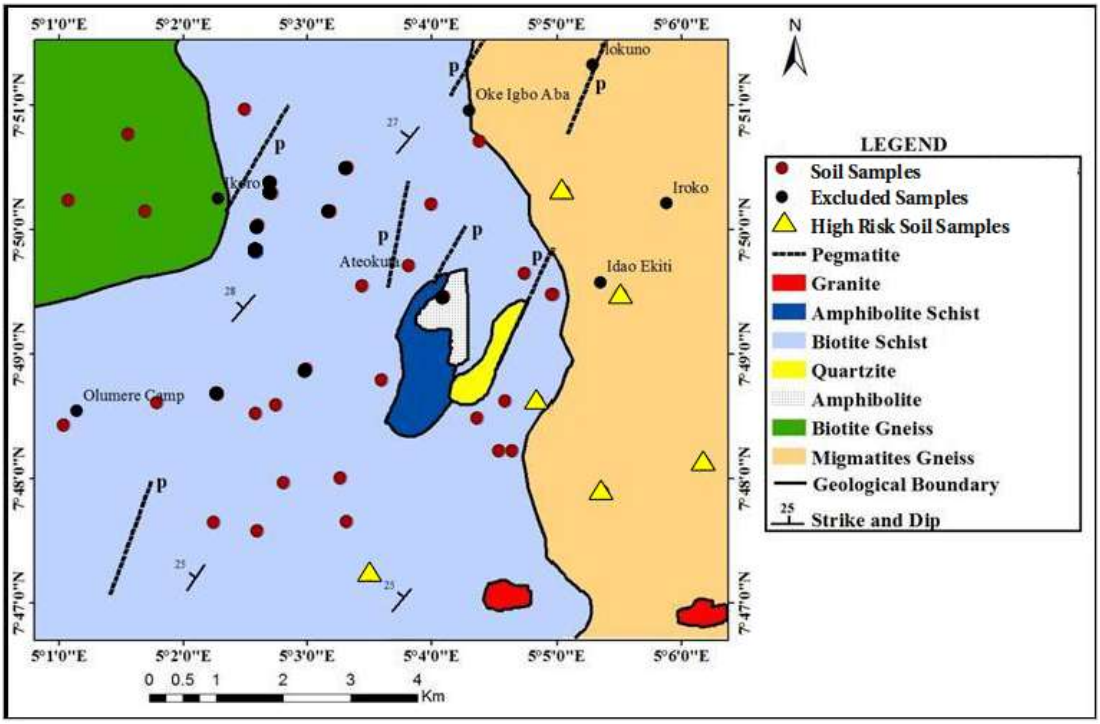

Figure 5.17: The geology of the sample area with samples (red), excluded samples (black) and samples with high percentage risk (yellow triangle) [Ade18b]

5.3 Global Averages

To contextualize the results obtained, they must be compared to results obtained in other parts of the world [UNS00] as shown in Table 5.1 and Figure 5.18.

Table 5.1: Average outdoor dose rates around the world [UNS00]

Location	D_{out} (nGy/hr) inferred from radionuclide concentrations in soil
Luxembourg	72
Ireland	58
Sweden	77
India	69
China	58
Norway	86
United States	55
Malaysia	93
Portugal	86
Syrian Arab Republic	33
Poland	42
Japan	45
Denmark	39
Spain	54
Ijero (this study)	65
Ijero [Usi+19]	90
Population weighted average (1996)	59

The average outdoor dose rate for Ijero, obtained in this study, is only slightly higher than the global average, given by UNSCEAR 2000 [UNS00]. Therefore, on average Ijero's primordial radionuclide activity concentration is not unreasonably high considering the circumstances.

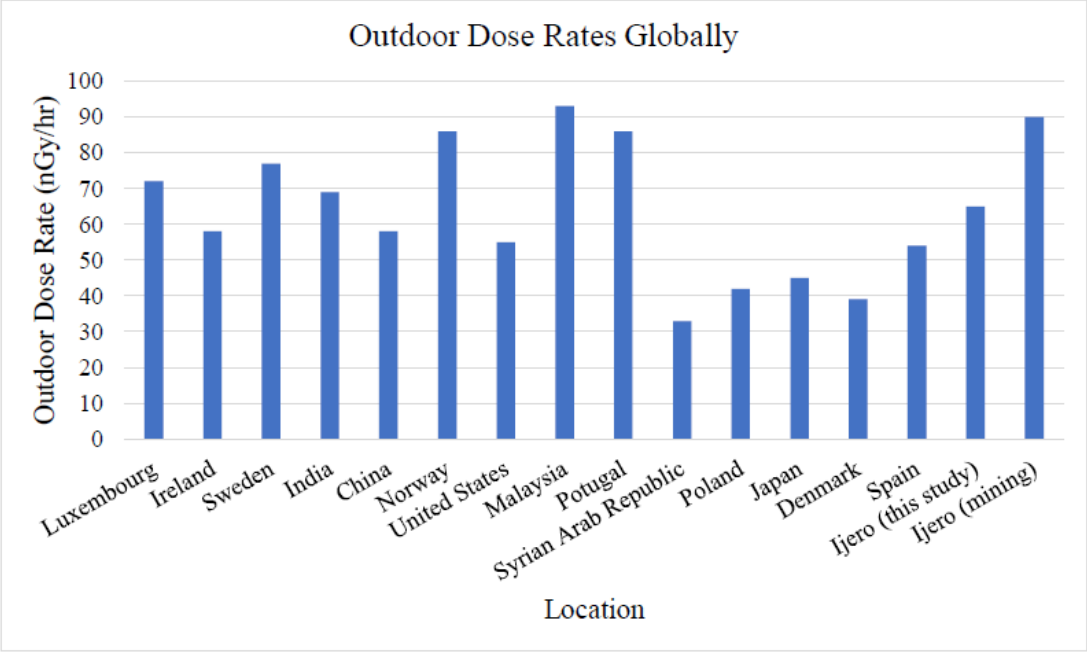

Figure 5.18: Average outdoor dose rates around the world [UNS00]

5.4 Previous Results in Ijero

As mentioned in Chapter 1.3, there have been several studies presenting radiological results on soil [OAO16], water [AIK18][Aki+18], sediment and mine tailings [Isi14] in Ijero.

The inconsistency in the results obtained in different studies is possibly due to the sampling locations. Samples taken in areas near mining, such as those taken by Usikalu et al. and Olise et al., presented high activity concentrations of ^{238}U and ^{232}Th [Usi+19][OAO16]. In the present study, samples taken towards the east, above migmatite gneiss had much higher activity concentrations than those taken in the west.

The dose rate results, obtained by Usikalu et al., were within experimental uncertainty of 10%, to the mean absorbed dose rate in the current study of 67 nGy/hr. It was speculated that the high concentrations of ^{40}K may be due to the use of inorganic fertilisers in the living areas [Usi+19]. In the current study, there was a soil sample, SOS37T, with very high ^{40}K activity concentration but low ^{238}U series and ^{232}Th series activity concentration. When viewed on the map, it seems to be in a very green area, largely undisturbed by mining activities. This too

could be attributed to inorganic fertilisers. A trend is observed, by Usikalu et al., with the activity concentration of the ^{238}U series and ^{40}K, exceeding 33 Bq/kg and 420 Bq/kg respectively. While the ^{232}Th series presents a weighted mean that is below 45 Bq/kg.

Olise et al. concluded that proper monitoring and control of construction materials is required to protect miners and the public [OAO16] as the mean concentration for the ^{238}U series and ^{40}K was much higher than the global population-weighted average for concentration in soils, given by UNSCEAR 2000, of 33 Bq/kg and 420 Bq/kg respectively. The mean activity concentration for ^{232}Th series was less than the global population-weighted average for concentration in soils of 45 Bq/kg, given by UNSCEAR. Once again, as in the current study, the weighted mean followed the same trend. The activity concentration of the ^{238}U series and ^{40}K was higher than 33 Bq/kg and 420 Bq/kg respectively. The ^{232}Th series presented a weighted mean that was below 45 Bq/kg.

A study, by Isinkaye, O., on the radiological hazards due to mine tailings and sediment presented soil activity concentrations for the ^{226}Ra series,^{232}Th series and ^{40}K. The study concluded that while the hazard indices are higher than global averages, they are acceptable [Isi14].

In the current study, There are certain locations where the activity concentration of primordial radionuclides is high, far surpassing the world average. However, most of the soil samples measured did not exceed the recommended maxima for activity concentrations and radiological risk factors.

If the people of Ijero are experiencing increased cases of lung cancer due to their environment, then it could be due to additive effects from another factor, such as chemical toxicity.

Chapter 6

Conclusion

Due to informal and ongoing mining activities, the natural radioactivity in soil samples from Ijero, Nigeria was measured and the radiological risks were assessed. The radionuclides under consideration were the ^{238}U series, ^{232}Th series and ^{40}K. The soil samples were crushed, sieved, dried and sealed in identical cylindrical containers. At iThemba LABS, the HPGe detector was coupled to the Palmtop MCA for high resolution gamma spectroscopy. The activity concentration of the aforementioned radionuclides was measured and the radiological risk factors were calculated to assess the risk, on average, to an individual living in Ijero.

The measured activity concentration for the ^{238}U series ranged from 10.1±1.4 to 83.9±2.1 Bq/kg with a mean value of 38.5 Bq/kg. For ^{232}Th the activity concentration ranged from 11.3±2.9 to 108.0±2.4 Bq/kg with a mean value of 37.1 Bq/kg. Finally, ^{40}K ranged from 67±26 to 1196±36 Bq/kg with a mean value of 461 Bq/kg. Thus, the mean values for the activity concentration of primordial radionuclides ^{238}U and ^{40}K were only marginally higher than the global averages of 33 Bq/kg and 420 Bq/kg respectively. The activity concentration of ^{232}Th was slightly less than the global average of 45 Bq/kg.

In total, thirty soil samples were evaluated. None of the samples had a radium equivalent activity greater than the limit of 370 Bq/kg. Of these samples, five had hazard indices outside of the permissible limit of 1 mSv/yr. Eight samples were above the permissible limit for the Annual Effective Dose rate, where indoor and outdoor dose rates must sum to 1 mSv/yr. The Annual Gonadal Equivalent Dose limit of 300 μSv/yr was surpassed by twenty-five samples.

For the Excess Lifetime Cancer Risk (ELCR) and excess percentage risk, which

estimates the probability that an individual could develop cancer in their lifetime, seven samples exceeded the maximum ELCR of 0.29×10^{-3}. The ELCR results ranged from 0.102×10^{-3} to 0.483×10^{-3}. The highest ELCR result is 1.67 times greater than the upper recommended value of 0.29×10^{-3}. A value of 1.67 for the ratio of the calculated ELCR to the maximum permissible ELCR corresponds to an excess percentage risk of 67%. The mean ELCR is 0.239×10^{-3} which is below the maximum recommended value.

There are certain locations where the activity concentration of primordial radionuclides is high, far surpassing the world average. However, most of the soil samples measured did not exceed the recommended maxima for activity concentrations and radiological risk factors. If there is an increase in lung cancer, it could be due to additive effects from chemical toxicity.

Appendix A

Table of Isotopes

Symbol	Name
^{228}Ac	actinium-228
^{40}Ar	argon-40
^{14}C	carbon-14
^{40}Ca	calcium-40
^{40}K	potassium-40
^{234}Pa	protactinium-234
^{206}Pb	lead-206
^{208}Pb	lead-208
^{210}Pb	lead-210
^{212}Pb	lead-212
^{214}Pb	lead-214
^{226}Ra	radium-226
^{220}Rn	radon-220 (thoron)
^{222}Rn	radon-222 (radon)
^{228}Th	thorium-228
^{232}Th	thorium-232
^{234}Th	thorium-234
^{234}U	uranium-234
^{235}U	uranium-235
^{238}U	uranium-238

Appendix B

Gamma Emission Probability Calculations

^{238}U, ^{235}U and ^{234}U exist in natural samples [Eba10]. For an accurate determination of the activity concentration of ^{238}U, the counts in the 186 keV full-energy peak should be examined more carefully. This can be done by peak deconvolution or a calculation.

In order to perform the calculation, the natural abundance of ^{238}U must be considered, as well as the gamma emission probabilities and the specific activities of ^{226}Ra, ^{238}U and ^{235}U.

^{226}Ra is one of the radioactive daughters of ^{238}U. It decays and emits a gamma ray at energy 186.211 keV. ^{235}U also undergoes radioactive decay and emits a gamma ray with energy 185.712 keV [IAE]. Table B.1 contains the relevant gamma emission information for these radionuclides.

	^{226}Ra	^{235}U
E_γ	186.211	185.712
B_r	0.0364	0.57

Table B.1: The gamma energy and gamma emission probability for ^{226}Ra and ^{235}U

The total counts in the full-energy peak consist of counts from ^{226}Ra and ^{235}U [EEA05]. The total count rate, CR_{tot}, at approximately 186 keV is equal to the sum of the count rates of ^{226}Ra and ^{235}U.

$$\mathrm{CR_{tot}} = \mathrm{CR_{Ra}} + \mathrm{CR_{U^5}} \tag{B.1}$$

$$\begin{aligned} \frac{\mathrm{CR_{Ra}}}{\mathrm{CR_{U^5}}} &= \frac{\mathrm{A_{Ra}} \cdot \mathrm{B_r} \cdot \epsilon}{\mathrm{A_{U^5}} \cdot \mathrm{B_r} \cdot \epsilon} \\ &= \frac{\mathrm{A_{Ra}} \cdot 0.0364}{\mathrm{A_{U^5}} \cdot 0.57} \end{aligned} \tag{B.2}$$

The specific activity, for gamma radiation, per unit mass for ^{238}U and ^{235}U for natural uranium [WIS]:

$\mathrm{SA_{U^5}}$: 5,7$\times 10^5$Bq/kg
$\mathrm{SA_{U^8}}$: 123.2$\times 10^5$Bq/kg

At secular equilibrium, The activity of ^{238}U will equal that of ^{226}Ra [EEA05].

$$\begin{aligned} \frac{\mathrm{SA_{U^5}}}{\mathrm{SA_{U^8}}} &= \frac{\mathrm{SA_{U^5}}}{\mathrm{SA_{Ra}}} \\ &= \frac{5.698 \times 10^5}{1.232 \times 10^7} \\ &= 0.04625 \end{aligned} \tag{B.3}$$

This is the ratio of the activity of ^{235}U and ^{226}Ra [EEA05]. Then from equation B.2

$$\begin{aligned} \frac{\mathrm{CR_{Ra}}}{\mathrm{CR_{U^5}}} &= \frac{\mathrm{A_{Ra}} \cdot 0.0364}{\mathrm{A_{U^5}} \cdot 0.57} \\ &= \frac{0.0364}{0.0462 \cdot 0.57} \\ &= 1.381 \end{aligned} \tag{B.4}$$

Therefore their contribution to the total count rate is

$$\frac{\mathrm{CR_{Ra}}}{\mathrm{CR_{tot}}} = \frac{1.381}{2.381} = 0.580 \tag{B.5}$$

$$\frac{\mathrm{CR_{U^5}}}{\mathrm{CR_{tot}}} = \frac{1}{2.381} = 0.420 \tag{B.6}$$

Natural abundance [Eba10]:
^{235}U: 0.72%
^{238}U: 99.27%

Without deconvoluting the peak, the total counts can now be written in terms of the counts due to ^{226}Ra.

$$\mathrm{CR_{tot}} = \frac{\mathrm{CR_{Ra}}}{0.580} \tag{B.7}$$

$$\mathrm{CR_{tot}} \cdot 0.580 = \mathrm{CR_{Ra}} \tag{B.8}$$

Now consider the activity concentration formula from Equation 4.2:

$$\mathrm{A} = \frac{\mathrm{N_i}}{\mathrm{L_T} \cdot \epsilon \cdot \mathrm{m} \cdot \mathrm{B_r}} \tag{B.9}$$

set $T = \frac{1}{\mathrm{L_T} \cdot \epsilon \cdot \mathrm{m}}$ and consider $\mathrm{CR_{tot}}$ as the total net counts in the peak

$$\begin{aligned} \mathrm{A_{tot}} &= \frac{\mathrm{CR_{tot}}}{T \cdot \mathrm{B_r}} \\ \mathrm{A_{Ra}} &= \frac{\mathrm{CR_{tot}} \cdot 0.580 \cdot 0.9927}{T \cdot 0.0364} \\ &= \frac{1}{T} \cdot \frac{\mathrm{CR_{tot}}}{0.0632} \end{aligned} \tag{B.10}$$

The spectra's net Area will be used as $\mathrm{N_i}$. The effective branching ratio is 0,0632.

Appendix C

Background Measurements

Below are the spectra for the different background measurements.

Figure C.1 shows the spectrum for the background that was recorded with an empty closed lead castle, superimposed on the spectrum that was recorded for a closed lead castle with an empty pillbox on the detector. The background measured with the pillbox is only slightly higher than the one measured without one.

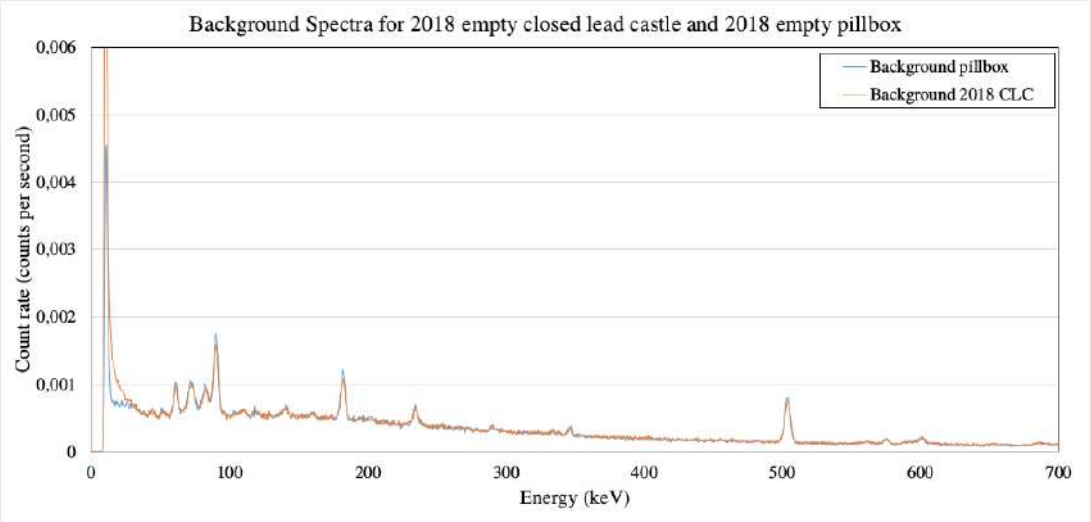

Figure C.1: Superimposed background spectra for 2018

Figure C.2 shows the spectrum for the background that was recorded for a closed lead castle with an empty pillbox on the detector superimposed on the spectrum that was recorded for a closed lead castle and a pillbox filled with still mineral water on the detector. Here, the background with the pillbox filled with mineral water was noticeably higher.

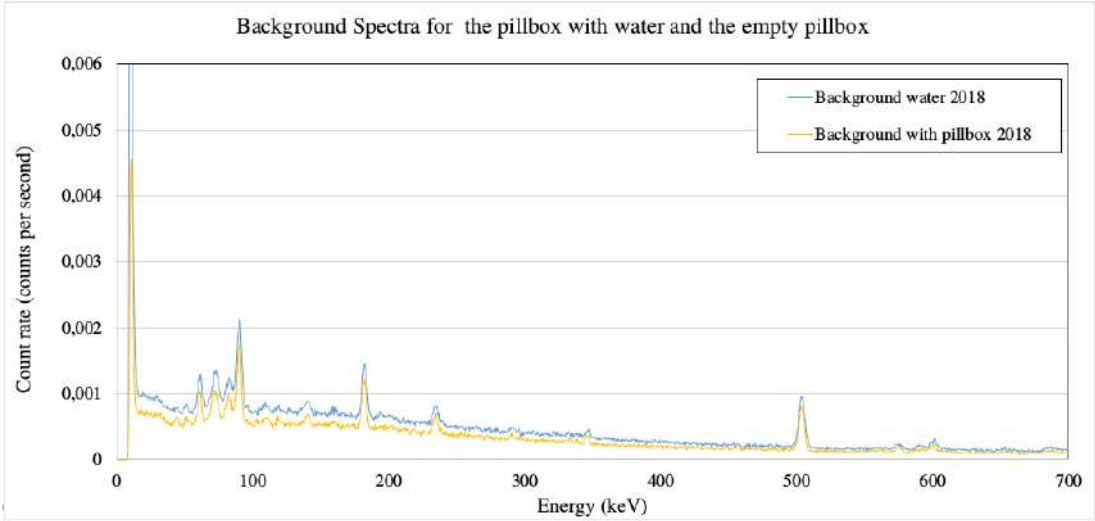

Figure C.2: The activity concentration of ^{238}U and ^{232}Th for all samples

Appendix D

Activity Concentration and Radiological Risk Tables

Table D.1: The location associated with each sample

Sample	Longitude	Latitude	Mass (g)	Date measured
SOS1T	5.08286	7.82466	33.4	2017-06-23
SOS3T	5.06666	7.83677	29.6	2017-06-25
SOS4T	5.07308	7.84527	28.8	2017-06-26
SOS5T	5.07919	7.8275	30.8	2017-06-27
SOS6T	5.09186	7.82469	32.0	2017-06-28
SOS7T	5.08425	7.83844	32.4	2017-06-30
SOS8T	5.08081	7.81041	32.8	2017-07-04
SOS9T	5.07752	7.80378	30.0	2017-07-14
SOS10T	5.0895	7.79828	32.3	2017-07-24
SOS11T	5.103	7.80208	31.5	2017-07-25
SOS12T	5.07661	7.81042	31.2	2017-07-26
SOS17T	5.05844	7.78719	34.0	2017-07-27
SOS18T	5.05533	7.79431	32.6	2017-07-29
SOS19T	5.07561	7.80372	33.5	2017-07-28
SOS20T	5.07283	7.80811	32.3	2017-07-31
SOS21T	5.06364	7.82786	28.0	2017-08-01
SOS22T	5.05733	7.82589	30.9	2017-08-02
SOS23T	5.0298	7.81025	32.0	2017-08-03
SOS25T	5.01739	7.80717	28.7	2017-08-07
SOS27T	5.04306	7.80875	30.2	2017-08-08
SOS28T	5.04583	7.80986	30.5	2017-08-09
SOS30T	5.05444	7.80011	34.6	2017-08-10
SOS31T	5.04689	7.79944	34.0	2018-03-27
SOS32T	5.0375	7.79417	34.9	2018-04-11
SOS33T	5.04333	7.79306	32.8	2018-04-10
SOS34T	5.06	7.81319	33.0	2018-04-09
SOS36T	5.018	7.83736	32.7	2018-04-05
SOS37T	5.02602	7.84617	32.5	2018-04-17
SOS38T	5.02825	7.83583	31.1	2018-04-19
SOS41T	5.04167	7.84956	32.9	2018-04-18

In 2019, three samples were re-measured to test the reproducibility of the results.

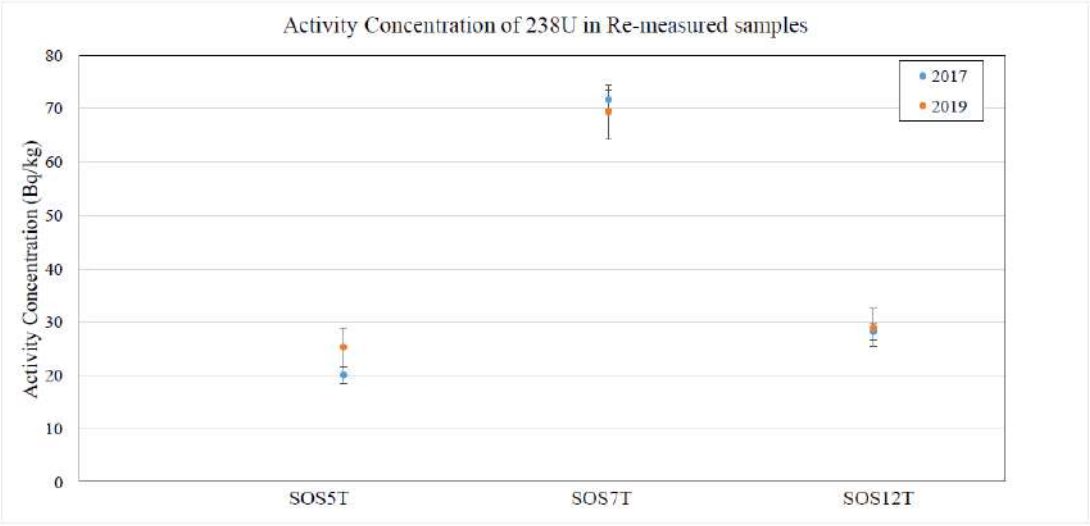

Figure D.1: A comparison of the activity concentration of ^{238}U for 2017 and 2019

The results are tabulated below.

Table D.2: The activity concentration results from 3 samples that were measured in 2017 as well as 2019

Sample	Activity	2017	2019
SOS5T	^{238}U	20.0±1.6	25.2±3.6
	^{232}Th	30.4±1.4	31.0±2.8
	^{40}K	376±17	310±22
SOS7T	^{238}U	71.7±1.8	69.4±5.1
	^{232}Th	108±2.4	108±4.8
	^{40}K	912±22	812±51
SOS12T	^{238}U	28.2±1.7	28.9±3.6
	^{232}Th	44.6±1.6	46.3±3.2
	^{40}K	454±16	403±25

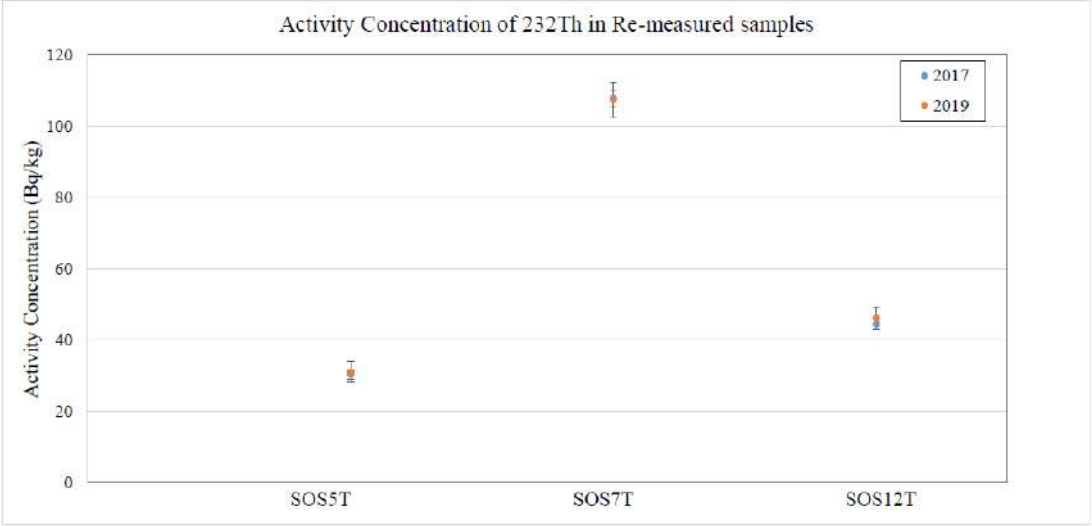

Figure D.2: A comparison of the activity concentration of ^{232}Th for 2017 and 2019

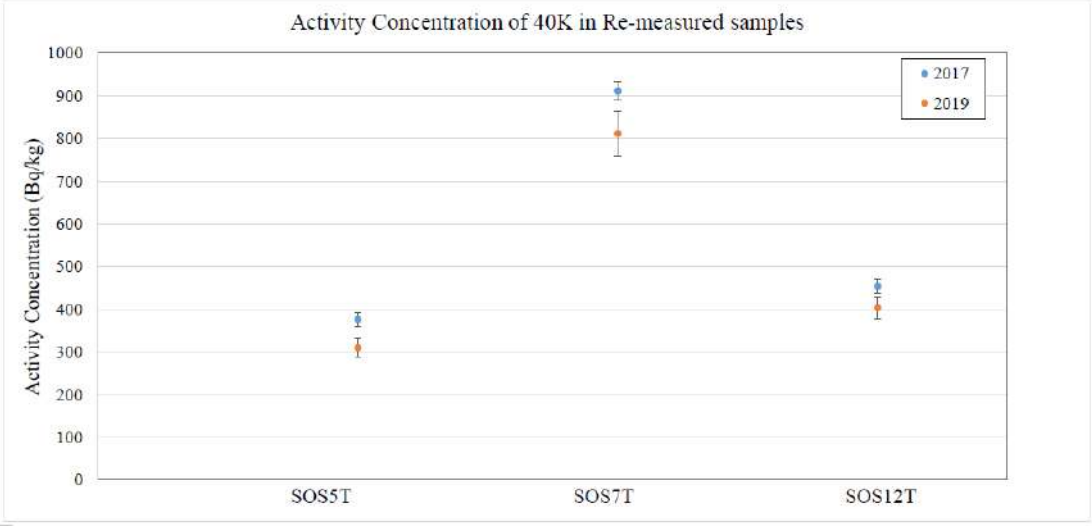

Figure D.3: A comparison of the activity concentration of ^{40}K for 2017 and 2019

The results for the activity concentration calculation are shown in Table D.3. The Standard row at the bottom of Table D.3 indicates the global average values for the activities of the primordial radionuclides and Ra_{eq}. The Standard row at the bottom of Table D.5 and D.6 indicates the maximum permissible limits.

Table D.3: Calculated activity concentration and Radium equivalent activity

Sample	A_U (Bq/kg)	A_{Th} (Bq/kg)	A_K (Bq/kg)	Ra_{eq} (Bq/kg)
SOS1T	52.0±1.9	53.8±1.9	827±20	193
SOS3T	57.6±0.8	34.5±0.7	489±14	145
SOS4T	24.3±1.8	77.7±2.2	249±15	155
SOS5T	20.1±1.6	30.4±1.4	376±17	92
SOS6T	83.9±2.1	57.4±1.9	752±19	224
SOS7T	71.7±1.8	108.0±2.4	912±22	296
SOS8T	58.5±2.0	68.9±1.9	969±21	232
SOS9T	52.1±2.0	35.8±1.5	351±16	130
SOS10T	69.4±2.1	63.6±2.0	954±22	234
SOS11T	70.4±2.0	61.9±1.8	1007±22	236
SOS12T	28.2±1.7	44.6±1.6	454±16	127
SOS17T	51.0±1.9	60.1±1.7	811±19	199
SOS18T	44.0±2.0	95.0±2.2	89±12	187
SOS19T	49.5±1.9	57.4±1.6	498±16	170
SOS20T	56.4±1.9	21.5±1.2	836±20	151
SOS21T	21.6±1.5	12.3±1.2	563±18	83
SOS22T	34.7±1.8	36.7±1.5	360±16	115
SOS23T	14.6±1.6	31.8±1.3	145±12	71
SOS25T	10.1±1.4	24.1±1.3	236±15	63
SOS27T	14.3±1.5	11.8±1.2	722±20	87
SOS28T	13.3±1.6	16.8±1.3	839±20	102
SOS30T	22.1±1.5	33.9±1.3	254±13	90
SOS31T	22.1±3.2	54.7±3.0	116±23	109
SOS32T	20.9±4.1	28.2±3.0	411±41	93
SOS33T	30.0±4.3	47.8±2.9	67±26	103
SOS34T	24.3±3.2	39.4±3.0	407±26	112
SOS36T	20.9±3.8	11.3±2.9	844±33	102
SOS37T	16.0±4.6	16.7±3.5	1200±36	132
SOS38T	17.3±4.2	11.4±3.1	913±36	104
SOS41T	25.5±3.3	60.6±3.6	398±30	143
GARDEN	8.9±3.5	10.5±2.7	43±22	27
Weighted mean	38.5±0.3	37.1±0.3	461±3	139
Standard	33	45	420	370

Table D.4: Activity concentration results obtained in previous studies in Ijero, Nigeria

Sample type	Activity Concentration Range (Bq/kg)	Year	Author
Tailing soil	^{226}Ra: 7.62 to 50.31 ^{232}Th: 12.68 to 234.18 ^{40}K: 249.66 to 1459.25	2014	Isinkaye O. [Isi14]
Soil (in mining areas) Soil (in living areas)	^{238}U: 83.64±8.76 to 150.06±10.46 ^{232}Th: 8.70±0.23 to 44.88±4.05 ^{40}K: 311.47±3.51 to 762.70±6.89 ^{238}U: 24.89±3.42 to 64.59±7.20 ^{232}Th: 10.88±0.23 to 90.76±3.18 40K: 338.47±3.12 to 1500.67±13.28	2019	Usikalu M.R. et al. [Usi+19]
Soil	^{238}U: 12.9±0.02 to 247.46±0.02 ^{232}Th: 0.99±0.05 to 115.37±0.02 ^{40}K: 45.56±0.01 to 2609.27±0.01	2016	Olise F.S. et al. [OAO16]
Soil	^{238}U: 10.1±1.4 to 83.9±2.1 ^{232}Th: 11.3±2.9 to 108.0±2.4 ^{40}K: 67±26 to 1196±36	2019	Present study
Ground water	^{222}Rn: 0.168 to 78.509 Bq/L 18 out of 40 samples > limit 11.1 Bq/L	2018	Akinnagbe et al. [Aki+18]
Ground water	^{222}Rn: 0.9 to 472 Bq/L	2018	Ajiboye et al. [AIK18]

Table D.5: Calculated hazard indices and indoor and outdoor dose rates

Sample	$H_{ex}\prime$(mSv/yr)	H_{in}(mSv/yr)	D_{out}(nGy/hr)	D_{in}(nGy/hr)
SOS1T	0.260	0.661	91	215
SOS3T	0.195	0.546	68	163
SOS4T	0.209	0.483	69	155
SOS5T	0.125	0.304	43	101
SOS6T	0.302	0.831	105	251
SOS7T	0.400	0.994	136	317
SOS8T	0.313	0.784	109	257
SOS9T	0.176	0.493	60	144
SOS10T	0.316	0.819	110	261
SOS11T	0.319	0.829	112	266
SOS12T	0.171	0.419	59	137
SOS17T	0.269	0.676	94	220
SOS18T	0.252	0.623	82	185
SOS19T	0.229	0.593	78	184
SOS20T	0.205	0.561	74	180
SOS21T	0.111	0.281	41	98
SOS22T	0.155	0.404	53	125
SOS23T	0.096	0.231	32	73
SOS25T	0.085	0.197	29	67
SOS27T	0.117	0.273	44	105
SOS28T	0.138	0.311	51	122
SOS30T	0.122	0.303	41	96
SOS31T	0.148	0.355	48	109
SOS32T	0.125	0.307	44	103
SOS33T	0.140	0.361	46	105
SOS34T	0.151	0.368	52	121
SOS36T	0.138	0.332	52	124
SOS37T	0.178	0.400	67	161
SOS38T	0.140	0.327	53	127
SOS41T	0.193	0.454	65	149
GARDEN	0.037	0.097	12	28
Standard	1	1	N/A	N/A

Table D.6: Calculated annual effective dose indoors and outdoors, annual gonadal equivalent dose, excess lifetime cancer risk and percentage risk

Sample	AED_{in} (mSv/yr)	AED_{out} (mSv/yr)	A_G (μSv/yr)	ELCR	ELCR/ max ELCR	excess risk(%)
SOS1T	1.056	0.112	645	0.0033	1.13	13
SOS3T	0.801	0.083	476	0.0025	0.85	-15
SOS4T	0.759	0.084	478	0.0024	0.81	-19
SOS5T	0.496	0.053	307	0.0015	0.53	-47
SOS6T	1.231	0.129	735	0.0038	1.31	31
SOS7T	1.558	0.167	959	0.0048	1.67	67
SOS8T	1.260	0.134	773	0.0039	1.35	35
SOS9T	0.709	0.074	421	0.0022	0.76	-24
SOS10T	1.283	0.135	780	0.0040	1.37	37
SOS11T	1.305	0.137	793	0.0040	1.39	39
SOS12T	0.672	0.072	416	0.0021	0.72	-28
SOS17T	1.081	0.115	663	0.0033	1.15	15
SOS18T	0.907	0.100	561	0.0028	0.97	-3
SOS19T	0.902	0.096	549	0.0028	0.96	-4
SOS20T	0.881	0.091	526	0.0027	0.94	-6
SOS21T	0.482	0.050	295	0.0015	0.51	-49
SOS22T	0.615	0.065	374	0.0019	0.66	-34
SOS23T	0.359	0.039	223	0.0011	0.38	-62
SOS25T	0.328	0.036	206	0.0010	0.35	-65
SOS27T	0.514	0.054	320	0.0016	0.55	-45
SOS28T	0.597	0.063	374	0.0018	0.64	-36
SOS30T	0.471	0.051	290	0.0015	0.50	-50
SOS31T	0.535	0.059	333	0.0017	0.57	-43
SOS32T	0.504	0.054	311	0.0016	0.54	-46
SOS33T	0.514	0.056	313	0.0016	0.55	-45
SOS34T	0.594	0.064	368	0.0018	0.64	-36
SOS36T	0.610	0.063	377	0.0019	0.65	-35
SOS37T	0.788	0.083	495	0.0024	0.84	-16
SOS38T	0.623	0.065	388	0.0019	0.66	-34
SOS41T	0.730	0.080	457	0.0023	0.78	-22
GARDEN	0.140	0.015	85	0.0004	0.15	-85
Standard	1	1	300	0.0029	1	0

Bibliography

[Ade18a] A Adedinni. *Exclusive: Illegal miners invade Ekiti, Osun communities*. access 20 June 2018. 2018. URL: http://petrolgasreport.com/exclusive-illegal-miners-invade-ekiti-osun-communities/.

[Ade18b] TA Adesiyan. "Geochemical evaluation of soil, stream sediment, water and plant samples in Ijero-Ekiti area, South Western Nigeria, in relation to health problems". PhD thesis. University of Benin, Nigeria, 2018.

[AIK18] Y Ajiboye, MO Isinkaye, and MU Khanderkar. "Spatial distribution mapping and radiological hazard assessment of groundwater and soil gas radon in Ekiti State, Southwest Nigeria". In: *Environmental earth sciences* 77.14 (2018), p. 545.

[Aki+18] DM Akinnagbe et al. "Assessment of Radon Concentration of Ground Water in Ijero Ekiti". In: *Manila Journal of Science* 11 (2018), pp. 32–41.

[Ama+17] Amanjeet et al. "Assessment of natural radioactivity levels and associated dose rates in soil samples from historical city Panipat, India". In: *Journal of radiation research and applied sciences* 10.3 (2017), pp. 283–288.

[Anj+11] Roberto Meigikos dos Anjos et al. "External gamma-ray dose rate and radon concentration in indoor environments covered with Brazilian granites". In: *Journal of environmental radioactivity* 102.11 (2011), pp. 1055–1061.

[AO17] Sesan Adeyemi and Ayodele Olagunju. "Putting small-scale mining in perspective: an analysis of risk perception of a southwestern Nigerian community". In: *Review of Social Sciences* 2.7 (2017), pp. 07–18.

[AP] TA Adesiyan and L Petrik. *Location and Accessibility*. e-mail correspondence 18 June 2019.

[Ato] Atomki. *Palmtop MCA Multi Channel Analyzator and Scaler User's Manual*. access 3 August 2018. URL: http://w3.atomki.hu/atomki/Electr/Downloads/mca/usersmanual-2.9.pdf.

[Bab+13] Oluwole Adeyemi Babatunde et al. "Practice of occupational safety among artisanal miners in a rural community in Southwest Nigeria". In: *International Journal of Science, Environment, and Technology* 2.4 (2013), pp. 622–633.

[Bax93] MS Baxter. "Environmental radioactivity: A perspective on industrial contributions." In: *IAEA Bulletin* 35.2 (1993), pp. 33–38.

[BB11] Jerrold T Bushberg and John M Boone. *The essential physics of medical imaging*. Lippincott Williams & Wilkins, 2011.

[Can04] Industries Canberra. *Model 2002 Spectroscopy Preamplifier User's Manual*. USA, 2004.

[CSP12] Simon R Cherry, James A Sorenson, and Michael E Phelps. *Physics in nuclear medicine e-Book*. Elsevier Health Sciences, 2012.

[DAE15] DAE Darwish, KTM Abul-Nasr, and AM El-Khayatt. "The assessment of natural radioactivity and its associated radiological hazards and dose parameters in granite samples from South Sinai, Egypt". In: *Journal of Radiation Research and Applied Sciences* 8.1 (2015), pp. 17–25.

[Dża+18] Agnieszka Dżaluk et al. "Natural radioactivity in granites and gneisses of the Opava Mountains (Poland): a comparison between laboratory and in situ measurements". In: *Journal of radioanalytical and nuclear chemistry* 316.1 (2018), pp. 101–109.

[Eba10] YY Ebaid. "Use of gamma-ray spectrometry for uranium isotopic analysis in environmental samples". In: *Rom J Phys* 55.1-2 (2010), pp. 69–74.

[EEA05] YY Ebaid, SA El-Mongy, and KA Allam. "235U–γ emission contribution to the 186 keV energy transition of 226Ra in environmental samples activity calculations". In: *International Congress Series*. Vol. 1276. Elsevier. 2005, pp. 409–411.

[EPA] EPA. *TENORM: Oil and Gas Production Wastes*. access 22 September 2019. URL: https://www.epa.gov/radiation/tenorm-oil-and-gas-production-wastes.

[FEC99] RB Firestone, LP Ekström, and SYF Chu. *The Lund/LBNL Nuclear Data Search*. access 26 September 2019. 1999. URL: http://nucleardata.nuclear.lu.se/toi/.

[Gil08] GR Gilmore. *Practical Gamma-ray Spectrometry 2nd Edition*. Warrington, UK: John Wiley & Sons, Ltd., 2008.

[Hom] Hometown. *Ijero Ekiti*. access 4 April 2017. URL: http://hometown.ng/listing-item/ijero-ekiti/.

[Hun12] Alistair Hunter. "Radiation biology: an important science for an advanced nuclear nation like South Africa". In: *South African Journal of Science* 108.7-8 (2012), pp. 33–43.

[IAE] IAEA. *Live Chart of Nuclides, nuclear structure and decay data*. access 26 June 2018. URL: https://www-nds.iaea.org/relnsd/vcharthtml/VChartHTML.html.

[IAR88] IARC. *IARC monographs on the evaluation of carcinogenic risks to humans*. France: World Health Organisation, 1988.

[ICR] ICRU. *About ICRU*. access 22 September 2019. URL: icru.org.

[Isi14] O Isinkaye. "Assessment of radiation hazards associated with tailing and sediment from an abandoned gold mine in Ilesa and an active tantalite mine in Ijero, southwest Nigeria". In: (2014).

[Ism16] A Ismail. *Killer gas - Why SA homes are not tested for Radon*. 2016. URL: https://www.health24.com/Lifestyle/Environmental-health/Environmental-disasters/killer-gas-why-homes-in-sa-are-not-tested-for-radon-20160223.

[Jib+16] NN Jibiri et al. "Dose assessments from the measured radioactivity in soil, rock, clay, sediment and food crop samples of an elevated radiation area in south-western Nigeria". In: *Environmental Earth Sciences* 75.2 (2016), p. 107.

[K+87] Kenneth S Krane, David Halliday, et al. *Introductory nuclear physics*. 1987.

[Kin05a] HM King. *Gneiss*. access 31 July 2017. 2005. URL: https://geology.com/rocks/gneiss.shtml.

[Kin05b] HM King. *Quartzite*. access 31 July 2017. 2005. URL: https://geology.com/rocks/quartzite.shtml.

[Kin05c] HM King. *Schist*. access 31 July 2017. 2005. URL: https://geology.com/rocks/schist.shtml.

[Kno00] Glenn F Knoll. *Radiation detection and measurement*. John Wiley & Sons, 2000.

[Lau] Philipp Laube. *Fundamentals: Conductors – Insulators – Semiconductors*. access 25 September 2019. URL: https://www.halbleiter.org/en/fundamentals/conductors-insulators-semiconductors/.

[Law02] M Lawal. "Constraints to small scale mining in Nigeria: policies and strategies for development". In: *Centre for Energy Petroleum Minerals Law and Policy Annual Review-the Dundee Yearbook of International Natural Resources and Energy Law and Policy* (2002), p. 17.

[Mas] Mc Master. *Chapter 8 Hyper-Pure Germanium Detector*. access 20 November 2018. URL: https://www.science.mcmaster.ca/radgrad/images/6R06CourseResources/%5C%5C4RA34RB3%5C_Lecture%5C_Note-8%5C_HPGe%5C_Detector.pdf.

[Mas+18] FB Masok et al. "Measurement of radioactivity concentration in soil samples around phosphate rock storage facility in Richards Bay, South Africa". In: *Journal of radiation research and applied sciences* 11.1 (2018), pp. 29–36.

[Mir] Mirion. *Germanium Detectors*. access 20 November 2018. URL: https://www.mirion.com/products/germanium-detectors.

[New+08] RT Newman et al. "Determination of soil, sand and ore primordial radionuclide concentrations by full-spectrum analyses of high-purity germanium detector spectra". In: *Applied Radiation and Isotopes* 66.6-7 (2008), pp. 855–859.

[Nig19] Ekiti State Government of Nigeria. *Population Figures*. access 20 September 2019. 2019. URL: https://ekitistate.gov.ng/about-ekiti/population-figures/.

[NRF] iThemba LABS NRF. *HPGE (High-purity germanium system)*. access 20 November 2018. URL: https://tlabs.ac.za/hpge-high-purity-germanium-system/.

[NRF17a] iThemba LABS NRF. *Lecture notes in Radiation and dose Measurement*. Aug. 2017.

[NRF17b] iThemba LABS NRF. *Lecture notes in Radiation Protection F753 Learning Material*. Aug. 2017.

[OA10] Olugbenga A Okunlola and Oluwatoyin O Akinola. "Petrochemical characteristics of the precambrian rare metal pegmatite of Oke-Asa area, Southwestern Nigeria: Implication for Ta-Nb Mineralization". In: *RMZ–Materials and Geo Environment* 57 (2010), pp. 525–538.

[OAO16] Felix S Olise, Deborah M Akinnagbe, and Olugbenro S Olasogba. "Radionuclides and radon levels in soil and ground water from solid minerals-hosted area, south-western Nigeria". In: *Cogent Environmental Science* 2.1 (2016), p. 1142344.

[Ong13] Joash Nyakondo Ongori. "In-situ measurements and calculation of radon gas concentration and exhalation from a tailings mine dump". PhD thesis. University of the Western Cape, 2013.

[Pen+18] S Penabei et al. *Assessment of natural radioactivity levels and the associated radiological hazards in some building materials from Mayo-Kebbi region, Chad*. access 20 September 2018. 2018. URL: https://www.researchgate.net/publication/326300461.

[Per04] Instruments PerkinElmer. *572 Amplifier*. USA, 2004.

[Pod+05] Ervin B Podgorsak et al. "Radiation oncology physics". In: *Vienna: International Atomic Energy Agency* (2005), pp. 123–271.

[Pow] Nuclear Power. *Interaction of Gamma Radiation with Matter*. access 18 November 2019. URL: https://www.nuclear-power.net/nuclear-power/reactor-physics/interaction-radiation-matter/interaction-gamma-radiation-matter/.

[Pro07] Radiological Protection. "ICRP publication 103". In: *Ann ICRP* 37.2.4 (2007), p. 2.

[Ran+15] Asha Rani et al. "Assessment of natural radionuclides in the soil samples from Marwar region of Rajasthan, India". In: *Applied Radiation and Isotopes* 101 (2015), pp. 122–126.

[Rev] World Population Review. *Population of Cities in Nigeria*. access 17 September 2019. URL: http://worldpopulationreview.com/countries/nigeria-population/cities/.

[SIL] SILENA. *SILENA INTERNATIONAL SpA*. access 26 September 2019. URL: https://manualzz.com/doc/30432464/silena-international-spa.

[Sta] University Stanford. *Research Fundamentals*. access 25 September 2019. URL: https://web.stanford.edu/group/scintillators/scintillators.html.

[UNS00] Sources UNSCEAR. "effects of Ionizing Radiation". In: *United Nations, New York* (2000), pp. 453–487.

[Usi+19] MR Usikalu et al. "Radiation dose assessment of soil from Ijero Ekiti, Nigeria". In: *Cogent Engineering* 6.1 (2019), p. 1586271.

[WHO09] WHO. *IARC monographs on the evaluation of carcinogenic risks to humans*. France: IARC *Press*, 2009.

[WHO19] WHO. *Nigeria*. 2019. URL: https://www.who.int/countries/nga/en/.

[WIS] WISE. *Uranium Radiation Properties*. access 13 March 2019. URL: http://www.wise-uranium.org/rup.html.

[Wyn17] S Wyngaardt. *Lecture notes in Honours Nuclear Physics*. Mar. 2017.